SHiP
Search for Hidden Particles

SHiP Experiment

PROGRESS REPORT

SHiP Collaboration*

Abstract

Progress on the SHiP experiment and the Comprehensive Design Study (CDS) is presented with focus on the re-optimization, the simulation studies and the detector developments, including beam tests since the Technical Proposal, and the physics performance. This document is complementing the proposal submitted to the update of the European Strategy for Particle Physics (ESPPU).

Keywords

SHiP, Comprehensive Design Study, SPS, CERN

CERN-SPSC-2019-010 / SPSC-SR-248
25/01/2019

*Author list: http://cern.ch/ship/Constitution/SHiP_Authorlist_nov2018.pdf

Contents

1 Introduction

An Expression of Interest [1] for a new experiment at CERN aiming at searching for hidden particles by using the intense beam of protons of the SPS accelerator was submitted to the SPSC in 2013. The SHiP collaboration that has been formed as a result, prepared in 2015 two documents describing the physics case [2], and SHiP's Technical Proposal (TP) [3, 4]. This report provides an update of the physics case, and describes the developments and advances in the technical design and in the evaluation of the physics performance of the proposed experiment since the TP. In parallel, a comprehensive design study of the experimental facility has been performed by the Beam Dump Facility working group in the context of the Physics Beyond Colliders study group [5], and is published in [6].

1.1 Physics Landscape in 2015

The discovery of the Higgs boson at the LHC in 2012 [7–10] made the Standard Model (SM) of elementary particles complete - all the particles predicted by the model have been found, and their interactions, tested at the LHC till now, are consistent with those predicted by the SM. The triumph of the SM in particle physics is accompanied by the success of the standard cosmological model (ΛCDM) based on Einstein's General Relativity, allowing to describe the structure of the Universe by a small number of parameters.

The era of guaranteed discoveries in particle physics has come to the end with the detection of the Higgs boson: for the particular value of the Higgs mass revealed by the LHC, the Standard Model remains self-consistent and valid as an effective field theory up to a very high energy scale, possibly all the way up to the scale of quantum gravity, the Planck scale [11–15]. It is merely intriguing that the particular values of the top-quark and Higgs boson masses lie very close to the criticality line, separating the regions of absolute stability and metastability of the electroweak vacuum (for a discussion and references see [11, 13, 16, 17].

The quest for new particles has not ended, however. We are certain that the SM does not represent the complete picture. Several well-established observational phenomena – neutrino masses and oscillations, dark matter, and the baryon asymmetry of the Universe – cannot be explained with the known particles alone and clearly indicate that New Physics (NP) should exist. Unfortunately, we do not have a definitive prediction where to find NP, nor do we have experimental clues on the masses, spins, and coupling constants of the associated new particles.

1.2 Physics landscape in 2018

In the last 3 years this picture did not change. The first ever run of proton-proton collisions at a centre-of-mass energy of 13 TeV has uncovered no significant deviations from the Standard Model [18–25]. Nor did other searches for new physics at particle physics laboratories worldwide. Intriguing hints of lepton flavour universality violations in semi-leptonic B decays have been reported in the recent years by Belle and LHCb [26–30]. Even if these hints are confirmed, it will not be possible to determine the scale of NP with certainty.

Significant efforts in neutrino physics in recent years [31, 32] did not improve our knowledge about the mass scale of the new particles that could give rise to the neutrino masses and oscillations. In particular, taking aside different unconfirmed signals of eV-scale neutrino states (for a review see [33]), all the oscillation signatures can be explained by the SM extended by two additional sterile neutrinos of essentially any mass ranging from a fraction of an eV to very high masses.

With regard to dark matter, the absence of detections in direct and indirect search experiments of weakly interacting massive particles (WIMPs) in the GeV-TeV mass range has stimulated growing interest in light dark matter (LDM) candidates: sterile neutrinos, axions, WIMP-like particles but with lower (sub-GeV) masses [34–36]. This has led to an important increase in activity around the corresponding experimental efforts: LDMX [37, 38], MiniBooNe [39–41], T2K [41], CRESST [42], NA64 [43, 44],

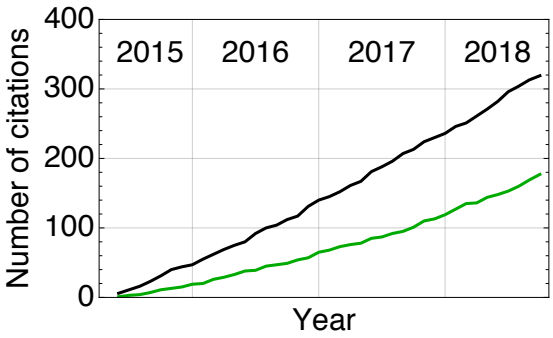

Figure 1: Citation history of the SHiP physics paper [2] (black) and of the SHiP Technical Proposal [3] since their initial publication in April 2015.

BDX [45] and many others. A similar trend is revealed in cosmological studies where models of structure formation, as well as systematic searches for various signatures of such particles in cosmological and astrophysical observations, have been investigated. As a result, the "cosmologically interesting" region of the parameter space of hidden particles, which can be tested at SHiP and the LHC, was pinned down with much better accuracy.

In summary, the current results in theoretical and experimental particle physics, cosmology and astrophysics still leave the parameters of NP largely undetermined. The fact that no convincing signs of new particles have been found so far suggests that they are either heavier than the reach of the present-day accelerators or interact very weakly.

The current experimental situation thus defines three main and fully complementary directions of development of particle physics:

- The direct searches for NP, namely the search for new phenomena occurring at high (untested) energies, such as the production of new types of particles (*energy frontier*).
- The indirect searches for NP, namely the search for possible failures in the SM predictions when performing high-precision experiments at any energy scale (*precision frontier*).
- The searches for extremely feebly interacting relatively light particles (*intensity frontier*).

While the energy frontier is investigated at the LHC and the precision frontier is pursued at LHCb and elsewhere, the intensity frontier remains under-explored. It is the main goal of the SHiP experiment to make a break-through in this direction. In particular, SHiP will explore the domain of particle masses and couplings that are not accessible to the energy and precision frontier experiments, and potentially find the particles that lead to neutrino masses and oscillations, explain baryon asymmetry of the Universe, and shed new light on the properties of dark matter (for a detailed discussion see [2]). The updated SHiP design, as described in this report, goes even further in this direction.

New particles with masses much lighter than the electroweak scale can couple to the SM fields via renormalisable interactions with small dimensionless coupling constants. These, so called "portals", can mediate interactions between the SM and "Hidden Sectors". Depending on the spin of the mediator, there are three classes of portals mixing with the SM particles: scalar portal (spin 0, coupling coefficient $\sin^2\theta$), neutrino portal (spin 1/2, coupling coefficient U^2) and vector portal (spin 1, coupling coefficient ϵ). SHiP is sensitive to all these portals, and moreover to a special case of non-renormalizable models predicting axion-like particles (ALP) decaying to photons, gluons and fermions (coupling coefficients $g_{a\gamma\gamma}$, g_{agg} and g_{aff}, respectively). SHiP can also probe the existence of LDM through the observation of its scattering off electrons and nuclei in the detector material. In addition to the exploration of the Hidden Sector, the SHiP physics program includes a rich program of tau neutrino physics and measurements of neutrino-induced charm production.

SHiP has received a large amount of attention from the particle physics community. The SHiP physics paper [2] is a highly cited document (see Figure 1), and many groups continue to explore the scientific potential of the experiment, making detailed predictions for models of feebly interacting particles. In the wake of the SHiP experiment, several dedicated intensity frontier experiments have been proposed in the recent years: CODEX-b [46], MATHUSLA [47–49], FASER [50–52]. Recognising the importance of diversifying the search efforts, the CERN Management created in 2016 a dedicated study group "Physics Beyond Colliders" (PBC) [5]. Searches for heavy neutral leptons, dark photons, dark scalars, light dark matter, and other super-weakly interacting light particles has also been included in the scientific goals of many presently running experiments [39, 40, 42–44, 44, 53–67].

1.3 Overview of the SHiP developments and advances since the TP

Despite an active program of searches for HS particles in many experiments, SHiP remains a unique dedicated experiment capable of reconstructing the decay vertex of an HS particle, measuring its invariant mass and providing particle identification of the decay products in an environment of extremely low background. Moreover, SHiP is also optimised to search for LDM through scattering signatures and for tau neutrino physics.

Since the Technical Proposal the SHiP design went through a significant re-optimisation phase. Figure 2 shows the layout of the re-optimised SHiP detector. While the overall set-up of the detector remains unchanged, the geometry and the detector composition has been significantly modified, and technological studies and test beams have brought maturity to the design. SHiP consists of the proton

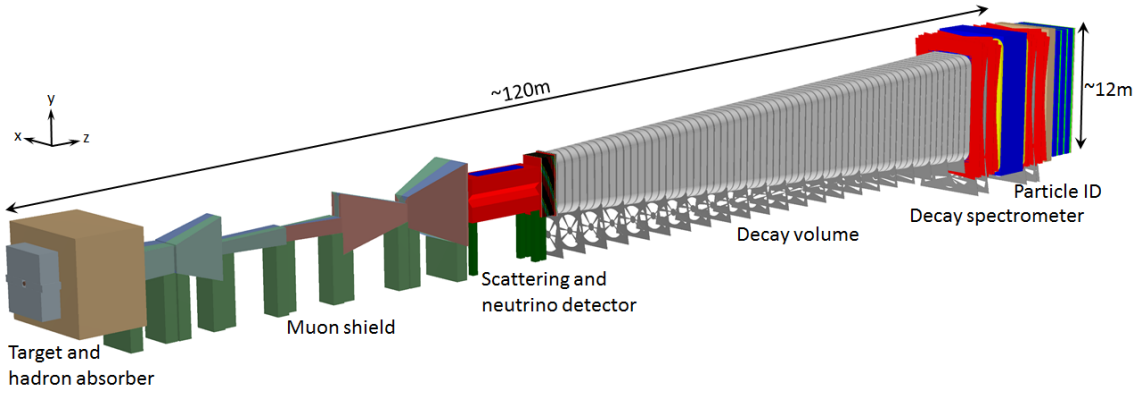

Figure 2: Overview of the SHiP experiment as implemented in FairShip.

target, followed by a hadron stopper and an active muon shield that sweeps muons produced in the beam dump out of acceptance. Since the TP, the target has been extended from ten to twelve interaction lengths in order to reduce the hadronic shower leakage. Studies were made to minimise the distance between the target and the SHiP spectrometers to improve the acceptance of the spectrometers, and to reduce the weight and cost of the muon shield. A significant improvement was achieved by starting the first section of the muon shield within the hadron stopper by integrating a coil which magnetises the iron shielding blocks.

The SHiP detector itself incorporates two complementary apparatuses, the Scattering and Neutrino Detector (SND), and the Hidden Sector (HS) spectrometer. The SND will search for LDM scattering and perform neutrino physics. It is made of an emulsion spectrometer located inside a single long magnet with a field above 1.2 T in the entire volume, and a muon identification system. The emulsion spectrometer is a hybrid detector consisting of alternating layers of an absorber, nuclear emulsion films and fast electronic trackers. The absorber mass totals $\sim$ 10 tonnes.

The HS decay spectrometer aims at measuring the visible decays of HS particles by reconstructing their decay vertices in a 50 m long decay volume. In order to eliminate the background from neutrinos

interacting in the decay volume, it is maintained at a pressure of $\mathcal{O}(10^{-3})$ bar. To maximise the sensitivity to HS particles the muon shield was shortened in combination with changing the shape of the decay volume from an elliptic cylinder to a pyramidal frustum. The decay volume is followed by a large spectrometer with a rectangular acceptance of 5 m in width and 10 m in height.

The main element of the HS decay spectrometer is the straw tracker designed to accurately reconstruct the decay vertex, the mass, and the impact parameter of the hidden particle trajectory at the proton target. The main change since the TP is the removal of the straw veto station that was located 5 m into the decay volume, and the increase of the straw diameter from 10 mm to 20 mm. Also, all tracker stations upstream and downstream of the magnet have now the same dimensions to ease construction and to reduce cost. The spectrometer dipole magnet is still based on a warm magnet with a fiducial aperture of $5 \times 10\,\mathrm{m}^2$ and a field integral of $\sim$0.5 Tm, but the coil and the fitting of the coil have been updated in order to accommodate the rectangular vacuum tank of the spectrometer section.

A set of calorimeters and muon detectors provide particle identification, which is essential in discriminating between the very wide range of HS models. For the TP, the ECAL was optimised to provide electron identification and π^0 reconstruction. It has now been decided to extend the ECAL requirements to include reconstruction of axion-like-particles (ALP) decaying to the two photon final state that is the unique way to discriminate between an ALP and a dark photon or a dark scalar. The current version of ECAL, called SplitCal, is a longitudinally segmented lead sampling calorimeter consisting of two parts which are mechanically separated in the longitudinal direction. Each part is equipped with high spatial resolution layers in order to provide pointing with a resolution of $\sim$5 mrad for photons originating from ALP decays. The longitudinal layer segmentation of SplitCal also improves the electron/hadron separation. This opened the possibility to remove the HCAL detector without compromising the PID performance, and only leave the absorber for the purpose of muon filtering.

The muon system consists of four stations interleaved by three muon filters. The ECAL converter material and the muon filters provide sufficient material budget to stop low momenta muons, such that the last muon station is only reached by muons with momenta exceeding 5.3 GeV/c. Since the TP, the muon system considers a new technology based on scintillating tiles with direct SIPMs readout. This option provides better time resolution and is more robust against hit rate variations.

Since the key feature of the HS decay spectrometer design is to ensure efficient suppression of the various backgrounds, the tracking and particle identification are complemented by a dedicated timing detector with $\sim$100 ps resolution to provide a measure of time coincidence, in order to reject combinatorial backgrounds. The decay volume is instrumented by the surround background tagger (SBT) whose purpose is to detect neutrino and muon inelastic interactions in the vacuum vessel walls which may produce long-lived neutral particles decaying in the decay volume and mimicking the HS signal events. Similarly, tagging of interactions in the upstream material of the muon identification system of the SND detector is provided by the associated detector layers.

The muon shield and the SHiP detector systems are housed in an $\sim$120 m long underground experimental hall at a depth of $\sim$15 m. To minimise the background induced by the flux of muons and neutrinos interacting with material in the vicinity of the detector, no infrastructure systems are located on the sides of the detector, and the hall is 20 m wide along its entire length.

2 Proton beam and experimental facility

The Comprehensive Design Study for the experimental facility has been carried out by the Beam Dump Facility working group and by its dedicated subgroups in the context of the Physics Beyond Colliders study group [5], in close collaboration with the SHiP experiment. Based on the request put forward in the addendum to the SHiP Technical Proposal [3], this study phase has consisted in a detailed elaboration of the SHiP operational scenario and in a preliminary design of the main components of the proton delivery, the target and the target complex, and the experimental area, together with a detailed evaluation of the radiological aspects and mitigation. Several critical items have been prototyped to demonstrate the concepts, notably the new type of three-way combined beam splitter/kicker magnet which allows alternatively feeding protons to the EHN2 experimental hall and the SHiP experiment, and the target system. In addition, it has been considered of high importance to perform a preliminary study of the integration of the whole complex, and the civil engineering design and execution process, in order to produce a more precise cost estimate and time line for the project. A full write-up of the Comprehensive Design Study for the facility is available ([6] and references therein).

Following the global re-optimisation of the experimental configuration, significant progress has also been made on the development of the muon shield magnet system, the decay vacuum vessel and its interfaces with the spectrometer magnet, and on the detector layout. Based on this, it has also been possible to specify the experimental area and the requirements on the infrastructure and the services, and to draw up a preliminary plan for the installation of the detector.

The sections below summarise the status and the conclusions most relevant to the SHiP experiment concerning the beam line and the experimental facility, and the status of the development of the muon shield and the decay vacuum vessel.

2.1 Proton yield and beam delivery

At the SPS, the optimal experimental conditions for SHiP are obtained with a proton beam energy of around $400\,\mathrm{GeV}$. The SHiP operational scenario implies returning to full exploitation of the capacity of the SPS. The request for the proton yield is based on a similar fraction of beam time as the past CERN Neutrinos to Gran Sasso (CNGS) program. A nominal beam intensity of 4×10^{13} protons on target per spill is assumed for the design of the experimental facility and the detector. In the baseline scenario for SHiP, the beam sharing delivers an annual yield of 4×10^{19} protons to the Beam Dump Facility and a total of 10^{19} to the other physics programs at the CERN North Area, while respecting the beam delivery required by the HL-LHC . The physics sensitivities are based on acquiring a total of 2×10^{20} protons on target, which may thus be achieved in five years of nominal operation.

In the search for HS decay vertices the control of combinatorial background from random combinations of residual muons relies on slow extraction of de-bunched beam with good uniformity over a timescale of around a second. The slow extraction is also required in order to dilute the large beam power on the proton target. The probability of combinatorial events is directly related to the proton interaction rate in the target, which should have minimum variations. A machine study in 2017 showed the encouraging results that the spill harmonic content in extractions of one second is not worse than in the longer spills used for the North Area. In order to measure the structure at very fine time resolution, and to take it into account in the background studies, SHiP has contributed to upgrading the in-vacuum detector that was initially developed and installed by the UA9 collaboration to study crystal-assisted extraction [68]. The detector is installed in the TT20 transfer line, downstream of the extraction region, and is based on a radiation-hard quartz bar which can be moved in and out of the beam. The Cherenkov light produced by the protons is read out with a photo-multiplier. With the upgrade the system is capable of measuring the proton intensity at rates up to 10 MHz. A series of measurements was performed in parallel to a BDF/SHiP Machine Development aiming at optimising the beam extraction process and aiming at exposing a prototype of the SHiP target. Figure 4 shows the measured proton intensity per 400 ns and

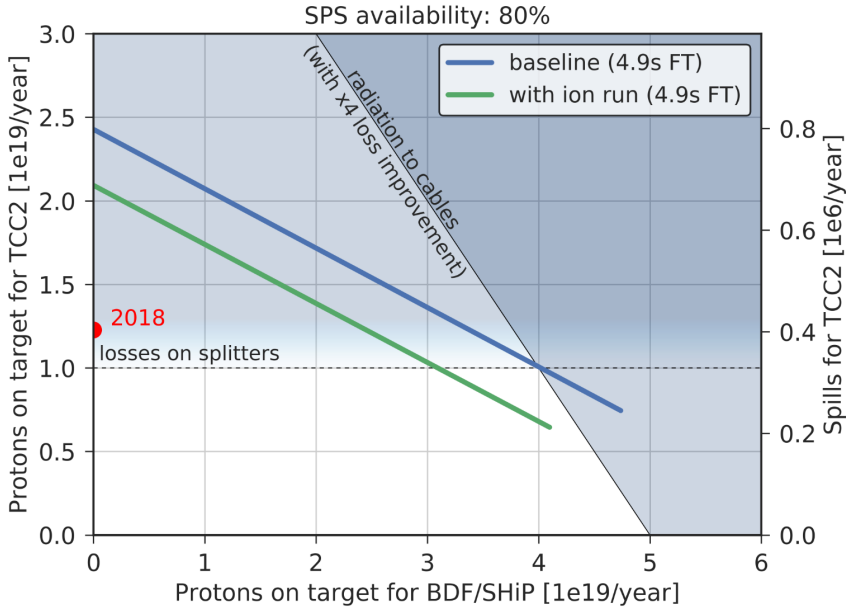

Figure 3: Projection of number of protons and number of spills on the North Area targets (TCC2) as a function of the number of protons on target for BDF/SHiP. The blue line shows the situation with only proton operation. The green line shows a scenario including ion operation. Both scenarios include operation of HiRadMat and AWAKE as in 2018. The integrated number of protons on the targets with the super-cycle used in 2018 is indicated in red.

100 ns in the SHiP 1 s spills, normalised to the expected average rate with a perfectly uniform extraction. The figures shows that a good uniformity has been achieved. The average proton rate at these time scales is a factor of two to three larger than in a perfectly uniform extraction and remain for the larger part within a factor of five. Further studies aim at measuring the variations as close as possible to the 100 ps time resolution of the SHiP timing detector.

Significant progress has been made in the studies of techniques to decrease the beam losses on the field wires of the septum magnets during the slow extraction process, and to reduce the induced activation in the surrounding material. A reduction of a factor of four with respect to the levels in the past is necessary to achieve the baseline intensity of 4×10^{19} protons on target per year. The studies have pursued direct mitigation based on the use of a thin device which scatters the particles that would

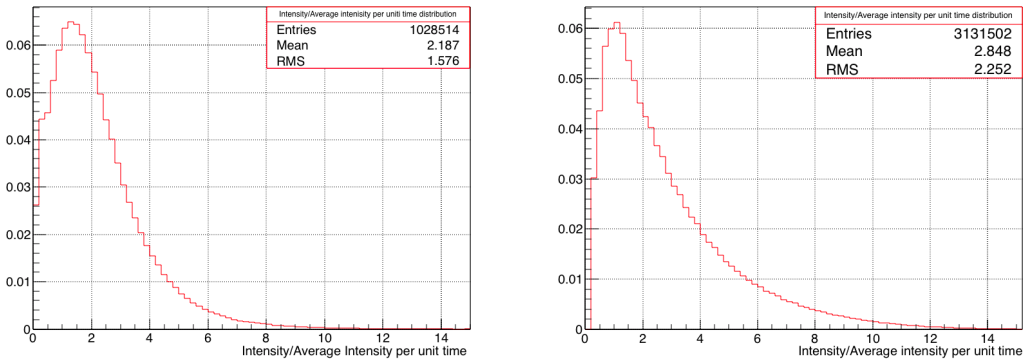

Figure 4: Probability density function of the measured proton rate per 400 ns (left) and 100 ns (right) in the SHiP 1 s spills, normalised to the expected average rate with a perfectly uniform extraction. Courtesy of Francesca Maria Addesa.

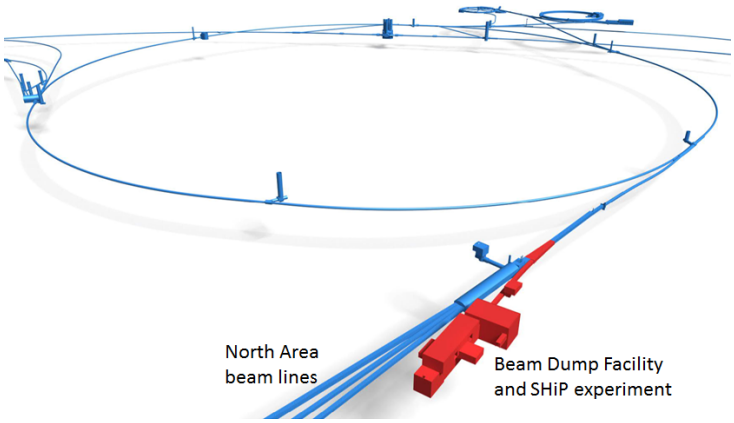

Figure 5: Overview of the CERN injector complex indicating the location of the new SPS Beam Dump Facility designed to house the SHiP experiment.

otherwise hit the septum wire, crystal channeling, and modified optics to reduce the beam density in the region of the septum wires. Recent tests have demonstrated that, together with improved orbit stability and alignment of the septa, it is possible to combine crystal shadowing with the modified optics to achieve a net reduction of more than a factor three. This shows that the SHiP baseline proton yield is realistically within reach.

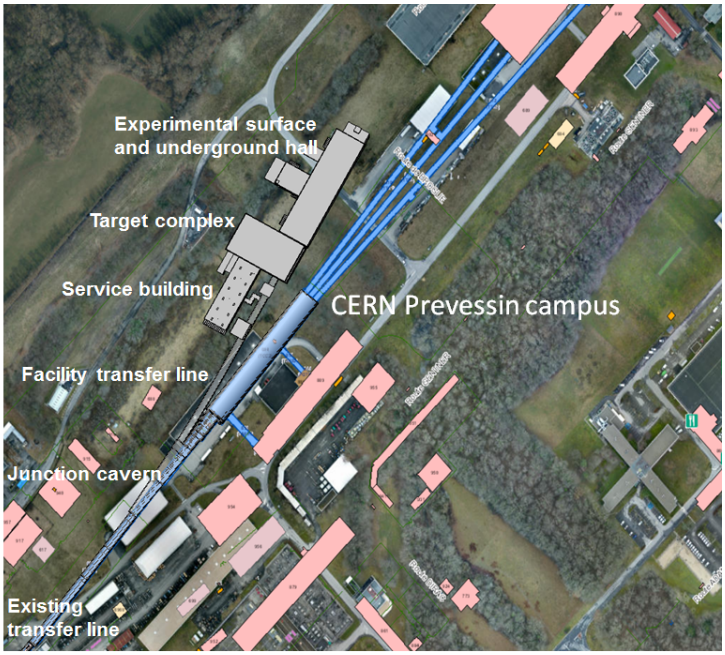

Figure 6: Overview of new surface and underground structures for the Beam Dump Facility. The beam-axis is at a depth of about $10\,\mathrm{m}$ which allows trenching the entire complex from the surface.

Currently, CERN has no high-intensity experimental facility which is compatible with the full beam power of the SPS. The proposed implementation of the beam dump experimental facility is based on minimal modification to the SPS complex and maximal use of the existing beam lines (Figure 5). CERN's North Area has a large space next to the SPS beam transfer lines which is for the most part free of structures and underground galleries, and which could accommodate the proposed facility (Figure 6).

In addition, it may be designed with future extensions in mind. A new type of three-way bi-polar beam splitter/kicker magnet allows alternatively switching the beam to a short new transfer line for the beam dump experimental facility, and otherwise splitting the beam between the other existing experimental facilities in the CERN North Area operational.

2.1.1 Operation with slow beam extraction in bunched mode

The uniform extraction is less critical in the search for a HS scattering signatures and in the neutrino physics, than in the search for decay vertices. On the contrary, slow extraction of bunched beam would provide undoubtful evidence of a Light Dark Matter signal, by measuring their different times of flight. For this reason, should an observation in the scattering detector require consolidation, a second mode of operation with slow extraction of bunched beam is being discussed. Figure 7 shows the region of discrimination assuming the 4σ SPS bunch length of $1.5\,\mathrm{ns}$ and a bunch spacing of $25\,\mathrm{ns}$ and $5\,\mathrm{ns}$, and a 40m distance between the proton target and the detector.

Several aspects of this mode of operations must be further investigated. The current $25\,\mathrm{ns}$ bunch structure used for the LHC is filled into the SPS in batches of 72 bunches every 3.6s. The repetition time in the SPS in this scheme is $18\,\mathrm{s}$ which would have a significant negative impact on the integrated proton yield for SHiP. Alternative schemes are under investigation. With $5\,\mathrm{ns}$ bunch spacing, it is theoretically possible to achieve the SHiP baseline proton yield. In both cases, the slow extraction loss levels must be controlled. First investigations show that, with the current extraction scheme, the losses in the septa are slightly higher than with debunched beam. Studies are under way.

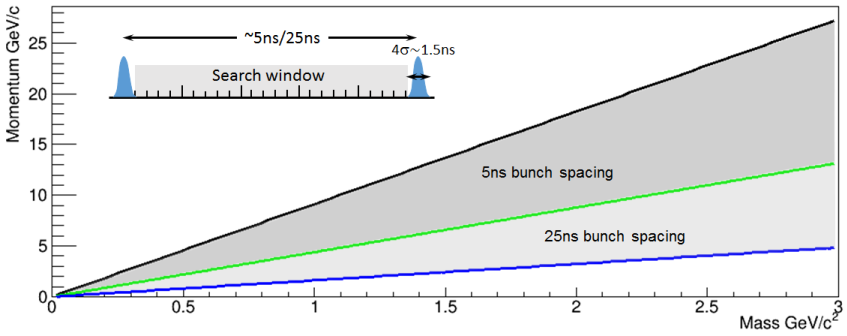

Figure 7: Mass-momentum region in which it is possible to discriminate a Light Dark Matter scattering signature from a neutrino interaction in the Scattering Spectrometer using slow extraction of bunched beam in the SPS and a time-of-flight measurement. The figures assumes a bunch structure with $5\,\mathrm{ns}$ respectively $25\,\mathrm{ns}$ bunch spacing and $1.5\,\mathrm{ns}(4\sigma)$ bunch length, and a distance of $40\,\mathrm{m}$ between the target and the detector.

2.2 Target system

The physics scope of the SHiP experiment requires a proton target which maximises the production of charm and beauty hadrons, as well as photons. At the same time, the proton interactions give rise to copious direct production of short-lived meson resonances, as well as pions and kaons. While a hadron stopper of a few meters of iron is sufficient to absorb the hadrons and the electromagnetic radiation emerging from the target, the decays of the pions, kaons and short-lived meson resonances result in a large flux of muons and neutrinos. In order to reduce the flux of neutrinos, in particular the flux of muon neutrinos and the associated muons, the pions and kaons should be stopped as efficiently as possible before they decay. The target should thus be long and be made of a material with the highest possible atomic mass and atomic charge. It should be sufficiently long to intercept virtually all of the proton intensity and to contain the majority of the hadronic shower with minimum leakage.

Studies show that the required performance may be achieved with a longitudinally segmented hybrid target consisting of blocks of titanium-zirconium doped molybdenum alloy (TZM, density $10.22\,\mathrm{g/cm^3}$ as compared to $10.28\,\mathrm{g/cm^3}$ for pure Mo) in the core of the proton shower followed by blocks of pure tungsten. The blocks are interleaved with $5\,\mathrm{mm}$ wide slots for water cooling. In order to respect the material limits derived from thermo-mechanical stresses, the thickness of each block has been optimised to provide a relatively uniform energy deposition and a sufficient heat flux for an efficient energy extraction.

As compared to the Technical Proposal the target has been extended from ten to twelve interactions lengths in order to reduce the hadronic shower leakage into the hadron stopper. The transversal dimensions have also changed from a square block of $300 \times 300\,\mathrm{mm^2}$ to a cylinder with a diameter of $250\,\mathrm{mm}$. Figure 8 shows the preliminary design of the target system. All these changes were implemented in the SHiP physics simulation for the Comprehensive Design Study.

A prototype target and a preliminary design of the enclosure with cooling and online instrumentation have been built and tested with beam in 2018 up to an integrated exposure of 2.5×10^{16} protons. The production of the target prototype allowed testing the manufacturing process via hot isostatic pressing. The beam test aimed at exposing the target material to similar conditions as expected in the final target to evaluate the effect of the cyclic stresses and temperatures in the core and in the cladding materials. The prototype enclosure enabled testing the cooling performance. The test campaign was fully successful and also demonstrates that the simulation which has been developed for the target design reproduces accurately the target behaviour. The target material is now being prepared for Post Irradiation Examination (PIE).

The infrastructure complex to house the proton target with the associated services and remote handling, which is fully compatible with the radiation protection and environmental considerations, have also been taken through an advanced study demonstrating the feasibility of the preliminary design (Figure 9) [69].

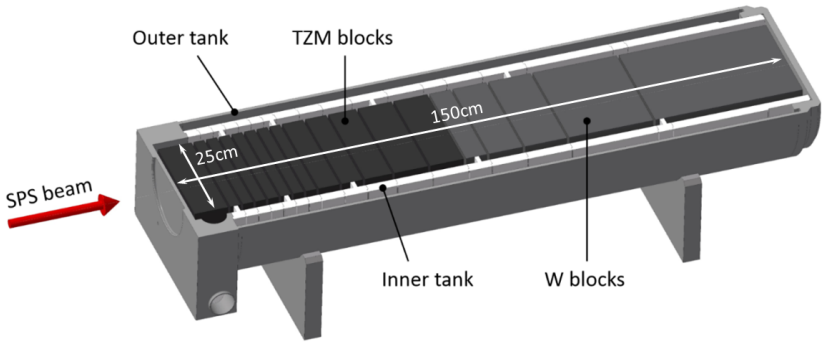

Figure 8: Layout of the preliminary target assembly, showing the TZM and the tungsten blocks and the inner vessel embodying the water cooling of the target.

2.3 Experiment layout

Despite the aim to cover long lifetimes, the sensitive volume should be situated as close as possible to the proton target due to the relatively large transverse momentum of the hidden particles resulting from the limited boost of the heavy hadrons. The minimum distance is only constrained by the need of a system to absorb the electromagnetic radiation and hadrons emerging from the proton target, and to reduce the beam-induced muon flux. The SHiP experiment aims at reducing the beam-induced backgrounds to below 0.1 events in the projected sample of 2×10^{20} protons on target. To meet this objective, the experimental set-up includes a set of magnets which deflect muons emerging from the target, and a vacuum vessel to reduce the number of neutrino interactions in the decay volume.

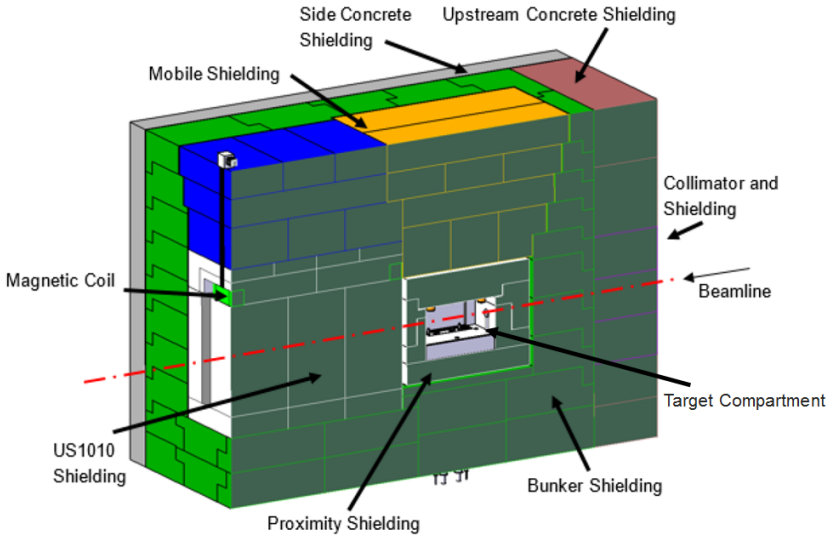

Figure 9: Cross-section of the target bunker showing the location of the target compartment, the surrounding iron shielding, and the magnetic coil and yoke incorporated into the downstream hadron stopper. The whole assembly is housed in a helium vessel.

The layout of the experimental area has also been updated in order to reduce background. The TP design had an $8\,\mathrm{m}$ wide tunnel around the muon shield. Since the cavern walls introduce back-scattering of muons, the width of the underground detector hall was changed to $20\,\mathrm{m}$ along its entire 120 m length.

2.3.1 Muon shield

The muon shield is designed to reduce the flux of muons by six orders of magnitude in the detector acceptance. Since the TP, the muon shield design has seen a major update. Firstly, the separation of positive and negative muons in the first section of the shield can be achieved in the shortest distance by the application of a magnetic field as soon as the muons are produced. While it is not practically possible to magnetise the target in the SHiP set-up, the new design includes a magnetisation of the hadron stopper. Secondly, with this addition, the field configuration of the entire set of free-standing magnets has been re-optimised. The resulting system of magnets is now $35\,\mathrm{m}$ long, compared to the TP design of 48 m, and has 1300 T of magnets (previously 2900 T). Since it has been possible to maintain the spectrometer aperture of $5 \times 10\,\mathrm{m}^2$, the reduced length of the shield gives the detector a larger geometric acceptance for signal decays.

Magnetisation of the target hadron stopper

The proton target is followed by a $5\,\mathrm{m}$ long hadron stopper. The physical dimensions of the absorber are mainly driven by the radiological requirements. The iron of the hadron stopper has been magnetised over a length of 4 m with the help of a magnetic coil integrated into the shielding (Figure 9 and Figure 10). The applied dipole field makes up the first section of the muon shield.

The coil and the integration of the coil in the target shielding is subject to several severe constraints related to the radiation exposure, powering, heat extraction, and handling. As shown in Figure 11 the coils has been located 1.3 m above the beam axis in order to reduce the exposure to radiation.

A contract has been established with Rutherford Appleton Laboratory for the design studies of the magnetisation of the hadron stopper up to specifying the prototyping of the coil. Preliminary design work on the magnet configuration and on the coil has been carried out. The first magnetic field modelling in Opera Vector Fields shows that a $\sim$1.6 T field along the beam axis can be realistically achieved. Figure 12

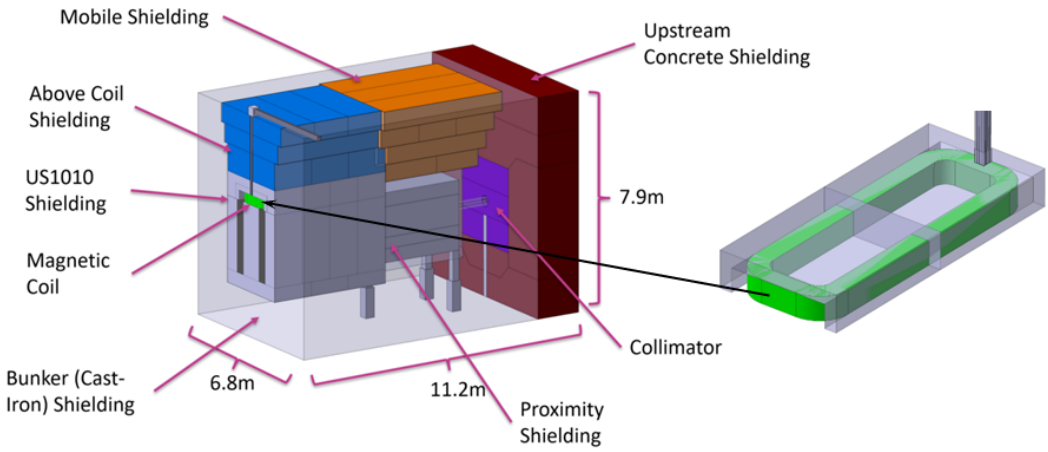

Figure 10: View of the magnetised section of the target shielding with the yoke configuration and the coil. The coil is embedded in specially designed shielding blocks which restrains the coil during operation and which provides crane lifting points should an intervention be necessary.

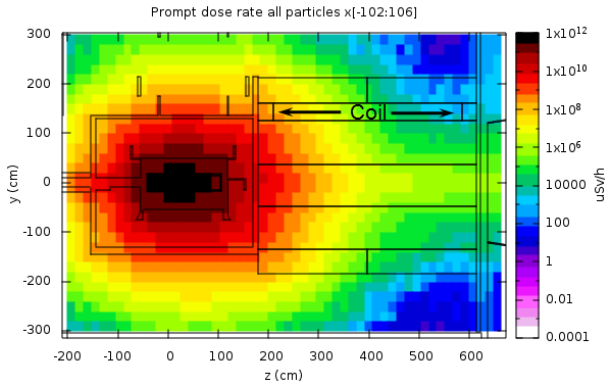

Figure 11: Effective dose in the target bunker integrated over $x = \pm 1\,\mathrm{m}$, showing the location and required level of radiation hardness for the design of the coil and the services.

shows the field in idealistic conditions. Initial calculations indicate that the thermal and the electrical engineering of a coil of this size would be manageable. An aluminium tape conductor is currently preferred for mass, radiation and thermal reasons. It is recommended that a coil assembly comprised of a number of coils is used for redundancy. Two configurations are being pursued, either multiple coils stacked vertically stretching the entire length of the volume to magnetise, or multiple coils located in a chain horizontally.

Free-standing muon shield

The design of the muon shield and the residual rate of muons depends on the momentum distribution of the muons produced in the initial proton collision. The latest shield optimisation and rate estimates were performed using full MC simulations with PYTHIA and GEANT, and Machine Learning techniques. In order to validate these simulations, an experiment was performed in summer 2018 (Section 3.4.1) to measure the muon spectrum using a replica of SHiP's target [70].

The muon shield optimisation is based on the use of Grain-Oriented (GO) steel allowing a high magnetic flux density at a very limited current. Grain-oriented steel sheets comes in $0.3 - 0.5\,\mathrm{mm}$ thickness. Taking into account the packing factor and other imperfections it was estimated that an average field of $1.7\,\mathrm{T}$ could be achieved throughout the magnets. By default, the machine learning optimisation

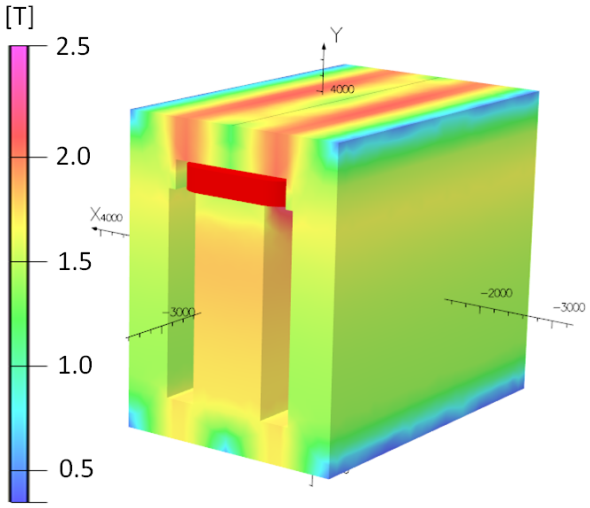

Figure 12: The magnetic field in the magnetised volume of the hadron stopper in idealistic conditions. The coil is shown in red near the top of the shielding.

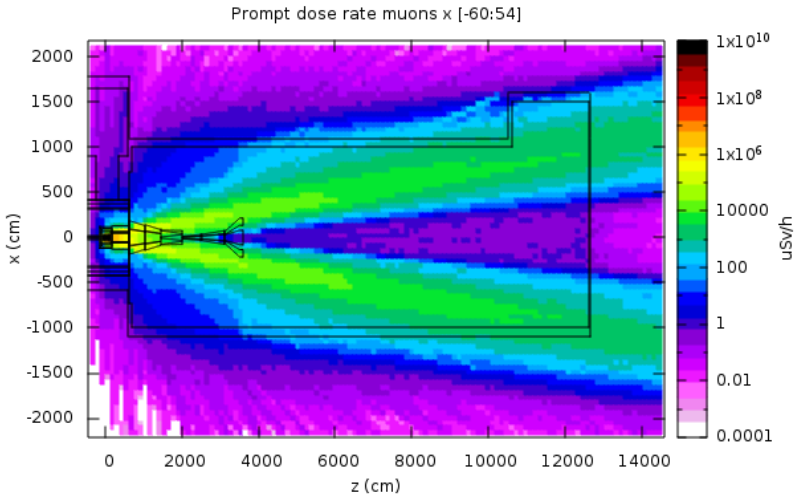

Figure 13: Prompt dose rate from muons at the level of the beam axis, illustrating the function of the muon shield. The layout of the muon shield is outlined in black between $0 - 40\,\mathrm{m}$.

starts from a free-standing muon shield consisting of six magnets, each of $\sim 5\,\mathrm{m}$ length, separated by 10 cm gaps. The overall geometry of the shield is described by 56 parameters. The geometric parameters are optimised by minimising a loss function that reduces both the number of muons entering into the decay volume and the resulting physical weight. The simulation sample, which is propagated through a full GEANT simulation of the detector for each iteration of the optimisation, is based on ∼18M muons produced in the target. The optimisation is extremely CPU intensive and a Bayesian optimisation procedure is therefore employed. Despite the large simulation sample, the optimisation is statistically limited with only a handful of muons passing through the final shield configuration. These characteristics make the use of conventional gradient based algorithms impossible. Figure 13 shows the muon flux through the re-optimised muon shield simulated with FLUKA [71]. The residual muon background entering the

detector acceptance is mainly composed of muons which undergo large-angle multiple scattering in the first part of the shield causing them to move to the "wrong" side of the beam line. The second part of the shield then focuses them towards the detector.

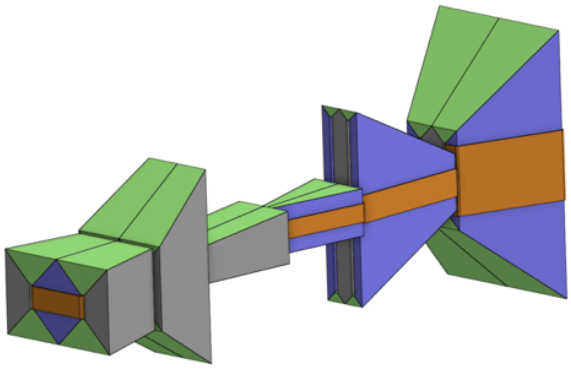

Figure 14: 3D view of the optimised muon magnetic shield.

The re-optimised parameters of the magnets obtained from the machine learning have been used to build a 3D CAD model of the muon shield (Figure 14). The model was used to produce a realistic magnetic field simulation with the OPERA package. Figure 15 shows the calculated magnetic field in a cross-section of the muon shield. The magnetic field simulation shows a good field homogeneity and strength in the regions critical for deflecting the high momentum muons and minor degradation in the less important outer regions.

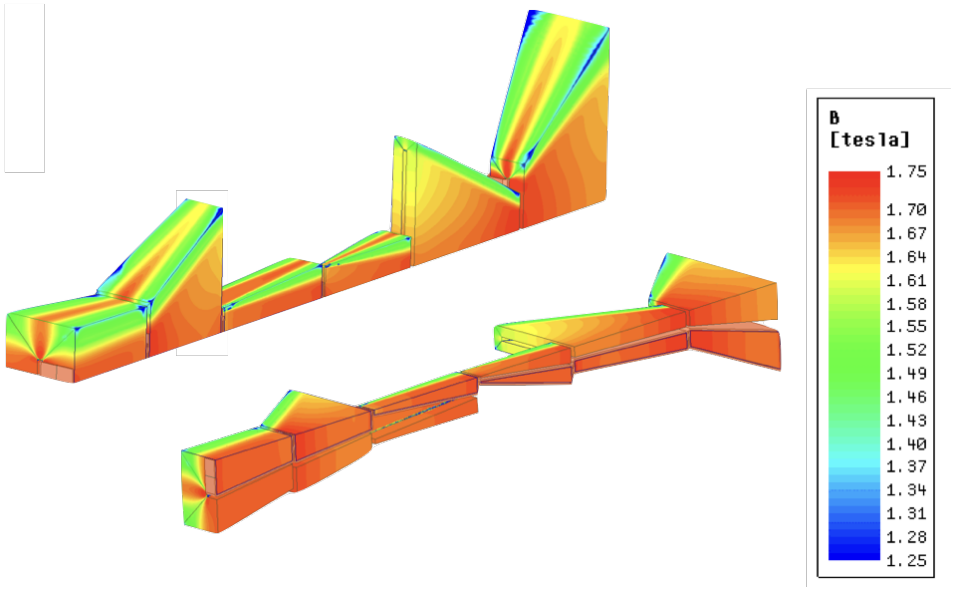

Figure 15: Modelled magnetic field distribution with nominal field intensity set to 1.7T. Quadrant cut out is shown.

The high permeability is very sensitive to high temperatures and mechanical stresses. For these reasons the design and performance of the free-standing muon shield magnets with the help of GO steel pose a number of technological challenges. These include how to best assemble sheets of GO steel without disrupting the magnetic circuit, how to cut the GO sheets into desired configurations, and how to best connect the GO sheets to achieve the desired stacking factor. In order to address these questions a prototyping campaign is underway.

The preliminary design of a magnet body entirely made from GO steel sheets is illustrated in

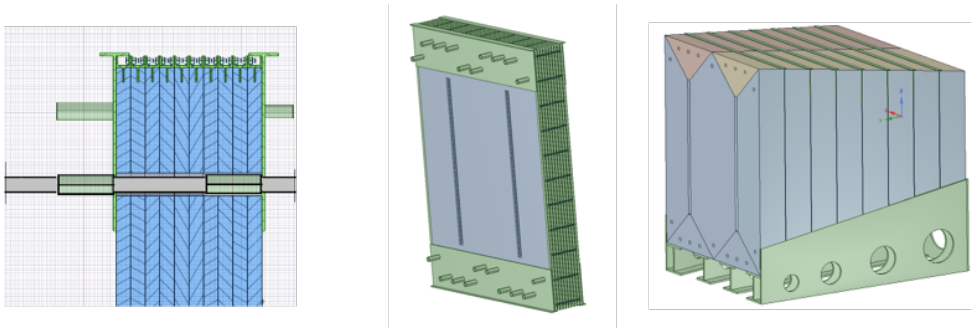

Figure 16: Preliminary mechanical design of magnets. GO steel sheets are packed into sections about 50 mm thick (left). Packs are bolted together into rectangular block about 50 cm thick (left, central). blocks of different dimensions are installed on the support beams (right).

Figure 16. It consists of 50 mm thick packs of sheets connected together by rivets, spot welding or alternatively screws. Packs are bolted together into rectangular blocks of about 50 cm depth. One block is thus made of about 1000 metal sheets of the same size. This makes mass production of such sheets reasonably cheap. Finally, blocks of different shapes are installed on the support beams. Welding by electron beam is tentatively chosen for connecting sections together. Dedicated tests have been made to measure magnetic properties of actual GO steel samples, as well as possible degradation of these properties by the welding procedure. Green lines in Figure 17 show the measured properties of the initial GO steel in the direction of and perpendicular to the grain structure. The blue line corresponds to the sample that has been welded by the electron beam. The magnetic quality of the welded sample degrades significantly. The microscopic image in Figure 18 shows the structure which appeared in the joint after the welding. An annealing process to reduce the tension and to restore the material properties was tested. Annealing at $500°C$ and at $700°C$ were separately applied to the welded test samples. It demonstrated that it was possible to recover most of the original magnetic properties of the material (Figure 17).

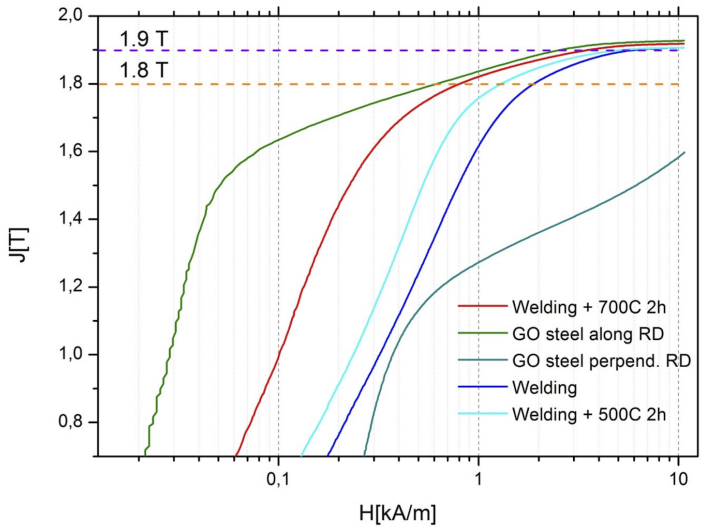

Figure 17: Measured magnetic properties of the Grain Oriented steel batch: unprocessed sample along (green) and perpendicular (dark green) to rolling direction, after the welding (blue), after the following annealing at $500°C$ (cyan) and $700°C$ (red).

The continued R&D and prototyping program aims at determining the degradation of the magnetic properties in the critical regions of the magnet in larger scale assemblies which includes the structural

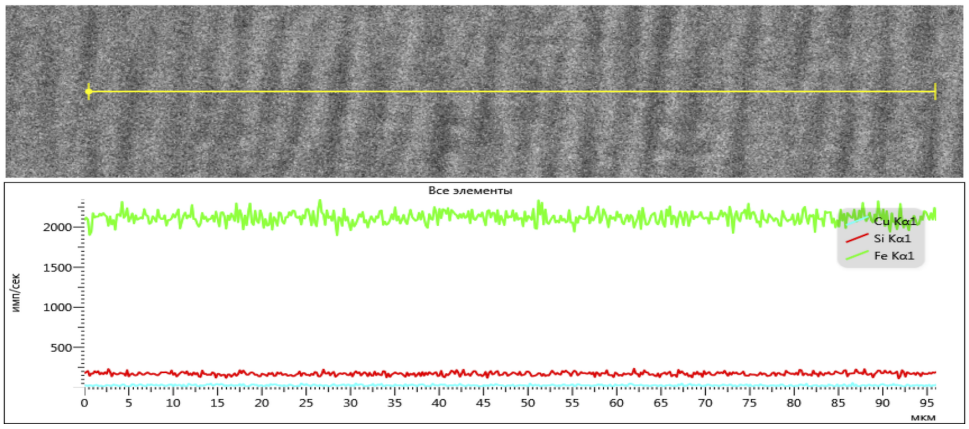

Figure 18: Carbon structure in the welded joint before the annealing.

elements. Another critical factor which requires careful consideration is the stacking factor that may be achieved in the full assemblies. Figure 19 shows the effective magnetic field in the critical volume of the first magnet of the shield by comparing the case with ideal jointing of the GO steel sheets with the case based on the measured magnetic properties of welded joints. Stacking factors of 95% and 90% have been assumed. First calculations show minor degradation of the overall magnet performance despite the relatively significant degradation of the field in the joints. The electrical current is chosen to provide an effective field of 1.7 T in the critical region.

In complement to the studies of magnet yokes constructed entirely from GO steel, a hybrid solution is also pursued with GO steel in the critical region of the magnet, surrounded by a return yoke of a normal iron with good magnetic properties.

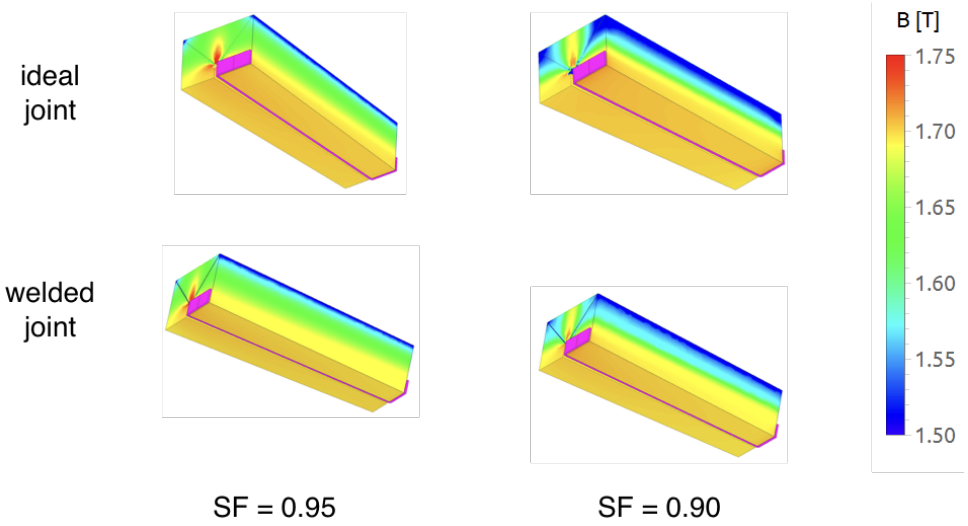

Figure 19: Modelled magnetic field map for ideal and welded joints, for stacking factors 95% and 90%. The current is set to provide effective magnetic field of 1.7 T in the critical magnet area.

2.3.2 Vacuum vessel

Deep inelastic neutrino-nucleon scattering in the detector volume leads to background events through production of V^0 particles (K_L, K_S, Λ) whose decay mimic the topology and modes of the hidden

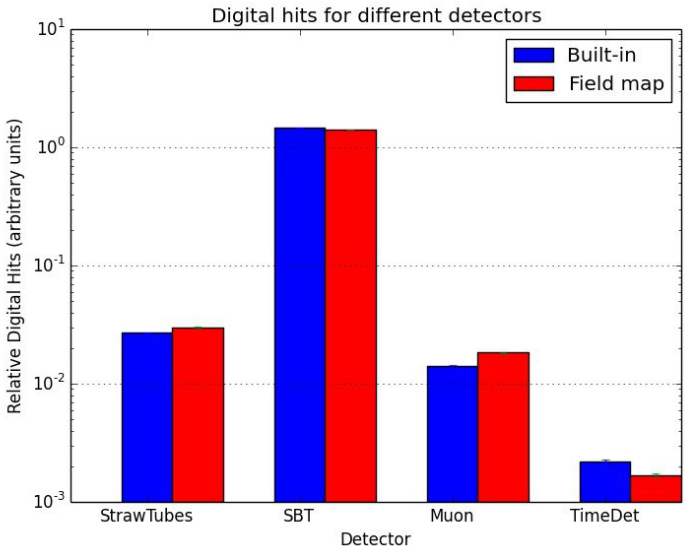

Figure 20: Simulated rates in different detectors caused by the muons which pass through the muon shield and enter into the detector acceptance. The plot compares the ideal magnetic field (red) with the realistic magnetic field (blue).

particle decays. With 2×10^{20} protons on target, a flux of $\sim 4.5 \times 10^{18}$ neutrinos and $\sim 3 \times 10^{18}$ anti-neutrinos are expected within the angular acceptance of the SHiP detector.

In order to suppress neutrino-induced background events in the fiducial decay volume, the experiment vacuum vessel is kept at a pressure of $1\,\mathrm{mbar}$. In this configuration, neutrino interactions mainly occur in the vessel walls, where they can be easily rejected by using criteria based on the reconstructed impact parameter at the proton target. Residual neutrino interactions as well as muon deep inelastic interactions with the vessel structure are further suppressed by the Surrounding Background Tagger system, which is covering the entire decay volume and which is capable of detecting the associated activity.

The SHIP vacuum vessel logically consist of two parts, the volume in which a decay vertex is accepted, and the spectrometer section. The spectrometer section runs through the spectrometer magnet and includes the four tracker stations, which are symmetrically located with two stations upstream and two downstream of the magnet. An upstream and a downstream end-cap close off the ends of the vacuum vessel.

Since the TP, the shape of the decay volume has changed to a pyramidal frustum whose parameters are primarily driven by the requirement of proximity to the proton target together with the shape of the region which is cleared from the muon flux. The length of the decay volume is mainly defined by maximising the acceptance to the different HS decay products given the transverse aperture of the spectrometer. This optimisation has arrived at a $\sim 50\,\mathrm{m}$ decay volume with upstream outer/inner dimensions of $2.2 \times 5.0\,\mathrm{m}^2/1.5 \times 4.3\,\mathrm{m}^2$, and downstream dimensions of $5.9 \times 11.9\,\mathrm{m}^2/5 \times 11\,\mathrm{m}^2$.

The decay volume vessel has undergone a thorough engineering study with a construction based on S355JO(J2/K2)W Corten steel. The design of the vessel wall was based on an optimisation aiming at producing a structure as light and as slim as possible in order to stay within the boundaries of the deflected muon flux whilst maintaining the required acceptance. The wall structure is mainly composed of an internal $20/30\,\mathrm{mm}$ thick continuous steel sheet acting as a vacuum liner reinforced by $10\,\mathrm{mm}$ thick azimuthal strengthening members. The structure is further reinforced by longitudinal stiffening profiles between the azimuthal beams. This allows maintaining a height of the stiffening members varying from $340\,\mathrm{mm}$ upstream to $390\,\mathrm{mm}$ downstream. Another shell is welded/bolted to the stiffening

members to form the compartments for the SBT liquid scintillator option, and to provide channeling of the compressive axial vacuum forces. The current model is implemented in the structural software SAP2000. The model also includes the support structure. The fixation system is designed to prevent vertical and transversal displacements of the decay volume, while allowing longitudinal displacement with the spectrometer magnet as the fixed point.

The design has been verified in terms of stresses and deformations in three different scenarios of loads, ultimate condition combination, exercise condition combination, and seismic combination. The actions from the end caps of the decay volume have been also considered in the model. The preliminary design work has been reviewed by a CERN safety engineer from the HSE group to ensure that the design accounts for the structural safety norms allowing access to the underground hall while under vacuum, and the earthquake loads in the region. Figure 21 and Figure 22 shows the structure of the decay volume.

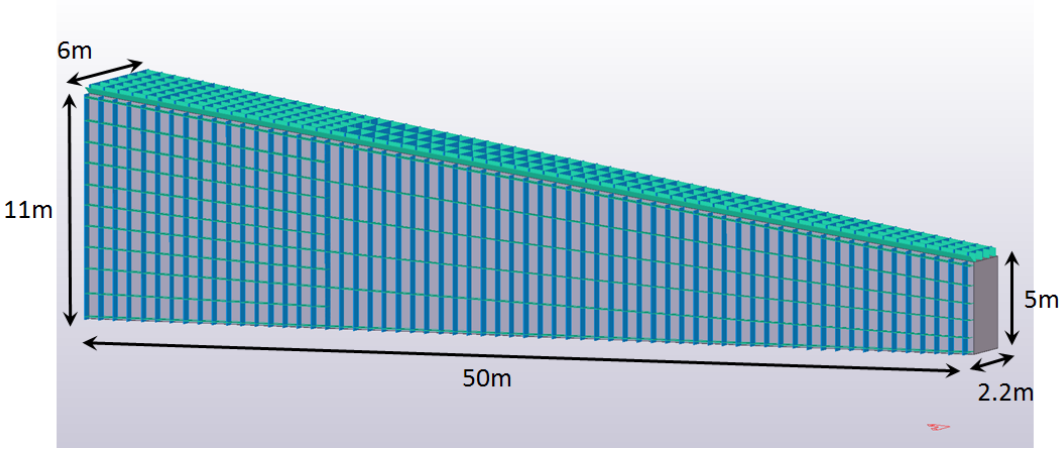

Figure 21: Overview of the structure of the decay volume showing the compartmentalization for the Surrounding Background Tagger as implemented in the Finite Element Model analysis. Outer dimensions including the walls are given.

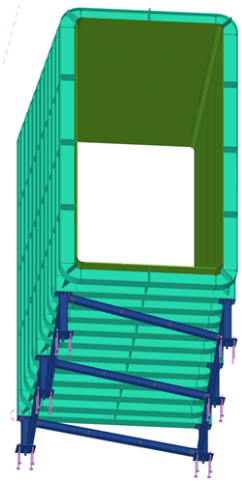

Figure 22: Cross-sectional view of the vacuum vessel. The design has been optimised in order for the wall to be as light and as slim as possible, and to incorporate a detector system which tags background events.

An external company has been involved in defining the process of manufacturing, transport, assembly and installation. A prototype module of the decay volume has been produced in order to study the performance of the SBT liquid scintillator option in a test beam at CERN (Section 5.1).

The spectrometer section has been the subject of a conceptual engineering study, including the insertion of the straw tracker and the interface with the spectrometer magnet. This section must be constructed from a non-magnetic material. For reasons of weldability, austenitic stainless steel is considered as baseline. In order to keep the weld seams small and thereby minimise deformations, a lightweight but very stiff box concept is being pursued. This allows limiting the shear force which is transmitted through the welds.

The spectrometer section vacuum tank comes in the form of two boxes. The principal task of the upstream and the downstream vacuum tank boxes is to lodge the straw tracker stations. The two boxes are nearly identical thanks to the upstream/downstream symmetry. The main difference comes from their end interfaces. The upstream box meets the decay volume, and the downstream box interfaces with the end-cap.

The vacuum tank boxes are pre-assembled in the on-site surface hall. The boxes are then slid into the aperture of the spectrometer magnet from both sides. The halfway connection is dismountable by a flange, O-ring and bolting, enabling retrieval of the boxes in case of a problem with the magnet. The yoke provides stiffening support to the vacuum tank boxes. In operation, the boxes imprison the warm magnetic coils.

A superconducting option is also under consideration for the main spectrometer magnet. The same vacuum tank box design may be used if the resulting cryostats occupy about the same volume as the warm coil packs in the present baseline.

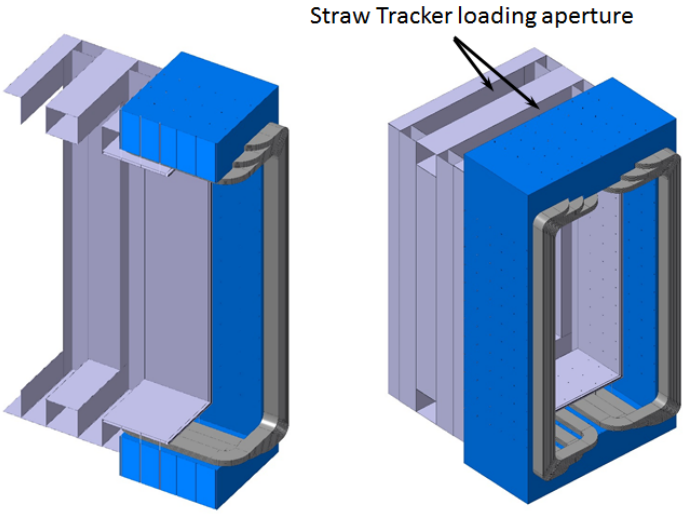

Figure 23: Conceptual views of the spectrometer magnet and the associated vacuum chamber which supports the straw tracker stations. Only the upstream vacuum chamber is shown, the downstream chamber is identical with the exception of the interface with the end-cap.

The tracker stations are designed as identical 'top loaders'. The station's principal frame is hung down from a cover plate, which corresponds to an opening in the roof of the vacuum tank. The cover plate acts as a flange, and feeds through the services of the tracker which are located in the vacuum. The vacuum tank is subjected to very large axial compressive forces under vacuum which must be channelled by the tracker cover flanges. Taken together, the precision and the management of tolerances and deformations are believed to be the main challenges in the spectrometer section project.

The vacuum volume upstream and the downstream end-caps should be as light as possible to minimise neutrino interactions upstream, and to avoid degrading the calorimetric performance downstream. A preliminary concept has been investigated based on a simple patch of extruded aluminium profiles. The end-cap material budget in this design is equivalent to 0.8 radiation lengths. The main challenge is

the need for large-scale electron welding. Currently, effort is invested on finding an alternative which splits the functions of mechanical support and tightness. In this solution the panels are bolted together while the vacuum tightness is provided by an added stainless steel liner.

The preliminary studies of the vacuum system for the approximately 2040 m^3 of total volume show that the requirements can be satisfied with a system of combined root-screw pumps, piezo and capacitance gauges for pressure monitoring, manual valves for operation and automatic valves for venting purposes [72]. A low out-gassing epoxy paint could be considered for the steel surfaces under vacuum to cover leaks and corrosion protection.

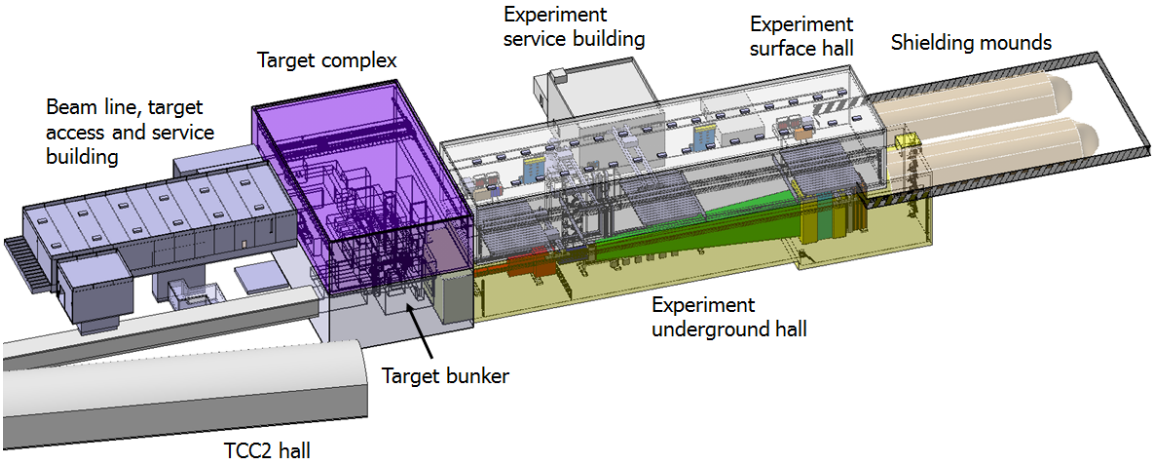

Figure 24: Overview of the experimental area.

2.4 Experimental Area

The detailed design of the experimental area (Figure 24) is mainly dictated by the requirements of the SHIP experiment as the first user of the Beam Dump Facility, but it is also taking into account future extensions and reuse. All phases of the SHiP experiment, including assembly, construction and installation, the operational phase as well as the dismantling phase, have been taken into consideration in the design, integration, and civil engineering studies.

The total length of the experimental setup is 113 m, defining the minimum length of the underground experimental hall (Figure 25). In order to reduce background from particle scattering in the cavern walls, the width of the cavern is 20 m with the detector located in the centre.

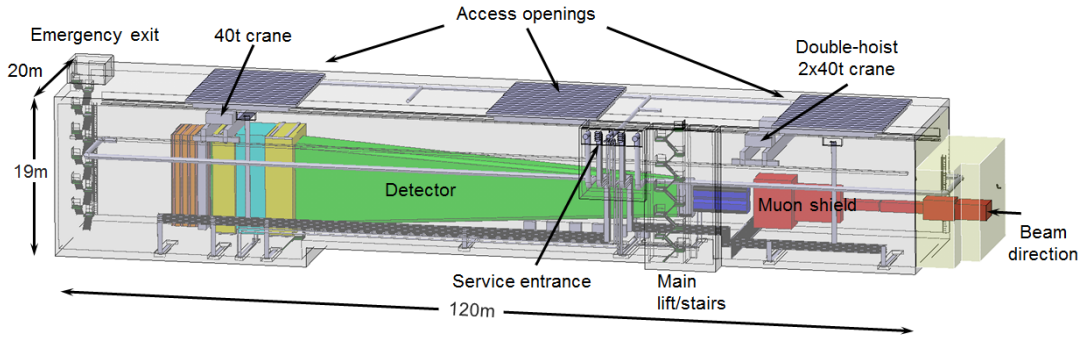

Figure 25: Overview of the underground experimental hall.

The assembly and the installation of the muon shield, the two spectrometer magnets and the vacuum vessel are considered major undertakings. They largely determine the layout of the surface hall

and the access doors (Figure 26), and the crane configuration, and drives the installation schedule. The current strategy foresees parallel construction of the muon shield magnets and the main spectrometer magnet together with its associated vacuum chamber. A large part of the assembly of both systems will take place in the underground experimental hall. This activity is followed by the construction of the upstream spectrometer magnet, and the construction of the decay volume starting from the larger end. In the current plan, the decay volume will arrive from the factory as pre-manufactured panels. The plan foresees pre-assembly of 7.5 m sections in the surface hall. This limits the number of welding operations underground, and allows other installation activities to continue in the underground hall. With the exception of the spectrometer straw tracker, all other detector elements will be assembled directly in-situ in the final location. To allow access on the side, the large detectors downstream of the spectrometer straw tracker either are installed on trolleys on floor rails, or are suspended with frames on girders. A clean room will be installed in the surface hall once the large components are installed in order to assemble the straw tracker stations before lowering them directly into position in the vacuum vessel.

A first specification of all operational detector services and space requirements have been provided to define the layout of the service building and the routing of the services, and the infrastructure systems such as the power distribution, cooling and ventilation.

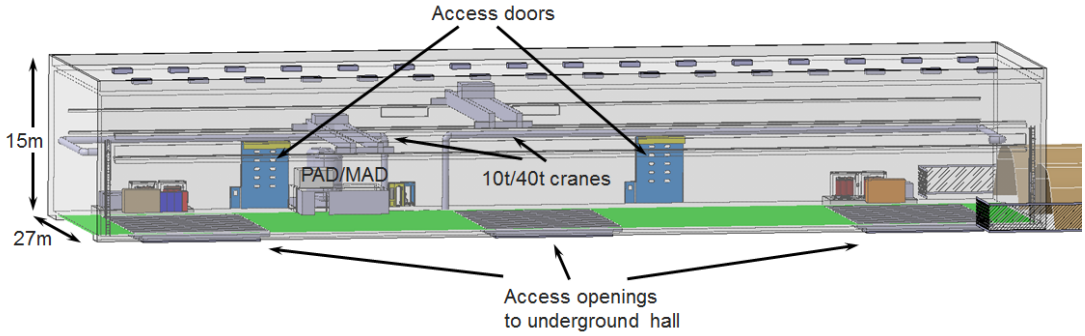

Figure 26: Overview of the surface hall with the access points for the detector installation indicated.

2.5 Potential siting of a search for Lepton Flavour Violation experiment

The BDF beam line offers a potential opportunity to host and operate in parallel an experiment ("TauFV experiment" [73]) to search for Lepton Flavour Violation and rare decays. Using a thin target consisting of several narrow blades spaced by a few centimeters, and intercepting about 2% of the intensity delivered to the SHiP target, the experiment would have access to close to 8×10^{13} tau lepton and $5 \times 10^{15} D^0$ meson decays. The detector under study consists of a $7.5\,\mathrm{m}$ long and $3\,\mathrm{m}$ wide spectrometer including a vertex detector, tracker, fast timing detector, electromagnetic calorimeter and muon system.

From the beam optics point of view, several locations can provide the required beam conditions and the beam drift space to accommodate the detector along the new $165\,\mathrm{m}$ transfer tunnel between the TDC2 switch yard cavern and the BDF target station without affecting the location of the BDF experimental area and without significant changes to the configuration of the beam line. The choice is instead driven by considerations related to the civil engineering in the vicinity of the existing installations, radiological protection, and to access and transport requirements above ground and underground. The preferred location under study is situated $100\,\mathrm{m}$ upstream of the BDF target bunker. Simulation studies are required to understand the influence on the SHiP experiment in terms of background.

3 Simulation and Reconstruction

The software framework adopted by SHiP is based on FairRoot [74] and called FairShip. FairRoot is an ideal turn-key solution for small (and large) experiments that do not have enough person power for a full fledged computing group, or for experiments that do not see the need to develop their own offline computing framework. It is fully based on the ROOT system. The FairShip code is largely a specialization of the generic C++ base classes provided by FairRoot, mainly profiting from the methods to describe the detector geometry, implement detector classes, and performing simulation. In addition some specific auxiliary libraries needed by SHiP are included, like GENFIT for reconstruction of tracks. The steering of the simulation flow, and the main parts of the reconstruction and analysis is based on Python classes and functions. FairShip moved recently to using `aliBuild` (https://alisw.github.io/alibuild), a simple build tool developed by the ALICE collaboration. FairShip is regularly updated following the software improvements of the external packages. The current versions of the principal external packages are ROOT v6-14-00, GEANT4 v10.3.2, GEANT4_VMC v3.6, GENIE v2.12.6, PYTHIA8 v8230, and EVTGEN R01-06-00.

3.1 Simulation

The simulation of the proton collisions with the fixed-target is done in two steps. First, primary proton interactions are simulated using PYTHIA8 [75]. Then the particles produced are transported through the target and the experimental setup using GEANT4 [76]. Some rare processes which produce muons with relatively high momenta, such as decays of light vector mesons, γ-conversions and positron annihilation, are disabled by default in GEANT4. These have been enabled and their rates artificially boosted by an arbitrary factor of hundred for further studies.

For the heavy quark production a procedure was developed to also simulate charm and beauty hadron production by the products of the primary proton-nucleon collision [77]. This increases the expected yield compared to the prediction in the TP by a factor of 2.6 and 1.9 in the detector acceptance for HNLs with mass of $1\,\mathrm{GeV}/c^2$ and $3\,\mathrm{GeV}/c^2$, respectively.

In total 6.5×10^{10} protons on target have been simulated with an energy cut for transporting particles after the hadron absorber of $10\,\mathrm{GeV}$, and 1.8×10^9 protons on target with an energy cut of $1\,\mathrm{GeV}$. The samples produced with charm and beauty hadrons correspond to about 100×10^9 protons on target.

Since the TP the simulation of the signals in FairShip has been updated and extended to more physics models. This allows simulating the hidden particles in the SHiP experimental setup with realistic reconstruction and analysis. Figure 27 - 29 show examples of reconstructed observables for different decay modes of $1\,\mathrm{GeV}/c^2$ HNLs, demonstrating that the selection efficiency used for the SHiP sensitivies (Table 5) is close to 100% for signal events. Figure 28 has been produced with the TP version of the ECAL.

The production and decay of HNLs have been considerably improved according to [78]. Dark scalar production and decay have been implemented. Inclusive decays of dark scalars are considered using the inclusive $b \to SX_s$ branching fraction given in [79]. The production of dark photons via meson decays, proton bremsstrahlung and QCD production has been implemented together with their decays. The contribution from cascade production, which is included for the HNL and the dark scalar, is not currently taken into account for the dark photon. A set of benchmarks are considered where the production is dominated by charm and beauty hadrons, and the final states consist of different multi-body final states involving at least two charged particles. All signal sensitivity curves presented in Chapter 6, except for the axion-like particles, have been obtained using the FairShip framework.

The SHiP experiment critically depends on an accurate simulation of the background components, in particular the design of the muon shield relies on an accurate knowledge of the muon flux. Figure 30 and Figure 31 show the muon spectrum and the exit point of the muons after the hadron absorber. In the

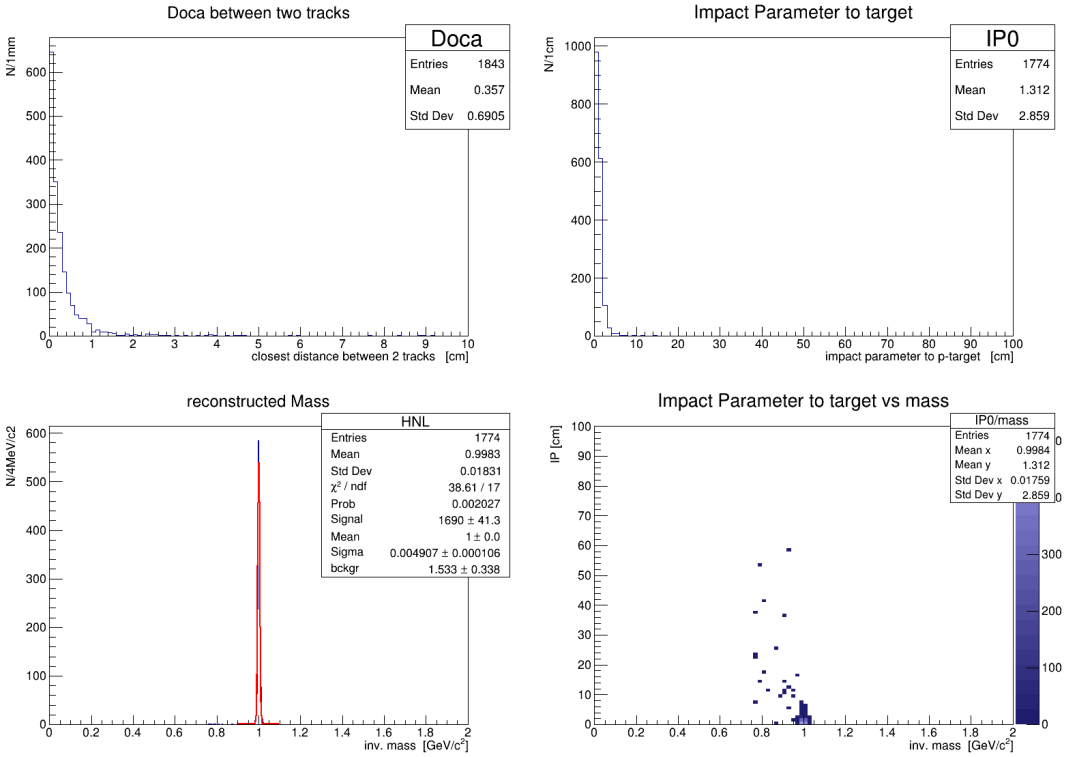

Figure 27: Reconstruction of 1 GeV/c^2 HNL $\rightarrow \mu^- \pi^+$.

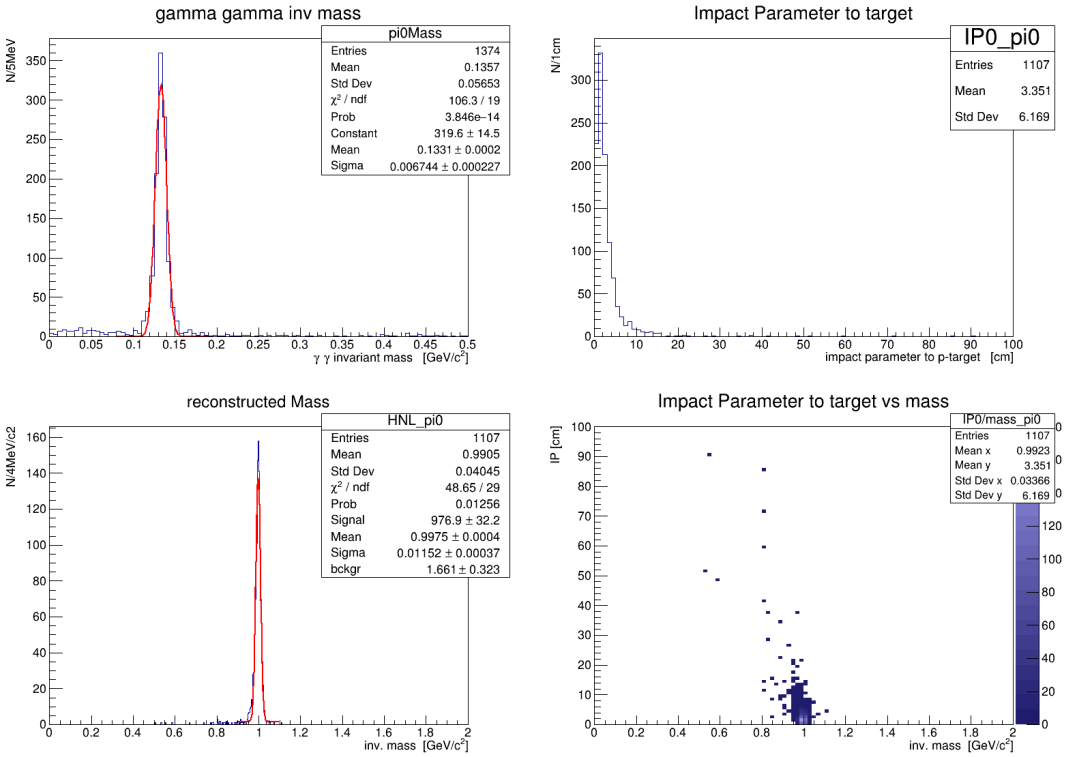

Figure 28: Reconstruction of 1 GeV/c^2 HNL $\rightarrow \mu^- \rho^+ (\rightarrow \pi^+ \pi^0 (\rightarrow \gamma\gamma))$.

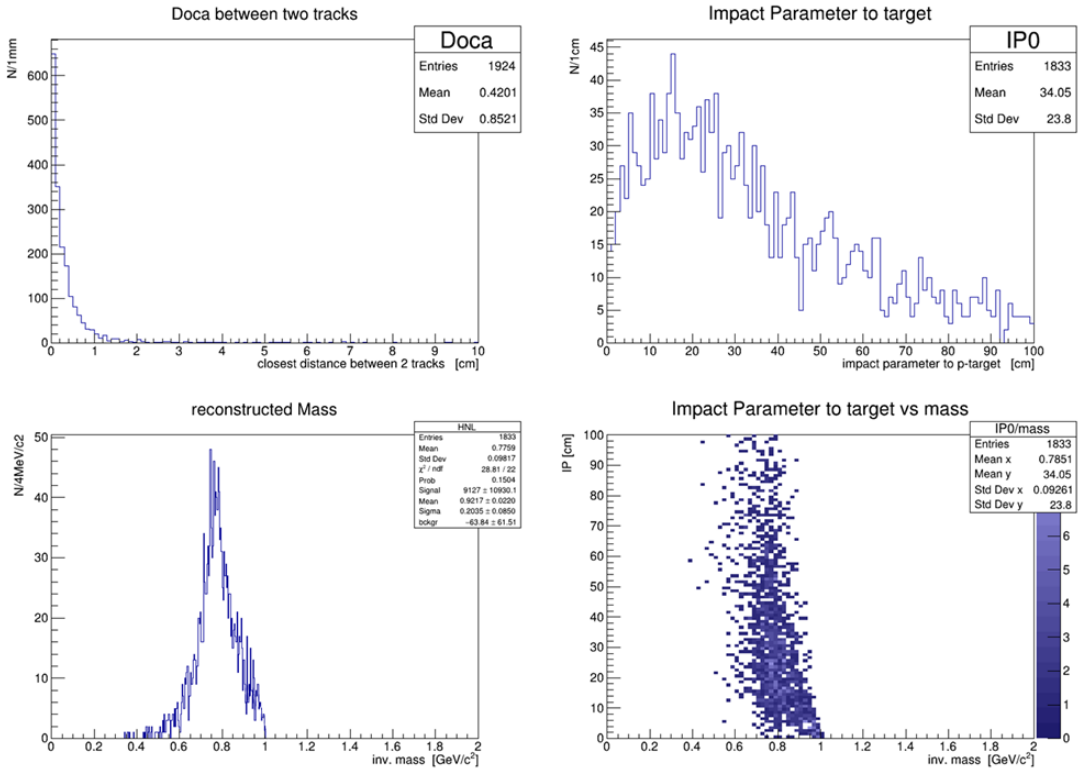

Figure 29: Reconstruction of 1 GeV/c^2 HNL $\to \nu\rho^0(\to \pi^+\pi^-)$.

TP [3], the validity of the simulation was verified by comparing simulation predictions to data from the CHARM beam-dump experiment at CERN [80]. The experimental and the simulated data were found to be in good agreement.

Further tests have been made since the TP. The multiple scattering as implemented in the GEANT4 version (v10.3.2) currently employed in the FairShip simulation has been compared to existing data and other models [81]. As shown in Figure 32 good agreement is found. Catastrophic energy loss by a muon in the SHiP active muon shield can drastically change its trajectory and divert it towards the SHiP decay volume. The catastrophic energy loss of muons in the NA62 liquid krypton calorimeter as measured by the NA62 collaboration [82] has been compared to a simulation with FairShip. The GEANT4 setup consists of a 125 cm thick block of liquid krypton. Muons are shot at the block, and the energy deposited in the block is summed up. As Figure 33 shows, reasonable agreement between simulation and data is found given the simplistic detector setup used. It should be noted that the mean energy deposited in the liquid krypton does not agree with the mean energy loss expected for muons (right plot) due to leakage.

Despite the relatively good agreement between the simulation and available data, more cross checks are needed with experimental setups which are closer to the phase space where SHiP operates to increase the confidence in the simulation. The most realistic cross-check is being performed with the data obtained by a dedicated experimental setup in the CERN North Area to measure directly the rate and momentum of muons produced by 400 GeV/c protons impinging on a replica of the SHiP target after 2.4 m of iron [70] (Section 3.4.1). The reconstruction and the analysis of the data use the FairShip software.

3.2 SHiP detector setup in the simulation

Since the Technical Proposal the detector descriptions in the simulation have been optimized and refined. Additional classes were added to realistically describe the digitized data of the sub-detectors. A frame-

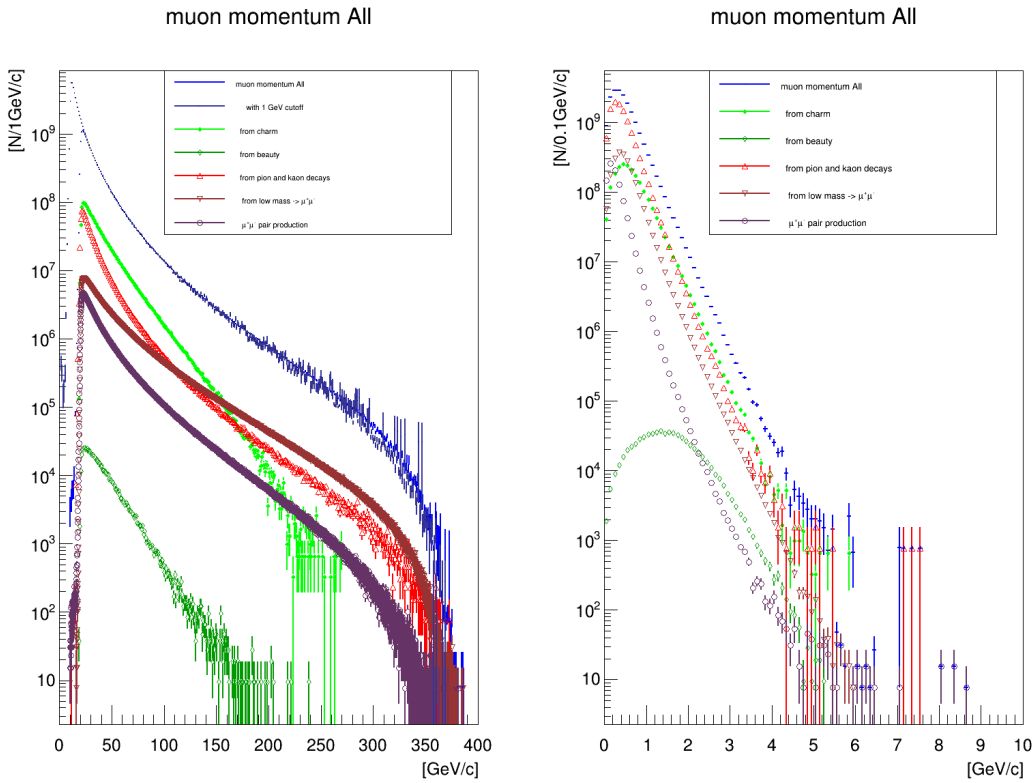

Figure 30: Momentum distributions of muons leaving the hadron absorber, total momentum (left) and transverse momentum (right). Different contributions are shown. The rates are normalized to 5×10^{13} protons on target.

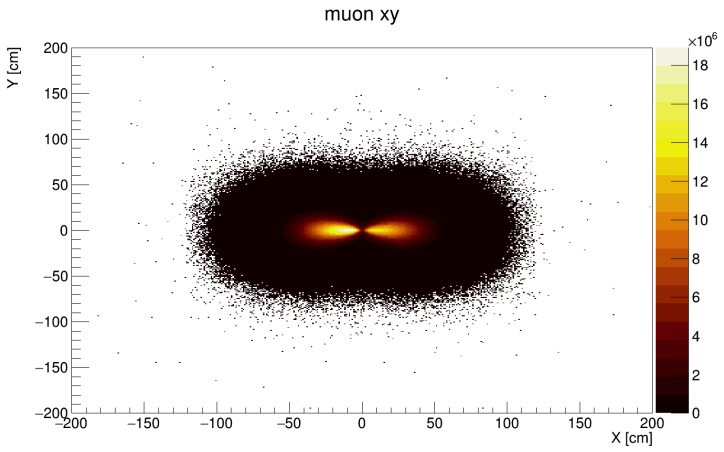

Figure 31: Position of muons leaving the magnetized hadron absorber.

work has been implemented to deal with global and local magnetic field maps, either in form of tables or parametrised functions. Below is a summary of the major modifications.

The active muon shield has been optimized for the frustum-shaped detector setup. Realistic field maps, obtained from a magnetic field simulation with the OPERA package instead of uniform fields, have been implemented (Section 2.3.1).

The layout of the Scattering and Neutrino Detector has been updated (Section 4). The associated muon identification system has replaced the Upstream Veto Tagger to provide tagging of neutrino in-

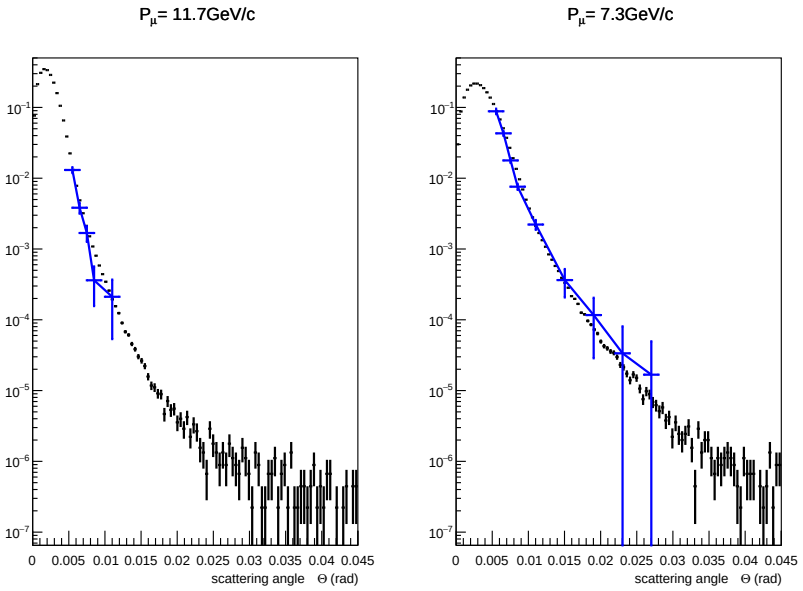

Figure 32: Comparison of the GEANT4 Monte Carlo simulation to data-sets from the HYPERON setup [83] at IHEP with muons at 11.7 GeV/c (left) and 7.3 GeV/c (right) impinging on a copper block. Blue points are the measurements, black points are from the FairShip simulation.

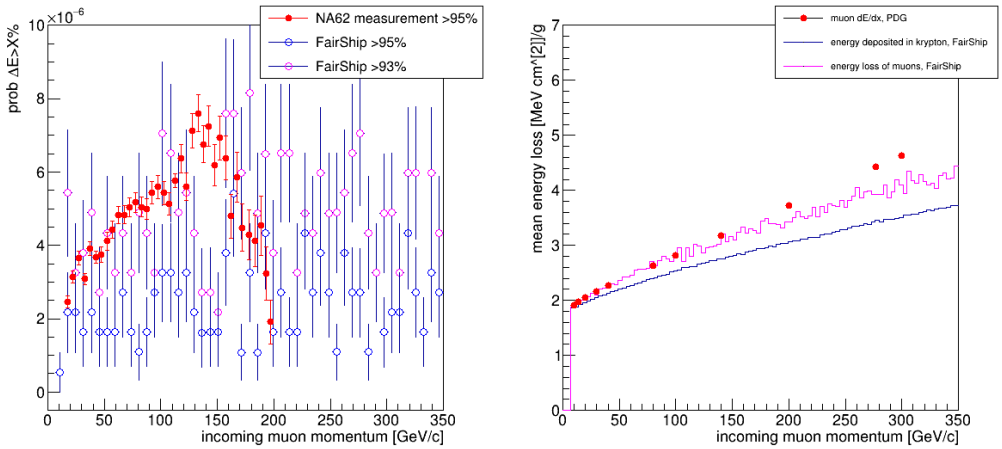

Figure 33: Left: probability that a muon releases more than 95% of its energy in the liquid krypton calorimeter, as a function of the muon momentum in GeV/c. Red points are the NA62 measurements, blue points are from the FairShip simulation, and magenta points are from FairShip with >93%. Right: mean energy loss as function of muon momentum. Note that the energy deposited in the krypton is less than the energy loss of a muon. At higher energies, mean energy loss is lower than expected. More studies can be done with a dedicated test beam setup to measure directly the energy loss of muons in iron, which is the most relevant for SHiP.

teractions in the material upstream of the decay volume that could produce long-lived neutral particles which in turn may decay and mimic a HS signal in the Decay Spectrometer. The in-vacuum upstream Straw Veto Tagger has been removed as it was found to bring a negligible contribution to the background suppression. Information from the vertex reconstruction with the decay spectrometer is sufficient to veto background from K_S decays. The SBT has now a realistic detector granularity corresponding to the structural design of the vacuum vessel. In addition to the layout with a liquid scintillator, an alternative layout with a solid plastic scintillator has also been implemented. The current Spectrometer Straw Tracker design is based on straw tubes with $20\,\mathrm{mm}$ diameter, while the original TP design (Section 5.2) had $10\,\mathrm{mm}$ tubes. The corresponding baseline straw geometry was reoptimized for high hit detection efficiency. It is implemented in FairShip as the default SST geometry. All tracker stations have now the same dimensions to simplify the engineering of the straw tracker supports and the vacuum chamber of the spectrometer section. The structural support material has been added to the simulation. A detailed field map for the spectrometer magnet from an OPERA simulation, including the return field, has been implemented.

Track finding based on Template Matching Pattern Recognition was used to evaluate the SST performance as a function of the straw diameter. Table 1 compares the track recognition efficiency, fake track rate and relative momentum resolution obtained for muon and pion tracks in the SST acceptance and originating from simulated decays of HNLs with a mass of $1\,\mathrm{GeV}/c^2$. As shown, the 6% loss in recognition efficiency when going from $10\,\mathrm{mm}$ to $20\,\mathrm{mm}$, is considered recoverable by using more complex pattern recognition techniques, such as Hough Transform and Artificial Retina. The slightly increased rates of clones is not an issue.

Method	Recognition efficiency, %	Clone rate, %	Ghost rate, %	$\frac{P-P_{true}}{P_{true}}$, %	$\frac{P_T-P_{T\,true}}{P_{T\,true}}$, %	Track purity, %
Inner straw diameter = 1.975 cm						
Template matching	89.7 ± 0.2	0	1.23 ± 0.08	-0.3 (μ) 2.3 (σ)	-0.2 (μ) 2.5 (σ)	99.24 ± 0.02
Hough transform	98.12 ± 0.09	0.59 ± 0.05	2.1 ± 0.1	-0.2 (μ) 2.0 (σ)	-0.2 (μ) 2.4 (σ)	99.47 ± 0.01
Artificial retina	99.04 ± 0.07	0.08 ± 0.02	1.12 ± 0.07	-0.2 (μ) 1.9 (σ)	-0.2 (μ) 2.2 (σ)	99.88 ± 0.01
Inner straw diameter = 0.975 cm						
Template matching	95.7 ± 0.1	0	1.21 ± 0.07	-0.2 (μ) 1.6 (σ)	-0.2 (μ) 2.0 (σ)	99.40 ± 0.02
Hough transform	99.04 ± 0.07	1.27 ± 0.08	1.92 ± 0.09	-0.2 (μ) 1.7 (σ)	-0.3 (μ) 2.1 (σ)	99.40 ± 0.02
Artificial retina	98.99 ± 0.07	0.38 ± 0.04	1.27 ± 0.08	-0.2 (μ) 1.5 (σ)	-0.2 (μ) 2.0 (σ)	99.82 ± 0.01

Table 1: Quality metric for different track pattern recognition techniques for two different straw tubes inner diameters.

The optimization of the SST geometry for the best track detection performance is ongoing. FairShip simulation is used to study the influence on the pattern recognition performance of a single view geometry, longitudinal distances between stations and stereo angle. Realistic simulation of the signal timing as function of the straw hit position is under development. The GARFIELD-based parameterisation of the drift time distributions as a function of the track local coordinates for ideal and misaligned straws was found to be in a reasonable agreement with results from beam test measurements. Parameterised dependencies of the most probable signal arrival time and the corresponding time resolution have been prepared for the upcoming version of FairShip.

The segmentation of the Timing Detector, and proper simulation of the expected timing resolution, has been added. Implementation of the alternative option based on MRPC is underway. An alternative option for the electromagnetic calorimeter with pointing capabilities has been added to the simulation, called SplitCal (Section 5.4). Performance studies are ongoing. The hadronic calorimeter has been removed as it has been found that the SplitCal should be capable of providing sufficient identification for low momentum particles. The material of the hadronic calorimeter is kept at the first filter wall for the muon system. The scintillating tile option has been implemented as baseline in FairShip for the downstream muon system.

3.3 Reconstruction

Different pattern recognition algorithms for the straw tracker reconstruction have been implemented and used to study the effects of detector modifications on the tracking efficiency. The reconstruction of signal with charged particles has been extended to include reconstruction of photons with the new SplitCal version of the ECAL detector. The energy of a photon is taken from the reconstructed cluster while the direction is given by the vertex of two charged tracks and the cluster position in the ECAL.

3.4 Validation of the SHiP simulation in test beam

3.4.1 Measurement of the muon spectrum

In order to validate the SHiP Monte Carlo simulation, the collaboration requested three weeks of beam time in 2018 with the aim of collecting $\mathcal{O}(5 \times 10^{11})$ 400 GeV protons on target and accurately measure the muon flux emanating from the SHiP target [70]. A 10×154.3 cm^3 cylindrical replica of the SHiP target with exactly the same configuration of TZM and W blocks as in the planned SHiP target [6] was installed in the H4 beam line at the CERN SPS.

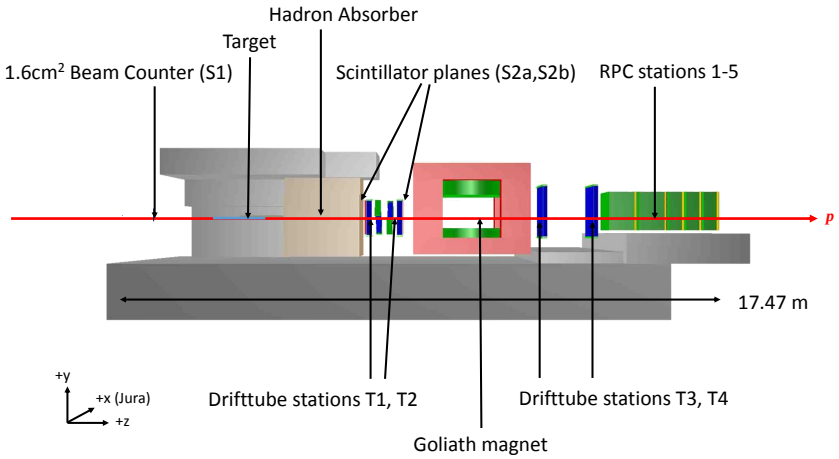

Figure 34: Layout of the spectrometer to measure the μ-flux

The experimental test setup as implemented in FairShip is shown in Figure 34. A 2.4 m hadron absorber made of iron was placed downstream of the target. The shielding of the target by iron and concrete blocks allowed operating the experiment at a 20 times higher than the normal intensity at the SPS H4 beam-line, i.e. at 2×10^7 protons on target per spill. To measure the momentum spectrum a spectrometer consisting of drift tubes stations for tracking, and RPC detectors together with muon filter walls for muon tagging, was installed around the Goliath magnet. In order to perform an accurate measurement of the spectrum, the Goliath field was mapped through a scan earlier in the year [84]. The target and the experimental setup seen from behind are shown in Figure 35.

The total number of protons collected on target has been estimated to $\sim 6 \times 10^{11}$. Data was collected for several settings of the Goliath magnet:

- Default configuration: Maximum field = 1.5 T, 5.3×10^{11} protons on target.
- Medium field configuration: Maximum field = 1.0 T, 4.8×10^{10} protons on target to enhance precision for low momentum muons.
- Field off configuration: 2.7×10^{10} protons on target for alignment purposes.

The analysis of the data is ongoing. The large simulation sample of muons generated for the SHiP studies will be used in the analysis by processing them with the geometry of the muon flux measurement. Figure 36 shows a reconstructed muon trajectory in the experimental setup as implemented in FairShip (left), and an example of an event reconstructed online (right).

Figure 35: Replica of the SHiP target and the experimental setup as seen from behind.

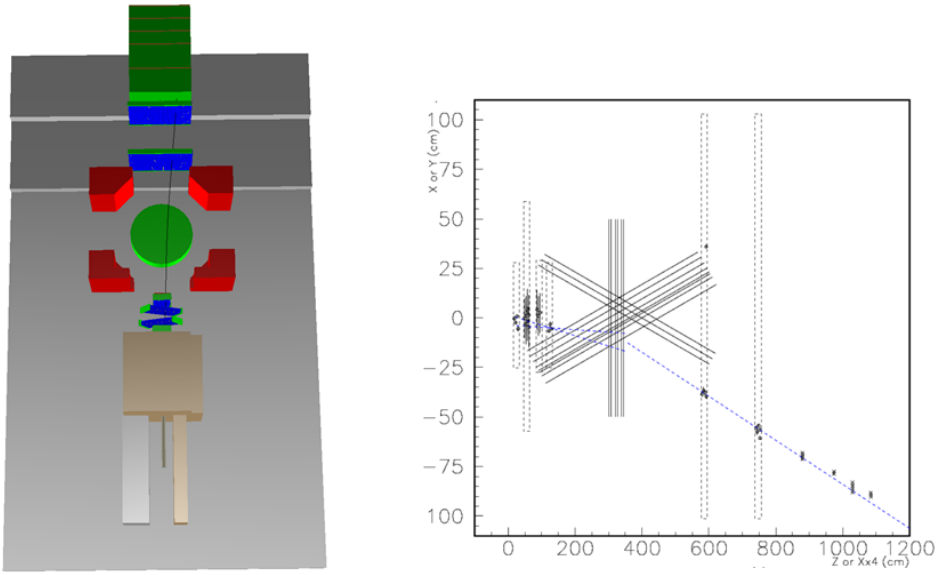

Figure 36: Muon flux test beam setup in FairShip with a reconstructued track reconstructed (left) and an example of an event reconstructed online during data taking (right).

3.4.2 Measurement of charm production in a thick target

The knowledge of the total charm production yield in 400 GeV proton interactions on the SHiP target is essential for the experiment, both in establishing the SHiP sensitivity to detect new particles that could be produced in charm decays, and in making a precise estimate of the tau neutrino flux produced in

D_s decays. In particular the cascade production of charm from primary protons which initially undergo elastic scattering, and from secondary hadrons interacting inelastically, has never been measured. SHiP aims at measuring the differential charm production cross section in a thick target, including the cascade production. The measurement is also of interest for QCD. In parallel to this measurement, an effort is ongoing to progress on the theoretical prediction and tune the next-to-leading order calculation.

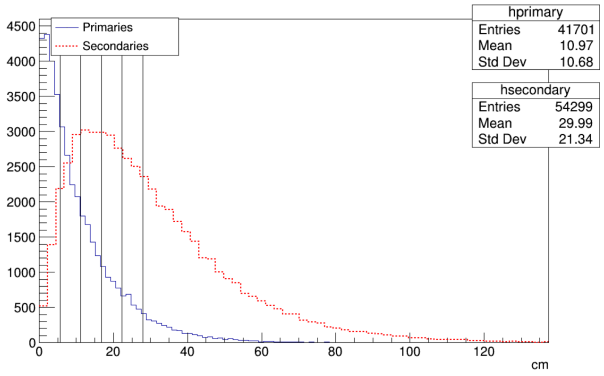

Figure 37: Distribution along the z-axis of charmed hadrons production vertices in a lead target.

An optimization run, aiming at collecting about 10% of the total statistics foreseen for the final measurement planned after LS2, was performed at the H4 beam line by modifying the muon flux set-up in the last week of the July 2018 SHiP run. Figure 37 shows the position distribution along the beam direction of primary and secondary charmed hadron production vertices in a lead target, as obtained from simulation [77]. The interaction length in lead is 17.6 cm. Since the number of produced charmed hadrons falls rapidly along the length of the target, the measurement focused on the first $\sim$1.6 interaction lengths.

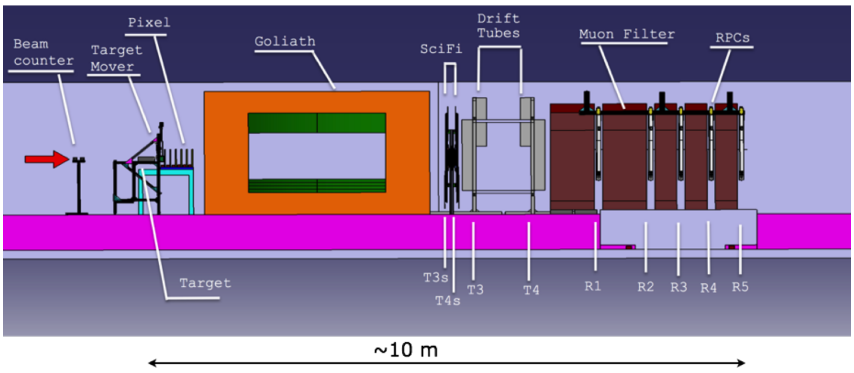

Figure 38: Lateral view of the experimental apparatus for the charm measurement.

The layout of the SHiP-charm detector is shown in Figure 38. The SHiP replica target was replaced by a lead target instrumented with Emulsion Cloud Chambers (ECC), in this case 1 mm-thick lead plates interleaved with nuclear emulsion films, allowing the detection of both the production and decay of the charmed hadrons in the target. A motorised precision table was used to move the ECC target in the transverse plane, thus allowing to distribute the very narrow beam on the whole emulsion surface.

In order to cope with the high multiplicity of tracks produced by the electromagnetic and hadronic showers, the drift tubes stations between the target and the Goliath magnet were replaced by a pixel detector system. The measurement of the track slope downstream of Goliath was performed by two SciFi stations in the high occupancy region and the drift tube stations in the external regions. Both the

muon flux and the charm measurement used the muon tagger system based on the RPCs for identification and extended tracking.

The target was assembled in six different configurations in order to study the charm production in different portions of the target. In total data from 16×10^5 protons on target were collected during the optimization run.

The analysis of the data is in progress. The first phase is devoted to the calibration and local reconstruction of tracks. In the second phase the alignment of the different sub-detectors will be performed and the data will be imported into FairShip for the overall event reconstruction.

In parallel, the analysis of the emulsion films is being performed with the new high-speed scanning systems, having an angular acceptance up to tan(θ)=1 [85–87]. First proton interaction vertices have been reconstructed, as shown in Figure 39.

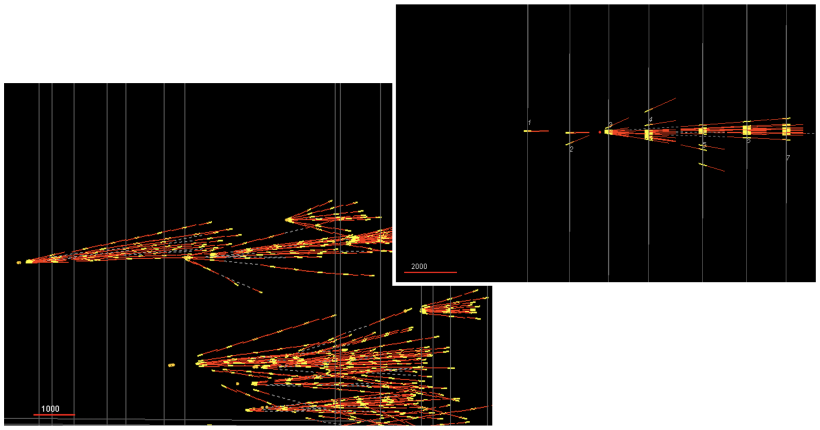

Figure 39: Proton interaction vertices reconstructed in the ECC brick.

4 Scattering and Neutrino Detector

The Scattering and Neutrino Detector (SND) has undergone a major revision since the Technical Proposal. In particular, the updated, shorter, Muon Shield has driven the optimisation of the detector configuration. The muon flux immediately downstream of the last magnet of the Muon Shield is shown in the left plot of Figure 40. The hourglass-shaped region delineates the area in the transverse plane which is cleared from the bulk of the muon flux, and, which in turn defines the allowed region for the detector. While the re-optimized version of the Muon Shield allows locating the SHiP detectors significantly closer to the proton target, the available lateral space for the SND has changed from a width of $\sim$4.5 m to $\sim$3 m. On the other hand, the neutrino flux and neutrino energy decreases with larger polar angles. This produces the radial dependence of the neutrino interaction yield shown in the right plot of Figure 40, favouring the development of a narrow and long emulsion target.

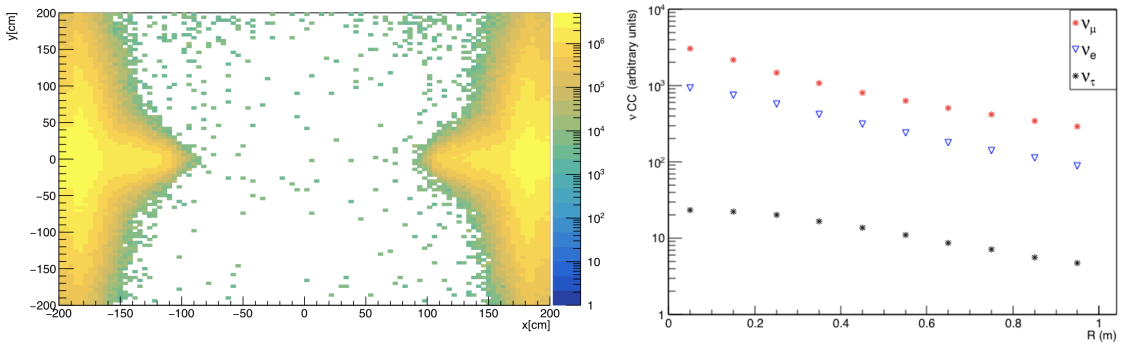

(a) (b)

Figure 40: (a) Muon flux distribution in the transverse plane immediately downstream of the last sweeper magnet. (b) Yield of the three neutrino species as a function of the distance from the beam axis.

Consequently, the optimisation of the spectrometer has resulted in an emulsion target with dimensions of 80×80 cm^2 in the transverse plane, and $\sim$3 m in length. The new geometry makes it advantageous to merge the two magnetised regions in the original design, and measure the momenta of both hadrons and muons in a single spectrometer, followed by a simplified muon identification system. Figure 41 shows the new configuration of the Scattering and Neutrino Detector, as implemented in the FairShip simulation. The new design consists of a $\sim$7 m long magnet providing a 1.2 T horizontal magnetic field. The magnet hosts the Emulsion Target, interleaved with the Target Tracker planes, and a Downstream Tracker. The emulsion target has a modular structure: the unit cell consists of an Emulsion Cloud Chamber (ECC) made of lead plates interleaved with nuclear emulsion films, followed by a Compact Emulsion Spectrometer (CES) for the momentum and charge measurement of particles produced in neutrino interactions. The ECC bricks are arranged in walls alternated with Target Tracker planes, providing the time stamp of the interactions occurring in the target. The Downstream Tracker is made of three Target Tracker planes separated by $\sim$50 cm air gaps. It is used to measure the charge and momentum of muons exiting the target region, thus extending significantly the detectable momentum range of the CES. The Muon Tracker planes also help to connect the tracks in the emulsion films with the downstream muon identification system.

The muon identification system is made of a sequence of iron filters and RPC planes, totalling about two metres in length. The system also has the role of tagging neutrino interactions in its material which could lead to long-lived neutral particles entering the downstream HS decay volume and mimicking signal events.

Both in terms of charge measurement and muon identification, the new, more compact design of the SND shows performance comparable with the TP version. While the CES is efficient at lower momenta, the Downstream Tracker is tailored to measure the charge and momentum of muons above

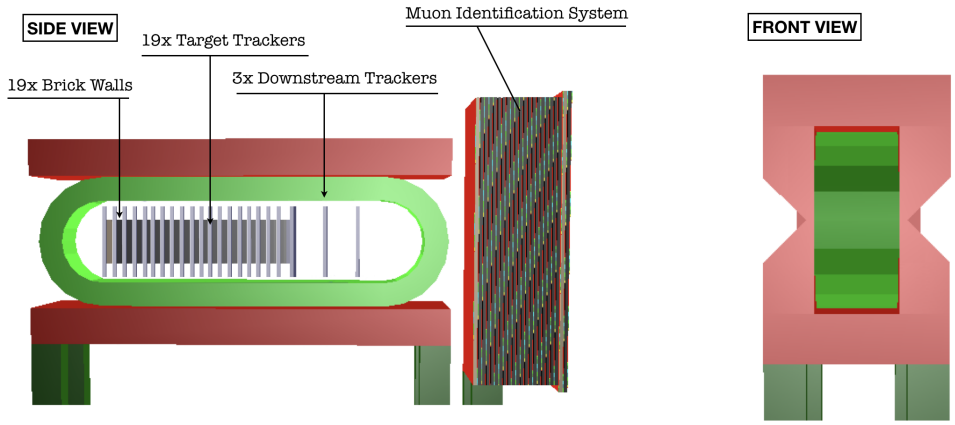

Figure 41: Schematic layout of the Scattering and Neutrino Detector (SND).

10 GeV/c. The combination of the two detectors provides a total charge identification efficiency of $\epsilon_{charge} = (65.7 \pm 0.5)\%$ for muons produced in ν_μ CC interactions. The geometrical acceptance of the muon identification system is 74.8% and the efficiency of the muon identification is $\epsilon_\mu^{ID} = 96.7\%$ with a mis-identication of hadrons of 1.5%.

Below is a more detailed description of each subsystem.

4.1 SND spectrometer magnet

The design of the SND magnet follows the need for a large magnetised volume ($\sim$1$\times$1.6$\times$6.4 m^3) with a field higher than 1.2 T, and which is capable of accommodating the Emulsion Target, the Target Trackers and the Downstream Tracker. At the same time, the yoke must be designed to produce a low stray field to avoid interfering with the muon background flux on the sides of the magnet.

Different options for the coil have been considered (warm aluminum and copper, and high and low temperature superconducting). Requirements on the access and maintenance as well as constraints from the associated detectors suggest that the better option is a warm magnet. As the nuclear emulsion requires an ambient temperature of $\sim 18^\circ$C, the coils have been designed with an active cooling system. CERN standards for the power supply and cooling system have been used. A schematic overview of the magnet, with the coil, the iron yoke, targets and detectors and part of the mechanical structures is shown in Figure 42. Table 2 summarises the design characteristics of the magnet.

The design of the magnet has been based on magnetic simulation, and 3D mechanical and thermal analysis. Figure 43 shows results from the analyses. The designed coil (copper/aluminum option) has a nominal cross-section of 0.41 m^2 and a fill factor of 0.68/0.73, respectively, and produces a uniform magnetic field of 1.25 T with $\Delta B/B < 1\%$ in the detector volume. The mechanical stresses as a result of the magnetic forces at the bends are $\sim$5 MPa according to Von Mises yield criterion. This is compatible with the yield strength of both copper and aluminum. From the electrical point of view, the coil has 96/72 turns for copper and aluminum respectively, operated with a supply current of 10.9/14.6 kA and a voltage drop of 128/139 V.

The iron yoke has a thickness of 0.6 m. The stray field laterally is below 1%, 17 mT in the worst case and 5 mT on the average. The mechanical stress within the yoke is estimated to be $\sim$6.7 MPa, thus

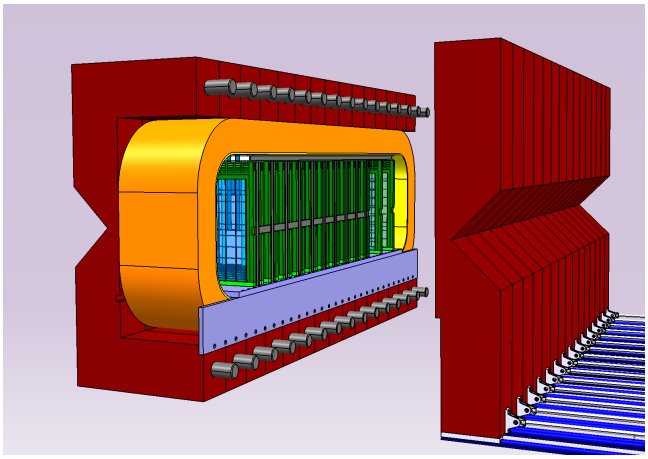

Figure 42: Schematic layout of the SND magnet.

largely within the strength limit defined by the standard UNI EN 10025 iron. The coil water cooling was investigated for both copper and aluminum solutions. Assuming the CERN standard for input/output temperatures of $30°C/50°C$, a flow rate $63/121$ l/min is required. The pressure drop is estimated to be $1.93/6.1$ bar. An additional 22 mm thick thermal shield of aluminium fitted to the inside of magnet is required to guarantee the required temperature for the detectors. It will be cooled with an average coolant temperature at $18°C$ and a maximum variation of $0.4°C$, requiring a refrigerator power of about 24 kW.

	Cu	Al
Reference B field	1.25	1.25
Overall ampere turns (MA)	1.05	1.05
Net coil volume (m^3)	4.3	4.6
Iron yoke volume (m^3)	36.0	36.0
Total magnet mass (tonnes)	300	275
Reference electrical power (MW)	1.32	1.90

Table 2: Summary of the design characteristics for the copper and aluminum coil options.

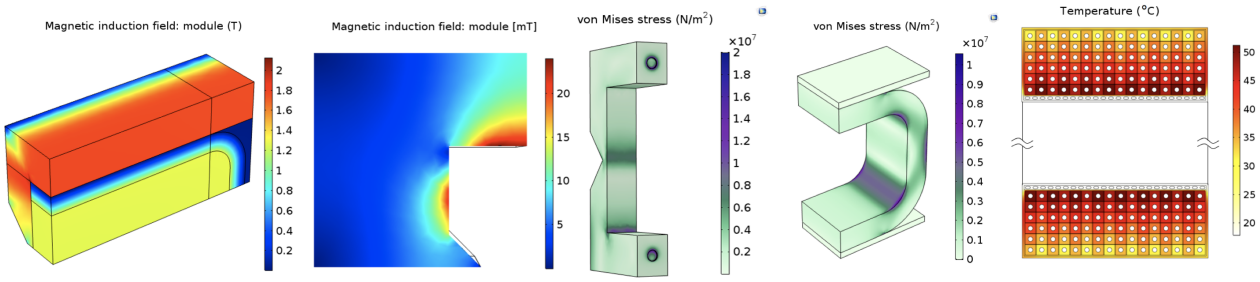

Figure 43: Magnetic field strength in the detector volume, the coil and yoke (a) and in the magnet surroundings (b). Mechanical stresses in a section of one iron yoke block (c) and in the coil edges (d). Temperature in the coil and in the thermal shield (e).

4.2 Emulsion Target

The Emulsion Target is in the current baseline made of 19 emulsion brick walls and 19 Target Tracker planes. The walls are divided in 2×2 cells, each with a transverse size of 40×40 cm^2, containing an Emulsion Cloud Chamber (ECC) and a Compact Emulsion Spectrometer (CES) as illustrated in Figure 44.

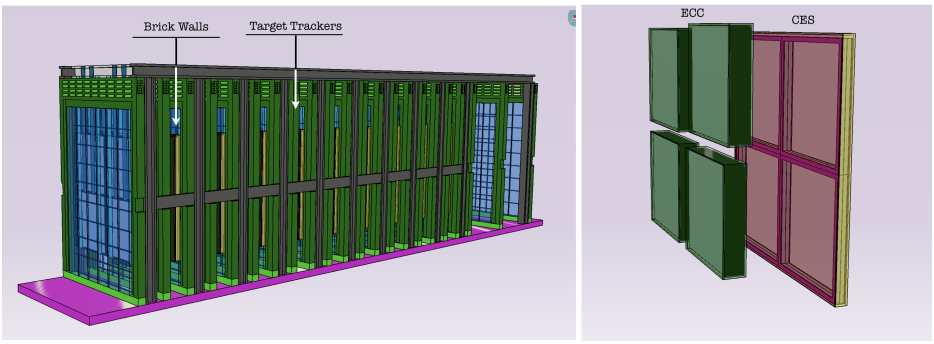

Figure 44: Layout of the Emulsion Target and closeup view of one emulsion brick wall of four cells, each containing an ECC and a CES.

The ECC technology makes use of nuclear emulsion films interleaved with passive absorber layers to build up a tracking device with sub-micrometric position and milliradian angular resolution, as demonstrated by the OPERA experiment [88]. It is capable of detecting τ leptons [89] and charmed hadrons [90] by disentangling their production and decay vertexes. It is also suited for Light Dark Matter detection through the direct observation of the scattering off electrons in the absorber planes. The high spatial resolution of the nuclear emulsion allows measuring the momentum of charged particles through the detection of multiple Coulomb scattering in the passive material [91], and identifying electrons by observing electromagnetic showers in the brick [92]. Nuclear emulsion films are produced by Nagoya University in collaboration with the Fuji Film Company and by the Slavich Company in Russia.

A unit cell is made of 57 emulsion films with a transverse size of $40\times40\,\mathrm{cm}^2$, interleaved with 1 mm thick lead layers. The resulting brick has a total thickness of ∼8 cm, corresponding to $\sim10X_0$, and a total weight of ∼100 kg. The overall target weight with 19 walls of 2×2 bricks is about 8 tonnes. The use of tungsten instead of lead is also being considering, both for its higher density and for its shorter radiation length and smaller Molière radius, which improve the electromagnetic shower containment. With the estimated background flux, the emulsion films must be replaced twice a year in order to keep the integrated amount of tracks to a level that does not spoil the reconstruction performance. The films are analysed by fully automated optical microscopes [93, 94]. The scanning speed, measured in terms of film surface per unit time, was significantly increased in recent years [85–87]. The current scanning speed and the availability of several tens of microscopes within the collaboration makes it possible to scan the whole emulsion film surface over a time scale of six months.

The Compact Emulsion Spectrometer modules aims at measuring the electric charge and the momentum of hadrons produced in τ lepton decays, thus providing the unique feature of disentangling ν_τ and $\overline{\nu}_\tau$ charged current interactions also in their hadronic decay channels. The CES also measures the momentum of soft muons which are emitted at large angles and which do not reach the Muon Tracker. The basic structure of the CES is made of three emulsion films interleaved by two layers of low density material. The emulsion films belonging to the CES will need more frequent replacements than those of the ECCs since reconstruction requires a lower level of background tracks. The replacement frequency is part of the current investigation.

The CES concept was demonstrated in 2008 [95]. A CES prototype using Rohacell as spacer between consecutive films was tested in 2015. The results showed that Rohacell does not respect the

required planarity. A new version with air gaps was designed and tested in 2017 at the CERN PS. The air gap was made by a 15 mm-thick PMMA hollow spacer placed between consecutive emulsion films. The CES chamber was located inside the MNP17 magnet at CERN, providing a vertical 1 T magnetic field, and exposed to π^- beams with momenta ranging from 1 to 10 GeV/c. A picture of the CES during the exposure is shown in Figure 45.

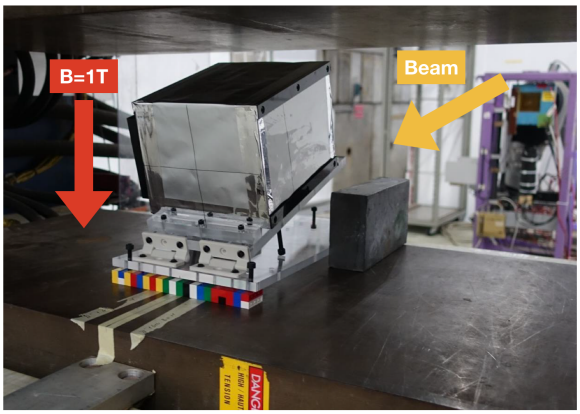

Figure 45: CES chamber exposed to pion beam at the CERN PS.

Different emulsion film prototypes were tested in order to identify the support for the emulsion which minimises local deformations. Results show that the use of a 500 μm-thick glass base induces deformations on the emulsion surface which are five times smaller than the 175 μm thick PMMA base typically used.

The results obtained with the CES made with a glass base are very promising. The distributions of the measured sagitta along the x-axis for 1 and 10 GeV/c pions show gaussian peaks with σ of 10.2 and 1.15 μm, respectively (Figure 46). The measured sagitta values are reported, and compared with the expected values, in Table 3. A very good agreement is observed in the whole momentum range. A momentum resolution of $\sim$30% up to 10 GeV/c momenta was achieved for the first time. The value reported in Table 3 shows that the resolution at low momenta is dominated by the multiple scattering in the 500 micron glass support. However, at those energies, the momentum can be more accurately determined by the multiple Coulomb scattering.

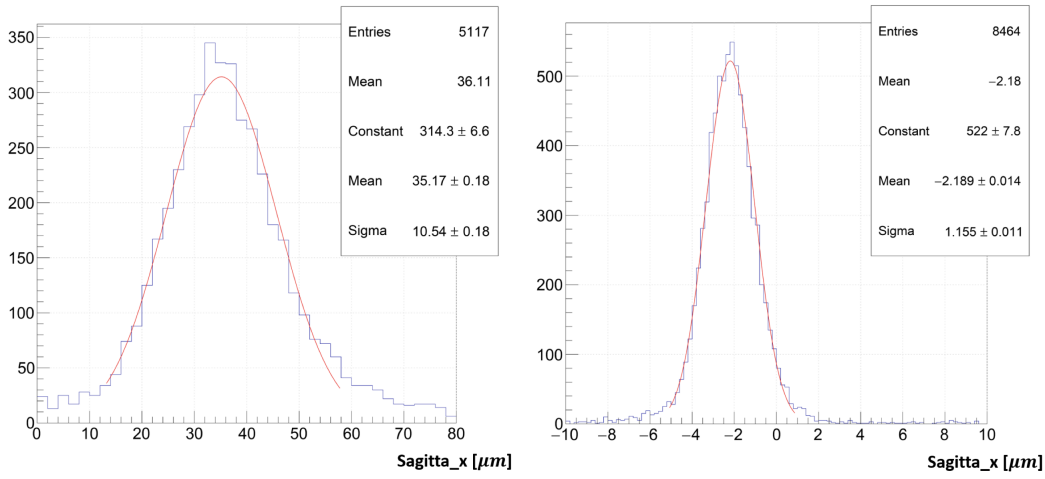

Figure 46: Measured sagitta along the x axis for 1 and 10 GeV/c pions.

P_{exp} [GeV/c]	S_{meas} [μm]	σ [μm]	S_{exp} [GeV/c]	P_{meas} [GeV/c]	$\Delta(1/P)/(1/P)$[%]
1	41.0 $\pm$ 0.2	10.5$\pm$ 0.2	37.1	0.9	29.9
2	20.1 $\pm$ 0.1	4.6 $\pm$ 0.1	17.68	1.8	29.7
4	9.32 $\pm$ 0.04	2.38 $\pm$ 0.05	8.84	3.8	32.2
8	5.46 $\pm$ 0.02	1.23$\pm$ 0.02	4.29	6.3	27.5
10	3.69$\pm$0.02	1.16$\pm$ 0.01	3.43	9.3	35.6

Table 3: Measured sagitta and the corresponding standard deviations compared with expectations. The measured momenta and the accuracy are also reported.

4.3 Target Tracker and Downstream Tracker

A system of electronic detectors in combination with the ECCs is needed in order to time stamp the events reconstructed inside the bricks and to connect the emulsion tracks to those reconstructed in the Downstream Tracker and in the muon identification system.

The Emulsion Target employs 19 Target Tracker (TT) planes in the current baseline configuration, with the first one acting as a veto for charged particles entering the Emulsion Target. Each TT plane has a $80\times120\,\mathrm{cm}^2$ transverse size and complements the corresponding brick wall. The TT system must satisfy the following requirements in order to operate properly with the ECCs in the 1.2 T magnetic field:

- flat surface to guarantee a precise parallel alignment of the ECC brick wall and the TT plane;
- total thickness of a single plane of within 5 cm;
- position resolution better than 100 μm in both x and y coordinates;
- high efficiency (>99%) for particle incident angles with respect to the beam axis up to $\pi/4$
- time resolution of $< 10\,\mathrm{ns}$ for the time stamping.

Three TT planes located downstream of the Emulsion Target measure momentum and charge for long tracks, in particular muons. The distance between two consecutive planes is 50 cm without any material interposed between them.

All the tracker planes are based on the same technology. Two options are currently under evaluation: micro-Resistive WELL (μ-RWELL) and Scintillating Fibre (SciFi) developed in LHCb. As demonstrated below, the two options have comparable performances in terms of position resolution.

4.3.1 μ-RWELL

The μ-RWELL is a novel Micro-Pattern-Gaseous Detector (MPGD) recently proposed [96]. The detector amplification stage, similar to a GEM foil, is obtained with a polyimide structure micro-patterned with a blind-hole matrix, and embedded on a thin Diamond Like Carbon (DLC) resistive layer in the readout Printed Circuit Board (PCB). The introduction of the resistive layer, which strongly suppresses the transition from streamer to spark mode, results in large gains ($> 10^4$), without significantly affecting the capability to stand high particle fluxes. The implementation of the resistive layer also affects the charge spread on the readout electrodes [97], and consequently the spatial resolution of the detector. For tracks orthogonal to the detector, the spatial resolution of a μ-RWELL equipped with 400 μm strip pitch readout, shows a minimum of about 50 μm for a DLC surface resistivity of about 100 M$\Omega/\square$ [98]. For non-orthogonal incident angles, the magnetic field smears and deforms significantly the electron charge shape at the anode, leading to an overall deterioration of the spatial resolution. This effect, common to all MPGDs, can be overcome by exploiting the so-called micro-TPC mode operation. The micro-TPC mode is a recently developed readout approach for MPGDs, first introduced by the ATLAS MicroMegas (MM) community [99]. This method evaluates the position of a track by combining information about the arrival time and the amplitude of the induced signals on the strip.

Since the TT is required to have an overall spatial resolution better than 100 μm, a combined test beam of μ-RWELLs operated in micro-TPC mode and a set of emulsion bricks was performed with muons at the CERN SPS. The experimental setup is shown in Fig. 47. Two μ-RWELL detectors, providing x and y views respectively, were placed on both sides of a rotating support, in order to perform exposures at different track angles. Two emulsion doublets were attached at a distance of 7.6 mm from the μ-RWELL PCB.

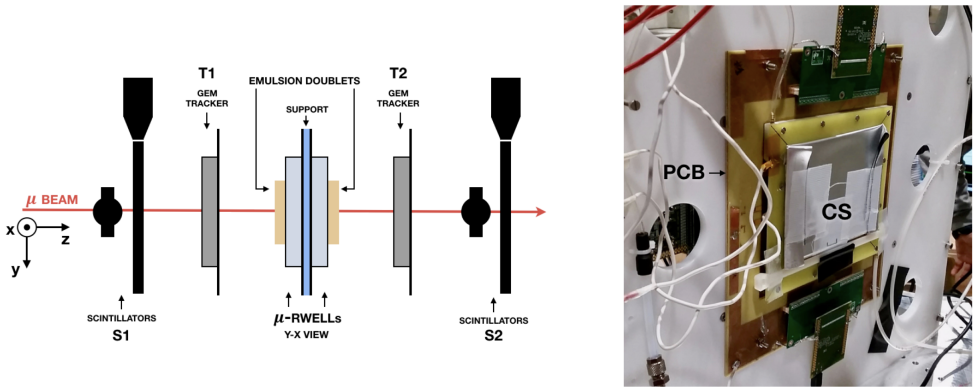

Figure 47: Left: sketch of the experimental setup used for the combined emulsions-μ-RWELL test beam. Right: Replaceable films attached to the μ-RWELL tracking chamber cathode side, at a distance of 7.6 mm from the PCB.

The position reconstructed by the μ-RWELL was determined in both Charge Centroid (CC) and micro-TPC mode.The left plot of Figure 48 shows the spatial resolution as a function of the track incident angle when operating the detectors with a the drift field $E_d = 0.5$ kV/cm. These data do not include the emulsion as external tracker. The black curve shows the results obtained with the CC method. The blue curve shows the spatial resolution in the micro-TPC mode. The red curve is a convolution of both methods. The CC mode gives good results for orthogonal tracks (90°) while the micro-TPC mode shows higher performance for non-orthogonal tracks, as expected. Combining the two methods a spatial resolution better than 100 μm could be achieved. Further improvements can be obtained with a better optimisation of the operating parameters of the detectors and by correcting for alignment errors.

A preliminary study of the matching between the μ-RWELL and the emulsion detector was tested with tracks impinging orthogonally. The μ-RWELL data refer to a parallel mode detector operation with a drift field $E_d = 1$ kV/cm. The residuals in the Y coordinate between the tracks reconstructed with the emulsion and with the μ-RWELL are shown in the right plot of Figure 48. The variance of the gaussian fit amounts to $\sim$40 μm. It is in agreement with the results reported in the left plot. Analysis of exposures at large angles is in progress.

4.3.2 Scintillating Fibre Tracker

The SciFi tracker option [100] is based on a detector technology developed for the LHCb upgrade in the LHC Long Shutdown 2. A mass production facility (several hundred square metres) has been developed and successfully operated in the framework of the LHCb SciFi collaboration. The main advantages of the SciFi tracking detectors are high spatial resolution (30-50 μm depending on its dynamic range) and very high efficiency to minimum ionising particles (>99.6%), totally unaffected by magnetic fields. In addition, the detector, based on thin (250 μm diameter) scintillating fibres, is extremely uniform and has no dead zones. Other advantages include the absence of power dissipation in the active detector planes, two-coordinate readout with a 3 mm thick active detector layer, and low density (0.05 X_0 with composite

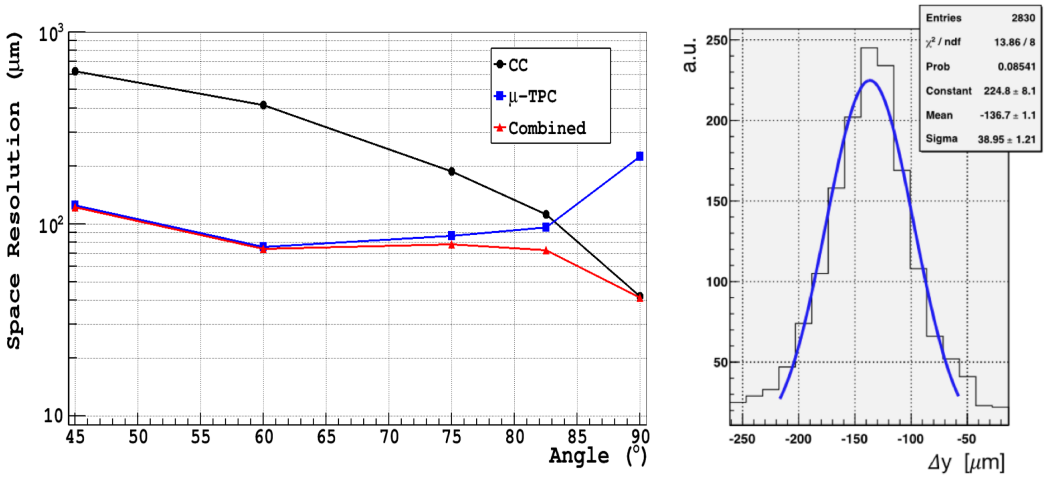

Figure 48: Left: spatial resolution of the μ-RWELL as a function of the incident track angle. Right: distribution of the position residuals along the y axis obtained in combination with emulsion for tracks orthogonal to the surface.

support planes). The cost per square metre is roughly two orders of magnitude less than for a silicon micro-strip detector with comparable resolution.

A TT station based on SciFi consists of two readout X and Y planes (each 1.45 mm thick), made of six scintillating fibre layers packed in an hexagonal continuous structure, and covering the full cross sections of the ECC brick walls. The fibre planes are supported with a Nomex honeycomb and thin (200 μm) CFC skins on the top and the bottom of the sandwich glued together under vacuum. Two sides are used to readout the light directly from the x and y fibres with multi-channel SiPMs such as Hamamatsu S10943-3183X. The other two sides are covered with mirrors (3M ESR foils).

The left panel of Figure 49 shows the spatial resolution measured in the LHCb application [101]. The right panel shows the setup used in a combined test with nuclear emulsion to check the performance and study possible systematic effects. The setup consists of a SciFi prototype with X and Y readout. It was exposed to cosmic rays in Moscow and the data analysis is in progress. An exposure with the electron beam at DESY is planned for 2019. The main purpose of this test is to check to what extent the SciFi can complement the ECCs in the measurement of electromagnetic showers in an environment where a few hundred showers will be contained in about $1000\,\mathrm{cm}^3$.

Eight SciFi planes with a $390.9\times400\,\mathrm{mm}^2$ surface were also constructed and operated in the SHiP-charm measurement in July 2018. The detector planes were installed to provide XY and UV stereo readout (at $\pm2^\circ$) combined in two stations. The data are under analysis.

4.4 Muon identification system

The muon identification system is designed to identify with high efficiency the muons produced in neutrino interactions and in τ decays occurring in the Emulsion Target. In the current design, the system consists of 13 iron filters, 10 cm thick, interleaved with 12 tracking planes instrumented with RPCs. The transverse dimensions of the active planes are $\sim2\times5\,\mathrm{m}^2$. The last two planes cover the whole decay vessel entrance window in order to tag neutrino interactions in the muon system which may give rise to potential background events in the downstream Hidden Sector Decay Spectrometer. Studies are ongoing to optimise the number of planes as well as the thickness of the iron filters for the identification of low energy muons, and measurement of their momenta through their penetration power, as a consistency check with the upstream detectors. A schematic view of the current design is shown in Figure 50.

Due to the relatively high rate of beam-induced muons, the RPCs will be operated in avalanche

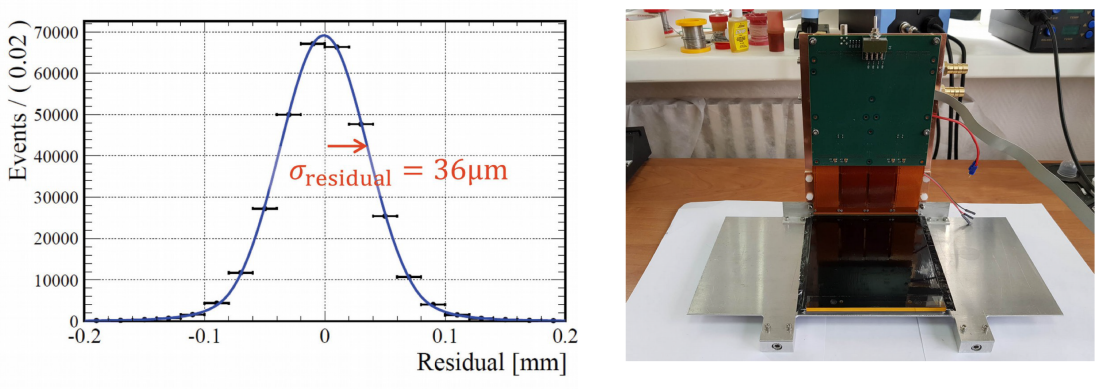

(a) (b)

Figure 49: SciFi position accuracy, as measured by LHCb, and setup used in a combined test beam with emulsion.

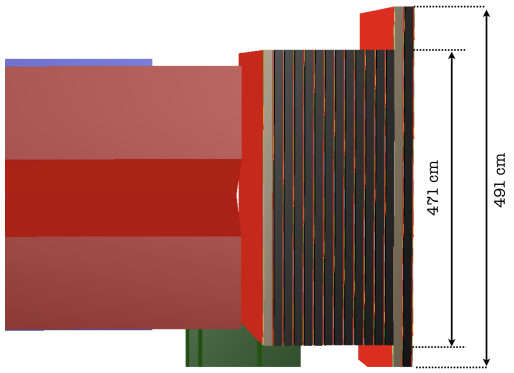

Figure 50: Schematic view of the design of the muon identification system.

mode. Each RPC plane will be made of four gas gaps, and with transverse dimensions of $\sim 2 \times 1.25\,\mathrm{m}^2$ each. The planes are arranged to cover the active area as shown in the left panel of Figure 51. The RPC planes will be read out by means of orthogonal strip panels with a pitch of 1-2 cm, subject to further optimisation.

A pilot production of five RPC detectors (size $2 \times 1.25\,\mathrm{m}^2$) was successfully made for the muon flux and charm production measurements in 2018 at the CERN H4 beam line. They are shown in the right panel of Figure 51. Gaps with 2 mm thick electrodes made of High Pressure Plastic Laminate (HPL, commonly known as bakelite) have been produced at the Korea Detector Laboratory (KODEL) in Korea. The HPL has a volume resistivity in the range $6-9 \times 10^{10}$ Ωcm. The outer surfaces of the electrodes were coated with conductive graphite paint and insulated with a PET film glued on them. Each gap was readout by two panels of X/Y strips with 1 cm pitch. The strip panels were also produced at KODEL. The chambers were operated in avalanche mode using the standard CMS/ATLAS gas mixture, 95.2% C2H2F4/ 4.5% Iso-C4H10 / 0.3% SF6 with a flux of about 2 l/h at HV = 9.6 kV.

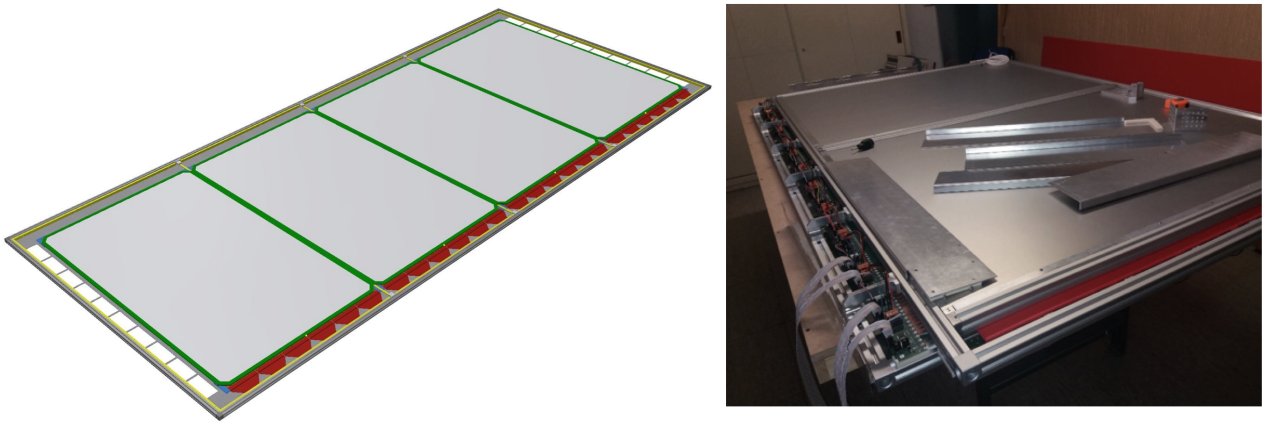

(a) (b)

Figure 51: Left: schematic drawing of an RPC plane made of four gas gaps. Right: RPC mechanical structure during the pre-assembly for the muon flux and charm measurements. The FE boards connected to the vertical strips are visible on the long edge of the structure.

5 Decay Spectrometer

The SHiP Decay Spectrometer consists of the large vacuum vessel, the Surrounding Background Tagger (SBT), the Spectrometer Straw Tracker (SST), together with the large spectrometer magnet with a total field integral of about 0.5 Tm, the Timing Detector (TD), the Electromagnetic Calorimeter and the downstream Muon system.

The Decay Spectrometer has to perform precise measurements of charged particles and photons originating from decay vertices of hidden particles in the decay volume, measure their momenta, and provide PID information. Moreover, the Decay Spectrometer has to ensure a redundant background suppression using timing and track information from the TD and the SST, vetoing criteria from the upstream muon system of the SND and the SBT, and PID by the calorimeter and the muon systems.

This section describes the principal features and main parameters of the Decay Spectrometer subdetectors as implemented in FairShip. These parameters have been used in the simulation studies of the Decay Spectrometer performance reported in Section 6. Specific proof-of-principle tests of prototypes have been undertaken in order to demonstrate that the expected detector performance can be achieved.

5.1 Surrounding Background Tagger

The SBT detects charged particles either entering the vacuum vessel from outside, or produced in the inelastic interactions of muons and neutrinos in the vacuum vessel walls. The baseline option for the SBT (LS-SBT) is using a liquid scintillator consisting of linear alkylbenzene (LAB) together with 2.0 g/l diphenyl-oxazole (PPO) as the fluorescent. This technology provides large detection efficiency and good sensitivity at a reasonable cost.

The LS-SBT is sub-divided into individual cells integrated into the support structure of the vacuum vessel. Accordingly, the cell size is 80 cm in the longitudinal direction and typically $\sim$120 cm in the transverse direction, depending on the location along the vacuum vessel. The thickness of the LS layer, surrounding the walls of the complete decay volume is $\sim$30 cm, again varying along the length of the vacuum vessel. Due to the conical shape of the decay vessel, the current LS volume of $\sim$243 m^3 is significantly reduced compared to the TP. This allowed increasing the PPO concentration from 1.5 g/l quoted in the TP without any increase in price for the LS. Each cell of the LS-SBT is readout by

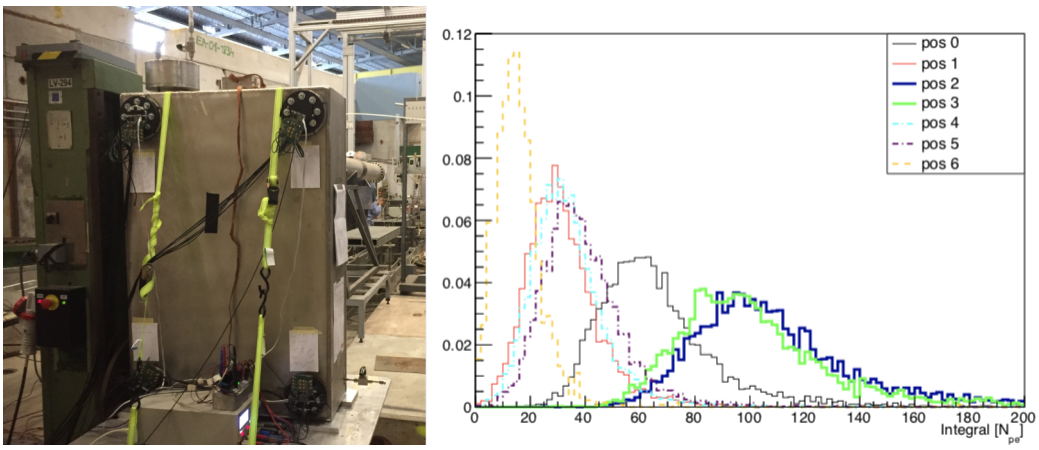

Figure 52: Left: prototype of a WOM MODULE, tested at the CERN PS T10 test beam area. Right: number of photoelectrons detected by the WOM module for muons at different beam positions.

two wavelength-shifting optical modules (WOM) that detect scintillation light in the range of 340 nm – 400 nm and transport the light to a ring of 24 SiPMs of $3 \times 3\,mm^2$ area directly coupled to the WOM tube. There are O(3500) WOMs for the whole LS-SBT. Beam test measurements in 2017, using a cell with a volume of $50 \times 50 \times 30\,cm^2$ (and 1.5 g/l PPO), show that a detection efficiency for muons of

at least 99.6% has been achieved. The WOM, equipped with a light guide and viewed by an array of eight $6 \times 6\,\mathrm{mm}^2$ SiPMs, as shown in Figure 52 (left), was required to detect at least five photoelectrons. The average number of photoelectrons detected by this WOM depends on the position of the particle traversing the LS cell and was measured to be at least 30 (see Figure 52 (right)). The measurements also demonstrate that a time resolution of 1 ns can be achieved with the threshold for both WOMs set to two photoelectrons. Since a fully satisfactory performance has been demonstrated with the WOM-based LS-SBT, the option with large-area PMTs is currently not pursued further.

Several ways of increasing the detected light yield and hence the efficiency have been identified. This includes increasing the PPO concentration and direct coupling of the SiPMs to the WOM tube without using a light guide. These improvements can also improve the time resolution thanks to the higher photoelectron statistics. A new design, with a larger cell size of $120 \times 80 \times 30\,\mathrm{cm}^3$, was tested with beam at CERN in October 2018, including a test of all the basic steps of the filling strategy for a small-scale liquid scintillator handling system.

While the basic components of the LS mixture have been identified (solvent LAB, fluor PPO), the exact composition still has to be optimised to the dimensions of the SBT cells. This concerns the concentration of PPO and a possible addition of paraffin oil to increase the transparency for a given scintillation light yield. Reflective coating, covering the inner walls of the cells, has to be selected based on the chemical compatibility and spectral reflectivity. Moreover, vitamin E will be tested as an additive to improve the chemical durability of the LS against accidental exposures to atmospheric oxygen. Finally, the use of green-sensitive SiPMs would allow using a green dye in the WOM coatings and an additional wavelength shifter (bisMSB) to the scintillator, improving its transparency and thus the homogeneity of the light response.

The cell geometry and the LS-SBT detector response are implemented in FairShip, providing the energy deposit from charged particles inside each individual cell. In the data analysis, a minimum energy deposition of typically $45\,\mathrm{MeV}$ is required to consider a LS cell as fired. This threshold is slightly below the energy deposition of a MIP traversing a LS cell perpendicular to the vacuum vessel wall. The timing performance of the LS-SBT, measured in test beam, has not yet been implemented in the simulation of the LS-SBT response.

The information from the LS-SBT is used in the background suppression of DIS events in the decay-vessel walls, induced either by neutrinos or muons, assuming that the detection probability inside a LS cell for charged particles depositing at least 45 MeV is 99.9%. The test beam results are already very close to this value.

5.2 Spectrometer Straw Tracker

The purpose of the Spectrometer Straw Tracker (SST) is to measure track parameters and momentum of charged particles with high efficiency and accurate enough to reconstruct decays of hidden particles, and to reject background events. The precision of the extrapolated position of the tracks must be well matched with the segmentation of the timing detectors (see Section 5.3) such that the high accuracy of the associated track time can be used to remove combinatorial background. The invariant mass, the vertex quality, the timing, the matching to background veto taggers, and the pointing to the production target are crucial tools for rejecting background.

The spectrometer consists of a large aperture dipole magnet and two tracking telescopes, one on each side of the magnet and each composed of two tracking stations. The four stations are identical with a nominal acceptance of 5 m in X and 10 m in Y, and are based on ultra-thin straw drift tubes oriented horizontally. Each station contains four views, in a Y-U-V-Y arrangement, where U and V are stereo views with straws rotated by a small angle $\pm\theta_{\mathrm{stereo}}$ around the z-axis with respect to the y-measuring straws.

The main change since the TP is the increase of the straw diameter D from 10 mm to 20 mm. This

change is motivated by the refined background rate simulations which confirm that for $D = 20\,\text{mm}$ the rate per straw remains modest ($< 7\,\text{kHz}$ in the hottest straw).

Tools for producing 20 mm straws have been developed and several prototype straws, using as before a 36 μm thick PET film coated with 50 nm Cu and 20 nm Au, have been produced with no new difficulty encountered compared to the fabrication of the original 10 mm straws. Several straws of 20 mm diameter and 5 m length have been fabricated. The rupture over-pressure was measured on ten samples of 50 cm length and was found to be around 4.4 bar, as expected. This is considered a sufficient margin for operating the straws at a pressure of about 1 bar in vacuum. The torsion of 5 m long straws, cemented on one side and pressurised to 1 bar over-pressure, was measured. A rotation of 38° was found at the free end. A torque of about $0.076\,\text{N m}$ was needed to cancel the rotation. A 2 m long $D = 20\,\text{mm}$ straw was fabricated and its performance as a MIP detector was characterised in a test run with beam in the SPS north area as a function of the wire offset at nominal conditions (~ 1.05 bar pressure, 70% Ar / 30% CO_2). The beam test set-up is shown in Figure 53. First results indicate that a straw hit resolution of 120 μm is achievable with high hit efficiency over most of the straw diameter, independently of the wire offset, as shown in Figure 54. The drift time spectra for different wire offsets are being analysed, and

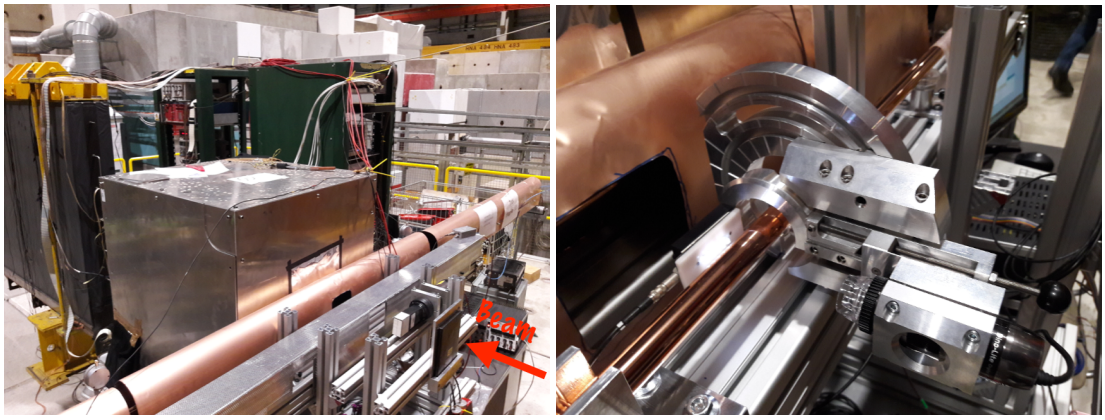

Figure 53: Left: picture of test beam setup. Right: zoom on straw while wire offset is measured with digital camera.

methods to extract the local wire offset from the distinctive features of the spectra are being investigated. Alignment studies for the full detector, using MC simulation, are being started, which should allow us to define the geometrical constraints for the mechanical engineering design.

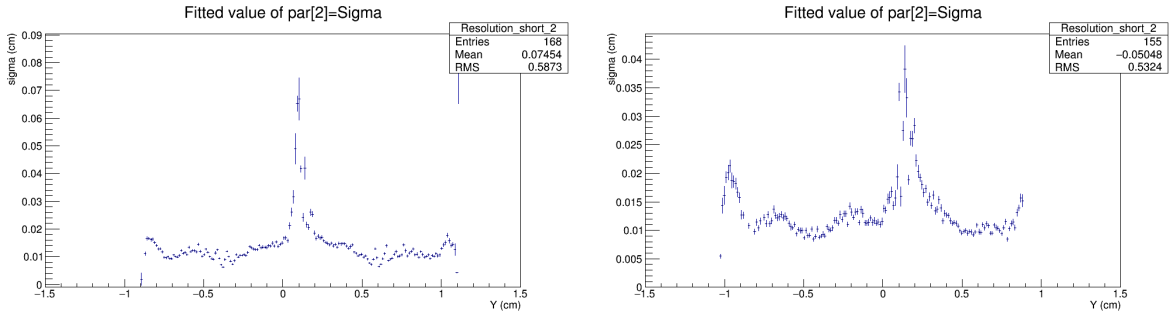

Figure 54: Hit resolution across the straw diameter for $D = 20\,\text{mm}$. Left: no wire offset. right: wire offset of $\sim 2\,\text{mm}$.

FairShip has been updated with the changes of the SST, and further optimisation studies are under way. The new straw layout, taking into account the larger straw diameter (20 mm), was obtained from geometrical considerations aiming at a high hit detection efficiency. As shown in Section 6, the

performance of the SST is not degraded in comparison to the TP. Dummy mechanical frames (stainless steel) were added around the straw panels to provide a more realistic material environment, and it was checked that background rates remain acceptable. A new field map, extracted from an FEA calculation, was implemented in the MC simulation, including the return field in the yoke. The return field has an effect on the rates in the last two stations, though these remain acceptable. An optimisation of the station geometry and, in particular, of the stereo angle is ongoing. Realistic simulation of the straw signal depending on the hit position is under development. A parametrization of the drift time distributions from GARFIELD simulations [102] is obtained as a function of the track local coordinates for ideal and non-zero wire offset. It was found to be in a reasonable agreement with the results from beam test measurements. Parametrized dependencies of the most probable signal arrival time, and the corresponding time resolution, are being prepared for a later version of FairShip.

The engineering challenges associated with the mechanical properties of the strongly strained long straws and tungsten wires were considered. Elongation and relaxation effects, which if neglected would result in excessive and evolving sagging of the straws, must be taken into account *ab inito* in the design. Several schemes are being studied, one of which includes a long-stroke constant-force spring, capable of maintaining the wire under the desired tension while accommodating a straw elongation of several centimeters. Another scheme utilises a straw suspension mechanism based on carbon fibres. A radically different method, developed for the COSY-TOF detector and the PANDA straw tube tracker [103], is now also being explored. In this technique, ultra-thin straws are held together by sparse glue dots in a close-packing configuration and "inflated" to 1 bar over-pressure. A self-supporting, rigid and straight straw tube module can be obtained without externally straining the straws and without straw suspension mechanism.

A preliminary conceptual design of the vacuum enclosure is being worked out which foresees a vacuum chamber with rectangular cross section, longitudinally extending over the whole spectrometer length, and providing four rectangular openings on the top side. These openings are used to insert the tracker station frames, fully equipped, into the vacuum volume. In this concept, the vacuum enclosure is decoupled from the mechanical structures of the detector. Front-end electronics are located inside the vacuum and require active cooling.

5.3 Timing detector

The TP baseline configuration for the plastic scintillator-based option of the SHiP timing detector (TD) consisted of two columns of 305 cm long bars instrumented with PMTs. Although the viability of using large-area SiPMs for the light readout was not known at the time, this scheme was discussed as an attractive solution which needed R&D. It has now been demonstrated that the large-area SiPM scheme is not only viable, but actually offers a better performance at a lower cost. A three-column setup of bars read out by arrays of large-area SiPMs is now chosen as the baseline option. The current design features bars made of EJ-200 plastic scintillator with dimensions 168 cm$\times$6 cm$\times$1 cm, arranged in three columns and 182 rows with 0.5 cm overlap between bars, for a total area of 5 m$\times$10 m. Each bar is read out on both sides by an array of eight 6 mm$\times$6 mm SiPMs. The signals from the eight SiPMs are summed by an ASIC based on the MUSIC chip [105] to form a single channel. Thus there are a total of 564 bars and 1128 channels.

Figure 55 presents the results obtained with a 1.5 m long bar read out by two arrays of 8 SiPMs attached to both ends of the bar, as detailed in Reference [104]. The resolution of the mean time is demonstrated to be $\sim$80 ps along the whole length of the bar.

In summer 2018, a 22-bar (44 channels) prototype array with 1.68 m long bars (same dimensions as those of the current SHiP design) was successfully operated at the CERN PS test beam, providing time-of-flight information to a high-pressure TPC prototype, as shown in Figure 56 (left). The front-end electronic boards based on the MUSIC chip to read out the SiPMs and provide the summed output, are

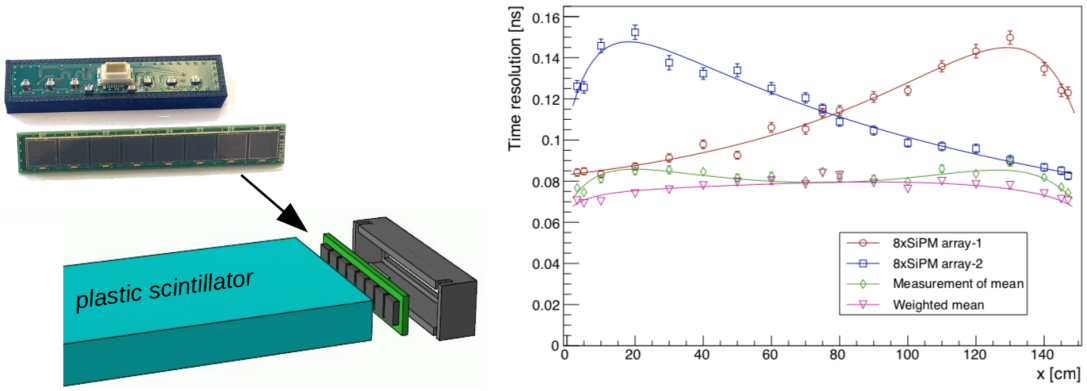

Figure 55: Left: picture of an array of eight 6 mm×6 mm SiPMs integrated into a PCB with a parallel connection and applied directly to the bar surface. Right: time resolution as measured by the SiPM arrays at both ends of a 1.5 m bar as a function of the beam impact position along the bar [104].

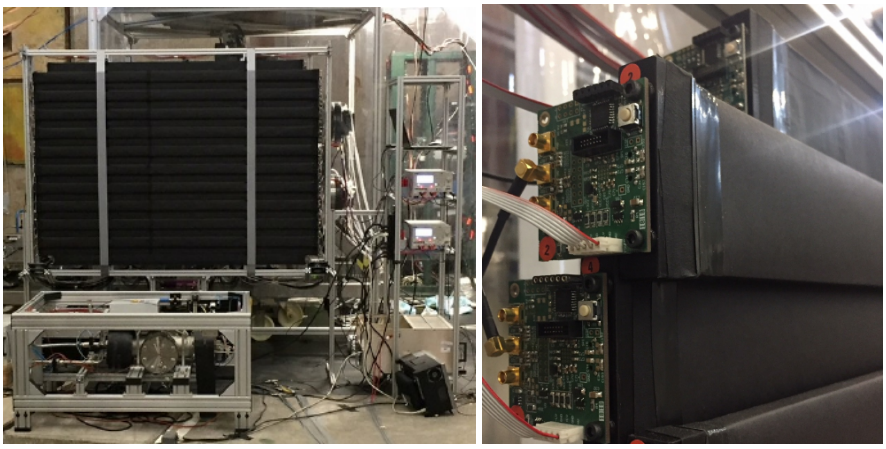

Figure 56: Left: picture of the plastic scintillator TD prototype comprising 22 bars, placed in front of a high-pressure TPC prototype and exposed to test beams at the CERN PS. Right: picture showing some of the front-end electronic boards of the TD prototype, providing a summed output signal for arrays of 8 large-are SiPMs applied to the bar surface.

shown if Figure 56 (right). The prototype showed similar performance as the single bar over its whole 2.1 m^2 active area.

An alternative option for the timing detector is based on the timing Resistive Plate Chamber (tRPC) technology. It uses a novel concept for the construction of the RPC gaps to address the problem of gas tightness and the high voltage insulation. The sensitive module is confined inside a completely sealed plastic box. This eases the construction and allows operation with a low flux of gas. The sensitive module of the SHiP tRPC incorporates a multi-gap RPC structure with six gas gaps defined by seven 1 mm thick float glass electrodes of about $1550 \times 1250\,\mathrm{mm}^2$, separated by 0.3 mm nylon mono-filaments. The tRPC chamber is composed of a sandwich of two identical sensitive modules with a plane of pick-up electrodes, consisting of $1600 \times 30\,\mathrm{mm}^2$ copper strips, in the middle. Both ends of each copper strip is directly connected to a low-jitter high-gain/bandwidth Front-End Electronics (FEE) read out by an FPGA-based multi-hit TDC. The time of a hit is derived from the average of the times registered on each end of the strips.

A tRPC prototype has been exposed to 8 GeV pions in October 2018 at the CERN T9 test beam area, as shown in Figure 57a. The almost $2\,\mathrm{m}^2$ active area has been scanned in order to obtain the

efficiency and timing performance at different locations. The results, summarised in Figure 57b, demonstrate an efficiency of 98% and an average time resolution of 54 ps.

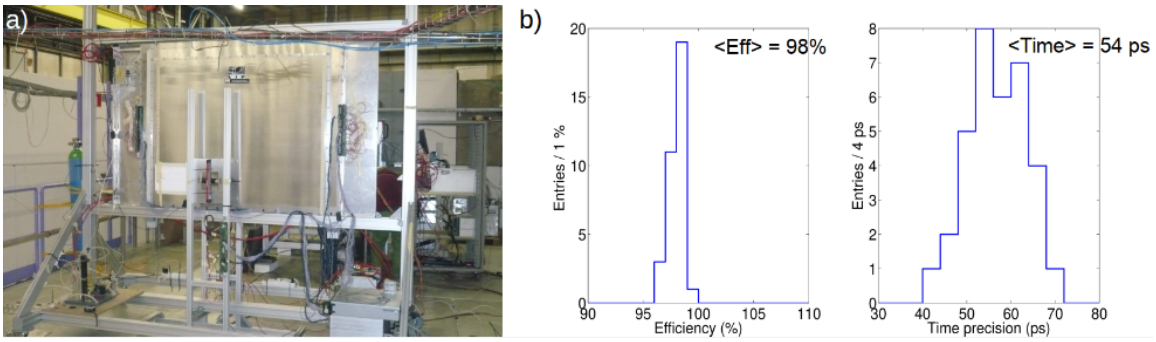

Figure 57: a) Test beam setup with the $2\,\mathrm{m}^2$ active area tRPC prototype. b) Preliminary results on the detector performance, demonstrating an average efficiency of 98% and a time resolution of 54 ps.

5.4 Electromagnetic Calorimeter

Compared to the TP, the design of the calorimeter system, based on the shashlik technology, has been changed to the longitudinally segmented SplitCal design which can measure the trajectory of photons originated from the $ALP \to \gamma\gamma$ decays, and improve electron/hadron separation.

SplitCal is a $25X_0$ long lead sampling calorimeter, with lead absorber plates orthogonal to the proton beam direction, and with two kinds of active layers. Most sampling layers are equipped with scintillator bars read-out by WLS fibres with a relatively coarse spatial segmentation. The lead absorber plates are $0.5\,X_0$ thick, i.e. 0.28 cm, while the scintillator is 0.56 cm thick. The positions of the three high resolution active layers, each 1.12 cm thick, are optimised to provide the best possible angular resolution for low and high energy photons. The first layer, located at $3\,X_0$ depth, together with the other two, located at the shower maximum, measure the photon angle by reconstructing the transverse shower barycentre at the three depths. High spatial segmentation of $\sim$200 μm, which could be achieved with e.g. micro-pattern or scintillating fibres detectors, is sufficient to provide a few mrad angular resolution. The photon angular resolution of SplitCal in SHiP is by far the dominant factor in the ALP mass resolution.

The SplitCal design has been implemented in FairShip, and the study of its performance is ongoing. Meanwhile, preliminary results from a dedicated toy Monte Carlo study report an angular resolution of as good as 3 mrad for 20 GeV, 5 mrad for 10 GeV and 9 mrad for 6 GeV photons. This is significantly better than the angular resolution demonstrated with the ATLAS electromagnetic calorimeter.

An outstanding issue in achieving this angular resolution, along with high efficiency for the photon reconstruction, is the presence of shower satellites due to long tails in the transverse shower shape (shown in Figure 58) which makes position reconstruction quite challenging. The shape of the transverse shower profile deposited by electrons in a prototype of the SplitCal module has been measured at a beam test at CERN in October 2018, in order to tune the FairShip simulation. A two-dimensional pattern recognition algorithm will be developed to maximise the sensitivity in the search for $ALP \to \gamma\gamma$ decays.

5.5 Muon system

The muon system has to identify muons with high efficiency ($> 95\%$) in the momentum range of $\sim 5 - 100\,\mathrm{GeV}/c$. Moreover, the muon system can contribute to the rejection of combinatorial background by requiring a tight ($<$1 ns) time coincidence of candidate muon tracks.

The muon detector is located downstream of the electromagnetic calorimeter and is comprised of four stations of active layers interleaved by the three muon filters. The four stations are 6 m wide and 12 m high. The amount of material of the calorimeter corresponds to $6.7\,\lambda_I$. The muon filters are 60 cm

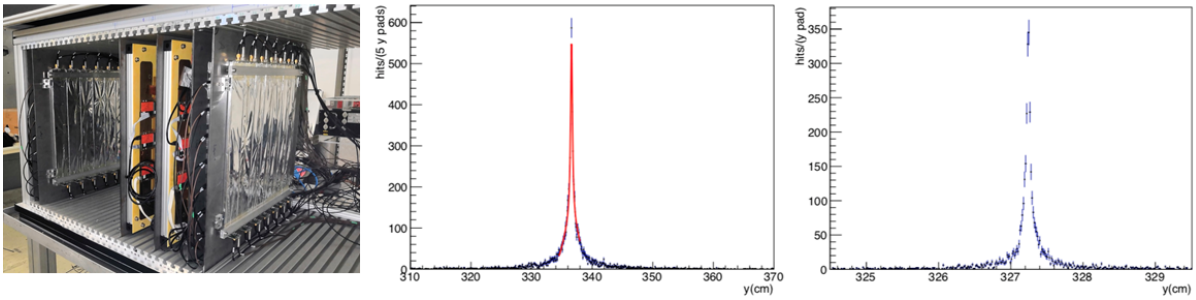

Figure 58: (Left) SplitCal test beam setup with 2×2 scintillator planes and two MicroMegas as high-precision layers (no absorbers in picture). Figure shows transverse shower shape, i.e. number of hit pads vs position in the y-direction, at the first (middle) and the third (right) precision layer of the SplitCal for 20 GeV photons.

thick iron walls, corresponding to $3.4\,\lambda_I$ each. A muon with normal incidence must have an energy of at least of 2.6 GeV to reach the first muon station and at least 5.3 GeV to reach the last muon station. The multiple scattering of muons in the material of the calorimeter and the muon filters drives the granularity of the system. Simulation studies show that a readout granularity of $\sim$10 cm in the transverse directions is adequate for the momentum range of interest.

The rate seen by the muon detector is between 1-6 MHz, depending on the station, mostly caused by the beam-induced muon background. Simulation studies show that the rate is dominated by very low p ($<$100 MeV/c) electrons, positrons and photons produced by inelastic and electromagnetic interactions of muons with the material of the detector. Most of the hits are concentrated in the first muon station. The second and third stations see very low rates while the fourth station sees an almost uniform illumination originating from very low momentum particles surrounding the system. To shield the last muon station against hits arising from muon interactions with the surrounding material, including the cavern walls, a thin ($\sim$10 cm) layer of iron has been added downstream of the last station. The hit rate from real muons is subdominant and does not exceed $\sim$300 kHz, being concentrated on the sides of stations.

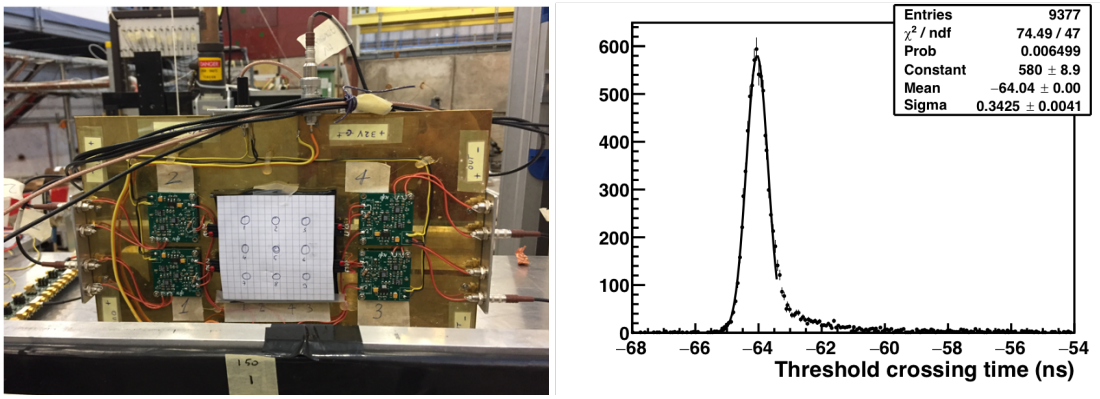

Figure 59: Left: Prototype of a tile for the muon system, tested at the T10 area at the CERN PS. Right: Time resolution.

The detectors of the muon system will cover a surface of $\sim$ 288 m^2 divided in four stations. The baseline technology chosen for the active layers in the TP [3] was based on extruded plastic scintillator bars with wavelength-shifter (WLS) fibres and silicon photo-multiplier (SiPMs) readout. A thorough R&D has been carried out on this technology and the results have been summarised in Reference [106]: a time resolution of $\sim$800 ps has been measured on 3 m long bars, completely dominated by the jitter of the fibre scintillation time. The highly non-uniform and relatively large hit rate, and the need for sub-ns time resolution for reducing the combinatorial background led us to consider a different technology for

the muon system: scintillating tiles with direct SiPM readout. This option is more robust against hit rate variations and has several advantages, including an intrinsically better time resolution and easier mechanical construction.

An excellent time resolution of $\sim$ 340 ps has been measured on small tile prototypes, as shown in Figure 59. Assuming this result can be extrapolated to a large scale detector, a muon system made of four stations equipped with scintillating tiles can in principle reach $\sim$ 200 ps time resolution. A new beam test has been performed in October 2018 to further progress on this R&D. Scintillating tiles with

Number of active stations	4
Active stations dimensions	$(600 \times 1200 \times 1)\,\mathrm{cm}^3$
Tile dimensions	$(10 \times 20 \times 1)$,cm^3
Number of tiles	3 600 $\times$ 4 = 14 400
Weight of the scintillator	11.52 tonnes
FEE channels	14 400
Number of passive iron filters	3
Filters dimensions	$(600 \times 1200 \times 60)\,\mathrm{cm}^3$
Iron weight	$\sim$1000 tonnes

Table 4: Muon System layout as implemented in FairShip.

direct SiPM readout is now the baseline solution for the SHiP Muon system. The basic parameters of the system are summarised in Table 4 assuming a preliminary tile dimension of $10 \times 20 \times 1\,\mathrm{cm}^3$. The tiles geometry has been implemented in FairShip at the digitization level. The tiles are simulated side-by-side without dead spaces.The choice of having the tiles at the digitization level and not hard-coded in the GEANT geometry is driven by the need of having a very flexible geometry to be able to follow the upcoming beam test results and the evolution of the mechanical drawings of the system without rerunning the (computationally heavy) GEANT simulation. Given the excellent time resolution, the possibility of building the muon system with only three stations instead of four is currently being considered. The final decision will be taken for the TDR.

6 Physics performance

The physics performance of the SHiP experiment is anchored in the emphasis on an extremely efficient and redundant background suppression, and a detector which is sensitive to as many decay modes as possible to ensure a model independent search for hidden particles. A set of common benchmark models is used below to illustrate the physics performance to Hidden Sector particle decays and to Light Dark Matter. The last section reports on the neutrino physics performance.

6.1 Hidden Sector particle decays

All benchmark HS models predict a signature with an isolated vertex in the HS spectrometer. Hence, HS signal candidates are required to form an isolated vertex in the fiducial volume. Table 5 summarizes the selection criteria used to estimate the signal sensitivity for the HS benchmark models. For fully reconstructed signal decays, where all particles coming from the decaying hidden particle are reconstructed in the spectrometer, it is required that the impact parameter (IP) to the target is less than 10 cm. This selection cut is very powerful in rejecting all background sources. Partially reconstructed final states (with one or more missing particles, e.g. $N \to \mu^+\mu^-\nu$) point back more loosely to the target. These final states are therefore more challenging to discriminate from the background. The signal candidates are required to have IP < 250 cm and, in addition, no associated activity in the SBT.

Cut	Value
Track momentum	$> 1.0\,\mathrm{GeV}/c$
Dimuon distance of closest approach	< 1 cm
Dimuon vertex position	(> 5 cm from inner wall)
IP w.r.t. target (fully reconstructed)	< 10 cm
IP w.r.t. target (partially reconstructed)	< 250 cm

Table 5: Selection criteria used for the background rejection and the sensitivity estimate in the analysis of Hidden Sector particle decays.

The background to the searches for hidden particles includes three main classes: neutrino and muon induced backgrounds resulting from inelastic interactions in the material of the detector and the cavern walls, and combinatorial muon background resulting from residual muons reconstructed as charged tracks in the SHiP decay spectrometer. As it was demonstrated in the SHiP Technical Proposal, backgrounds originating from cosmic muons can be reduced to a negligible level.

Large samples of neutrino and muon inelastic backgrounds, corresponding to about ten years and five years of SHiP nominal operation, respectively, have been generated using FairShip, forcing all produced neutrinos and muons to interact with the material. The interaction points were distributed along the neutrino and muon trajectories, with weights according to the material density along the tracks.

While the background rejection and signal sensitivities presented here rely on linear cuts, multivariate techniques can be expected to further improve the performance of the final experiment.

6.1.1 HS background rejection

Neutrino induced background

The dominant source of background comes from neutrino inelastic scattering, producing long-lived neutral SM particles which decay to final states similar to HS particles inside the decay volume. The flux of neutrinos emerging out of the target is expected to be $\sim 2 \times 10^{18}$ neutrinos per 2×10^{20} proton on target, which will induce $\sim 3.5 \times 10^7$ neutrino interactions in the vicinity of the decay volume. In order to reduce the number of neutrino interactions inside the vessel, a very conservative vacuum level of 10^{-6} bar was considered for the Technical proposal, resulting in an expectation of less than one neutrino interaction in the air per 2×10^{20} protons on target [3]. Accounting for the additional rejection power

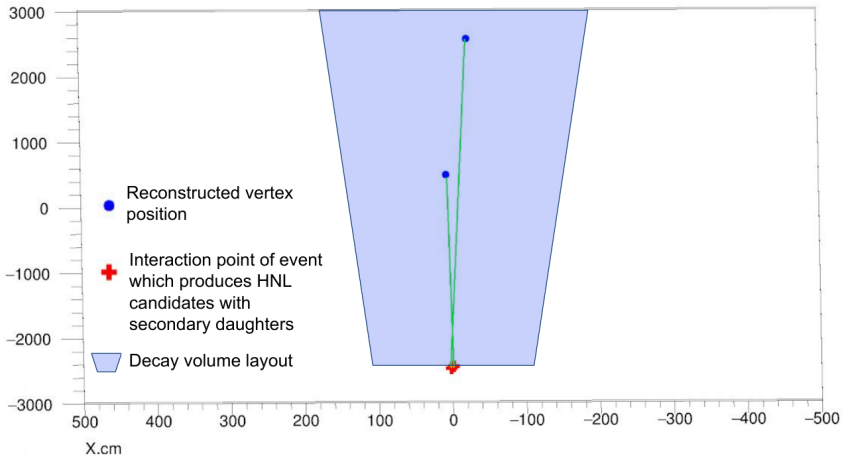

Figure 60: Position of the two events that produce neutrino induced background candidates in the partially reconstructed signal selection.

from kinematics, particle identification, and the veto detectors, it has been possible to reduce the expected background to less than 10^{-2} per 2×10^{20} protons on target with the vacuum pressure increased to $\sim$1 mbar.

The background from neutrino interactions in the walls and in the floor of the surrounding experimental has also been found to be negligible.

The dominant source of neutrino induced background comes from neutrino interactions in the upstream muon detector of the SND and in the walls of the decay volume. The expected number of background events with at least two reconstructed tracks of opposite charge amounts to $\sim 6.5 \times 10^4$ events per 2×10^{20} protons on target. A large fraction of this background is characterised by high particle multiplicities at the origin of the neutral particle. The events can therefore be vetoed by activity in the veto detectors at a location which is compatible with an extrapolation from the reconstructed decay vertex.

Selection criteria	Fully reconstructed	Partially reconstructed	Signal efficiency
Use of veto systems	0	0	64.8%
No veto systems	0	18	65.1%
Veto systems only around the vertex	0	2	

Table 6: Neutrino background in 2×10^{20} protons on target. "Veto systems" refer to the SBT and the upstream muon identification system of the SND.

Applying the selection in Table 5 for fully reconstructed signal event, reduces the neutrino induced background to zero, even without the veto requirement. Applying the selection criteria for partially reconstructed final states and the veto criteria in the SBT, two events remain, both of which originate from photon conversions in the entrance of the decay volume. These type of events are rejected by an additional requirement on the decay opening angle. The location of these events is shown in Figure 60.

Muon inelastic background

The muon deep inelastic scattering (DIS) background comes from muons interacting in the cavern walls and floor, downstream of the muon shield, and with the material of the vessel and the SND detector. The

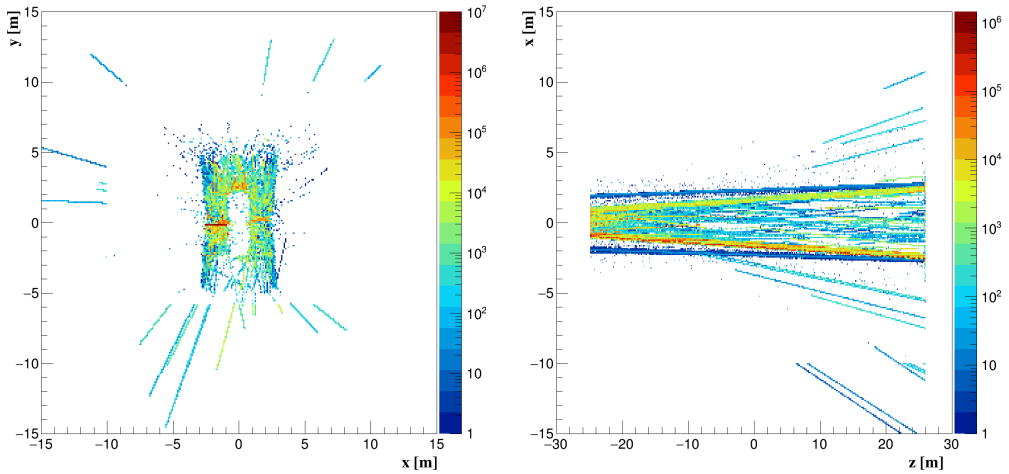

Figure 61: The interaction points of all generated muon deep inelastic scattering events before any cuts are applied.

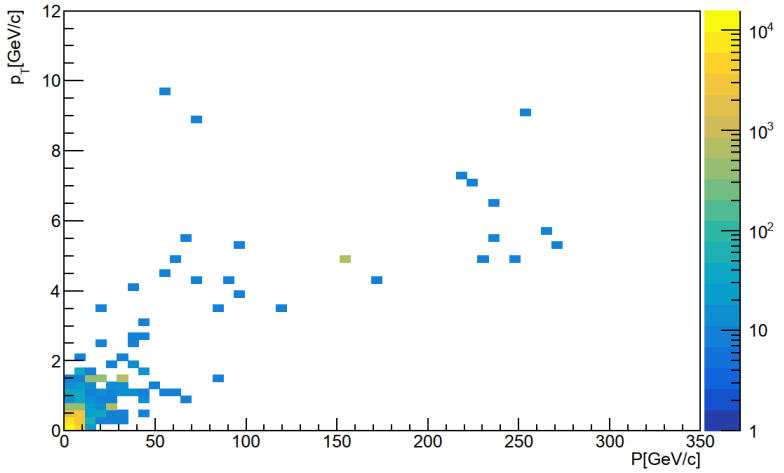

Figure 62: Momentum versus transverse momentum of muons hitting the decay vessel. A 3 GeV/c momentum cut is applied.

latter is expected to dominate, as shown in Figure 61, as the bulk of the muons flux hit the cavern walls downstream of the decay volume.

The number of muons impinging on the decay volume has been estimated to 5.8×10^4 per proton spill, with an average momentum of $\sim$8 GeV/c (see Figure 62), resulting in $2.1 \cdot 10^8$ muon DIS interactions in the decay volume for 2×10^{20} protons on target. These background events have a high multiplicity leaving a signal in the veto detectors. Applying the selection in Table 5 and the veto detector requirement based on detecting the incoming muon or the products resulting from the interaction, brings the muon inelastic background to zero. Assuming no correlation between the veto criterion and the pointing requirement for the decay vertex, an upper limit on the residual background can be set as low as 6×10^{-4} and 2×10^{-5} events (at 90% CL) for partially and fully reconstructed final states, respectively.

Selection cut	Expected background
Events reconstructed	$1.5{\cdot}10^6$
Selection cuts (IP $<$ 10 cm)	27
Selection cuts (IP $<$ 250 cm)	566
Vetoed events SBT (fully reco)	$< 2.7 \cdot 10^{-5}$
Vetoed events (partially reco)	$< 6 \times 10^{-4}$

Table 7: Summary of the muon inelastic background events expected for 2×10^{20} protons on target. The numbers with the veto requirement assume factorization with the Impact Parameter cut.

Muon combinatorial background

Random combinations of muons which enter the decay volume, either by elastic back-scattering in the surrounding cavern walls or by surviving the muon shield, may mimic signal events. The rate of fully reconstructed muons inside the SHiP spectrometer has been estimated with the full FairShip simulation to 26.3 ± 3.6 kHz during a spill. In order to study the expected combinatorial background, fully simulated muons from the sample discussed in Section 3 are used. Unique pairs of tracks are formed out of the muons that survive the shield and enter the decay volume. Kinematic and topological distributions of these reconstructed muons are shown in Figure 63 and 64.

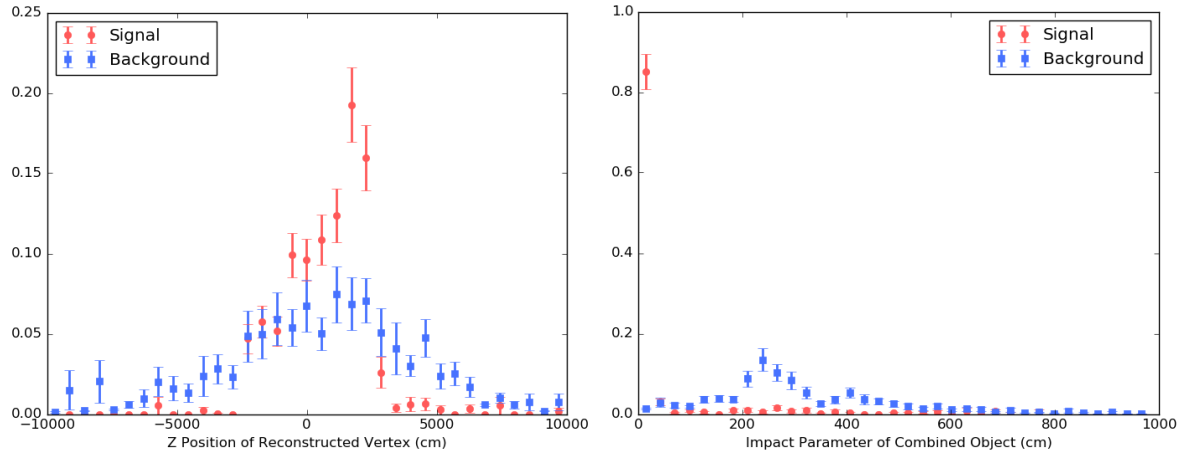

Figure 63: Vertex position in z and impact parameter for reconstructed muon combinatorial background events, compared to HNLs of mass 1 GeV/c^2 decaying to $\mu^+\pi^-$. The histograms are normalised to unit area.

Applying the selection cuts in Table 5 significantly reduces the combinatorial muon background rate, while maintaining a high signal selection efficiency for both fully and partially reconstructed final states. Table 8 summarises the expected background level.

Criteria	Expected background
Acceptance	8.5×10^{15}
Selection cuts (Table 5)	10^9
Timing	10^{-2}

Table 8: Expected background level from muon combinatorial events.

The final requirement, specifically designed to suppress combinatorial background, is the use of the timing detector, described in Section 5.3. With the rate of muons, fully reconstructed in the SHiP decay spectrometer, it is expected to have 8.5×10^{15} pairs of tracks with 2×10^{20} protons on target.

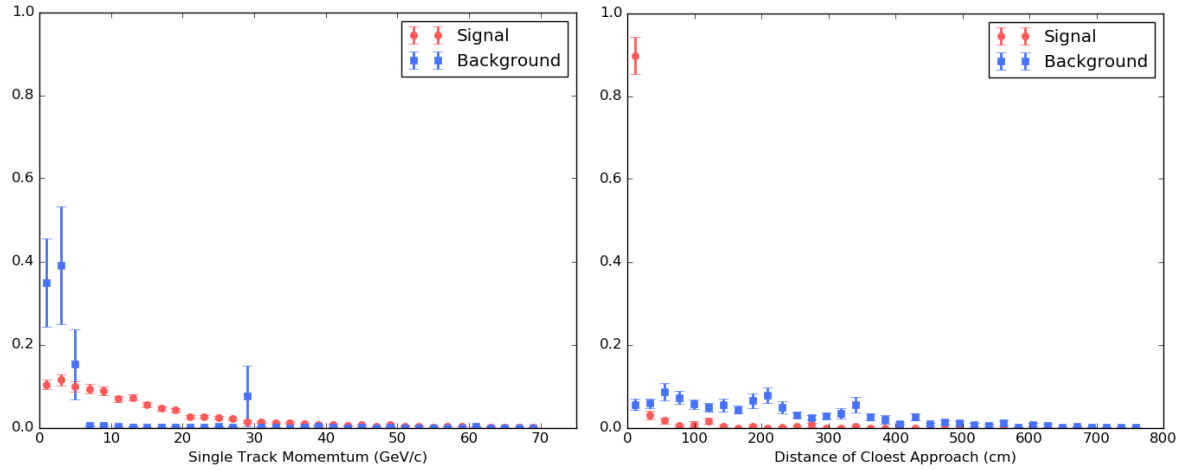

Figure 64: Track momentum and distance of closest approach between tracks for reconstructed muon combinatorial background events, compared to HNLs of mass 1 GeV/c^2 decaying to $\mu^+\pi^-$. The histograms are normalised to unit area.

Within a timing window of 340 ps, corresponding to three times the resolution of the timing detector, there are 60×10^4 pairs of tracks surviving the shield over the lifetime of the experiment. Therefore the probability to have two tracks in the same time slot of 340 ps is about 10^{-11}, which corresponds to the suppression factor of the timing detector.

Consequently, the muon combinatorial background is reduced to $1.2 \times 10^{-2} \pm 1.2 \times 10^{-2}$ events over the lifetime of the experiment. Further rejection of the combinatorial background can be achieved by employing information from the veto detectors. The majority of background muons produces multiple hits in the SBT and in the upstream muon system of the SND detector. Therefore, reconstructed tracks whose extrapolated trajectory matches hits in these sub-systems can be rejected as background. Assuming a 95% and 90% hit efficiency for the SBT and RPC detectors respectively, this criterion provides an additional suppression factor of 10^{-4}, and is found to be independent of the selections summarised in Table 8.

Background summary

In summary, Table 9 shows the upper limits for the main classes of backgrounds which can be set with the currently available simulation data samples. Simulation of neutrino background is ongoing to increase the data sample by an order of magnitude, and machine learning techniques are currently being used to generate a larger sample of muons which enter the detector acceptance for further studies of the muon combinatorial background.

Background source	Expected events
Neutrino background	< 1
Muon DIS (factorisation)	$< 6 \times 10^{-4}$
Muon Combinatorial	4.2×10^{-2}

Table 9: Expected background to the HS particle search at 90% CL for 2×10^{20} protons on target.

6.1.2 HS signal sensitivities

All signal sensitivities are obtained using the FairShip simulation framework (Section 3). The 90% confidence region is defined as the region in the parameter space where on average $\bar{N}_{\text{events}} \geq 2.3$ recon-

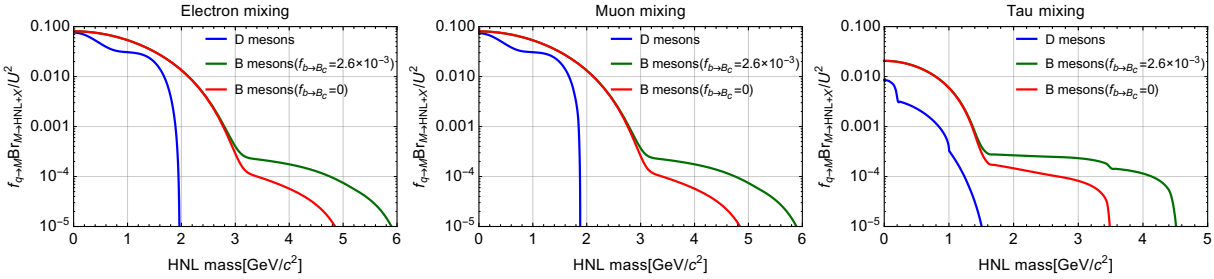

Figure 65: Meson fragmentation fraction times branching fraction of meson decays to HNL as a function of the HNL mass. Contributions from D and B mesons are shown. To demonstrate the influence of B_c mesons, we show two cases: the B_c fragmentation fraction at SHiP energies equal to that of at LHC energies: $f(b \to B_c) = 2.6 \times 10^{-3}$ (maximal contribution), and $f_{b\to B_c} = 0$. See text for details.

structed signal events are expected in the whole mass range, corresponding to a discovery threshold with an expected background level of 0.1 events.

Heavy Neutral Leptons

The *neutrino portal* consists of adding to the Standard Model new gauge-singlet fermions – heavy neutral lepton (HNLs) – that couple to the SM through the coupling $\epsilon_{ab}\bar{L}_a H_b$ where L_a is the SU(2) lepton doublet and ϵ_{ab} is anti-symmetric tensor in two dimensions. Phenomenologically, HNLs are massive Majorana particles with mass M_N that possess "neutrino-like" interactions with W and Z bosons (the interaction with the Higgs boson does not play a role in our analysis and will be ignored). The interaction strength is suppressed as compared to that of ordinary neutrinos by flavour-dependent factors (known as *mixing angles*) $U_\alpha \ll 1$ ($\alpha = \{e, \mu, \tau\}$).

The dominant production channels for HNLs in the SHiP experiment occur through weak decays of flavoured mesons [107, 108]. For HNLs with masses $M \lesssim 500\,\mathrm{MeV}/c^2$ kaon decays are the dominant production channel. While $\mathcal{O}(10^{20})$ kaons are expected at SHiP, most of them are stopped in the target or hadron stopper before decaying. As a consequence, only HNLs originating from charm and beauty mesons are included in the estimation of the sensitivity below. Figure 65 shows the production rates of HNLs used in this analysis.

The production of HNLs through the decay of charm mesons dominates for HNL masses greater than the kaon masses. For HNL masses greater than charm meson masses, decays of beauty mesons are responsible for the production of HNLs at SHiP as shown in Figure 65. For masses $M_N \gtrsim 3\,\mathrm{GeV}/c^2$ the contribution of B_c may become important and even dominant. The fraction of B_c mesons among all beauty meson (*i.e.* the fragmentation fraction $f_{b\to B_c}$) at SHiP energies is unknown. Given this uncertainty we provide two estimates:

- Assuming that $f_{b\to B_c}$ is the same as at the LHC energies $f_{b\to B_c} = 2.6 \times 10^{-3}$ [109]
- Assuming that $f_{b\to B_c} = 0$.

The main decay channels of HNLs considered in this study are shown in Figure 66, see [108] for details. Signal events were simulated through FairShip for various masses and mixing angles U_i^2 with Standard Model electron, muon and tau neutrinos as input parameters. The sensitivity to various HNL benchmark models is estimated by applying the reconstruction and selection criteria, described in Section 6.1, for partially reconstructed final states.

When estimating the contribution from HNLs produced through decays of B_c mesons, the angular distribution of B_c mesons is taken to be the same as that of B^+ mesons, based on comparisons performed with the BCVEGPY [110] and FONLL [111] packages. The energy distribution is obtained by re-scaling the energy distribution of the B^+ meson to account for the mass difference with the B_c.

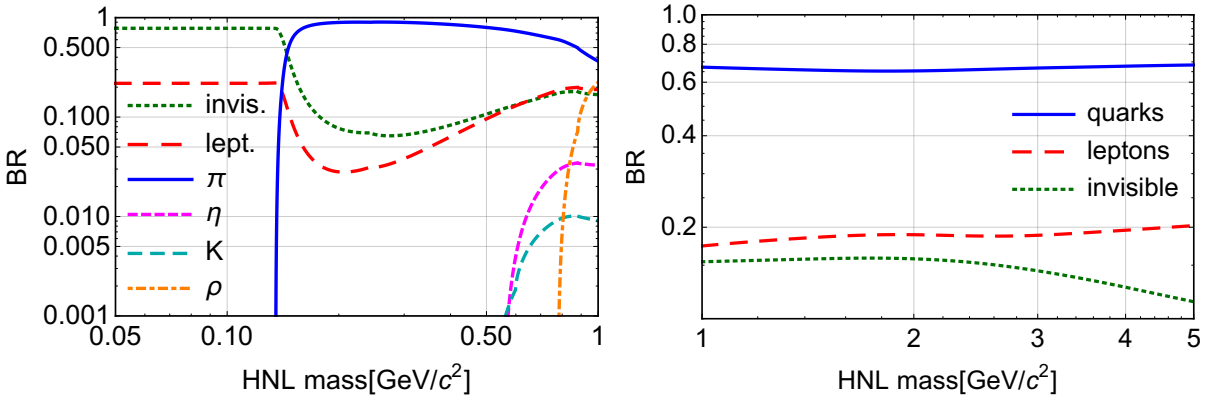

Figure 66: The branching ratios of the HNL decays for the mixing ratio $U_e : U_\mu : U_\tau = 1 : 1 : 1$. *Left panel:* region of masses below 1 GeV/c^2; *Right panel:* region of masses above 1 GeV/c^2. From [108].

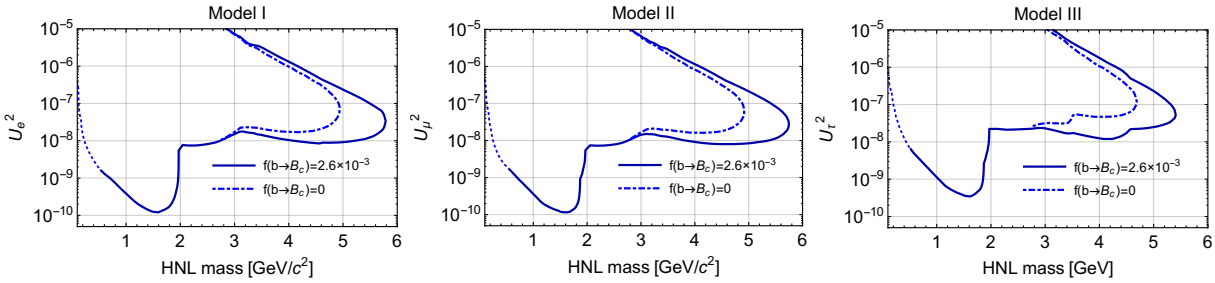

Figure 67: Sensitivity of the SHiP experiment to three HNL models. Solid curves show the contribution from B_c mesons, when the fragmentation fraction is taken equal to that at LHC energies: $f_{b\to B_c} = 2.6 \times 10^{-3}$. Dashed-dotted lines do not include contributions from B_c. Below 0.5 GeV/c^2 only production from D and B mesons is included (dotted lines). Total number of events within contour is $N \geq 2.3$.

Figure 67 presents the sensitivity curves for three HNL models, assuming particular ratios between the three HNL mixing angles [112]

- Model I (BC6), $U_e^2 : U_\mu^2 : U_\tau^2 = 52 : 1 : 1$
- Model II (BC7), $U_e^2 : U_\mu^2 : U_\tau^2 = 1 : 16 : 3.8$
- Model III (BC8), $U_e^2 : U_\mu^2 : U_\tau^2 = 0.061 : 1 : 4.3$

Figure 68 presents the sensitivity curve for HNLs, with the benchmark assumption that the ratio between the three HNL mixing angles corresponds to $U_e^2 : U_\mu^2 : U_\tau^2 = 0 : 1 : 0$.

For completeness, both the conservative curves for the case $f_{b\to B_c} = 0$, and the optimistic ones with $f_{b\to B_c} = 2.6 \cdot 10^{-3}$ are shown in all sensitivity plots.

Dark Scalars

The *scalar portal* couples a gauge-singlet scalar S to the gauge invariant combination $H^\dagger H$ made of the SM Higgs doublet:

$$\mathcal{L}_{\text{scalar}} = \mathcal{L}_{\text{SM}} + \frac{1}{2}(\partial_\mu S)^2 - \frac{M_S^2}{2} S^2 + g S H^\dagger H + \mathcal{L}_{\text{int}} \tag{1}$$

where g is the coupling constant and $\mathcal{L}_{\text{int}}$ are interaction terms that play no role in our analysis. After the spontaneous symmetry breaking the cubic term in (1) gives rise to the Higgs-like interaction of the scalar S with all massive particles with their mass times a small *mixing parameter*

$$\mathcal{L}_{S,\text{int}} = \theta S \left[\sum_f m_f \bar{f} f + M_W W_\mu^+ W_\mu^- + \dots \right] \quad \theta \equiv \frac{gv}{m_H} \ll 1 \tag{2}$$

where g is the coupling in (1), v is the Higgs VEV; m_H is the Higgs mass and $W_\mu^\pm$ is the W-boson. The sum in (2) goes over all massive fermions (leptons and quarks). Further details on the phenomenology of the scalar portal are provided in [113] as well as in [114–117]. Dark scalars are produced from decays of kaons and $B^\pm$-mesons, see Figure 69. However, as discussed for the HNLs, kaons are mainly absorbed in the hadron absorber in SHiP and here only the production via B-mesons is considered.

The hadronic decay width of the scalar S is subject to large uncertainties for masses $M_S \sim 1\,\text{GeV}/c^2$, where neither chiral perturbation theory nor perturbative QCD can provide reliable results (see discussion in [79]). In this work we use the result of [118] for S decay widths in this range. The resulting branching ratios are shown in Figure 70.

The SHiP sensitivity is calculated within the FairShip simulation framework that allows us to apply reconstruction and selection criteria described in Section 6.1. In contrast to the neutrino portal, the contribution of Dark Scalar production through B_c meson decays is negligible, thus there is no need to assess the B_c contributions to the sensitivity. The sensitivity of the SHiP experiment to Dark Scalars is shown in Figure 71.

Dark Photons

The minimal *dark photon* model considers the addition of a U(1) gauge group to the SM, whose gauge boson is a vector field called the dark photon (DP). A kinetic mixing between the dark photon and the SM U(1) gauge bosons is allowed [119], with a reduced strength parametrised by a coupling ε, also called the kinetic mixing parameter. In its simplest form, the knowledge of the mass of the dark photon m_{DP} and the kinetic mixing parameter ε is enough to characterise the model and calculate production cross section and decay properties. Different mechanisms are possible for the production of such new particles at a fixed-target experiment. Three different modes are investigated for estimating the sensitivity of the SHiP detector, considering only the primary proton-proton interactions (cascade production, which is included for HNL and Dark scalar is here ignored).

Dark photons with masses below $0.9\,\text{GeV}/c^2$ can mix with photons from neutral meson decays

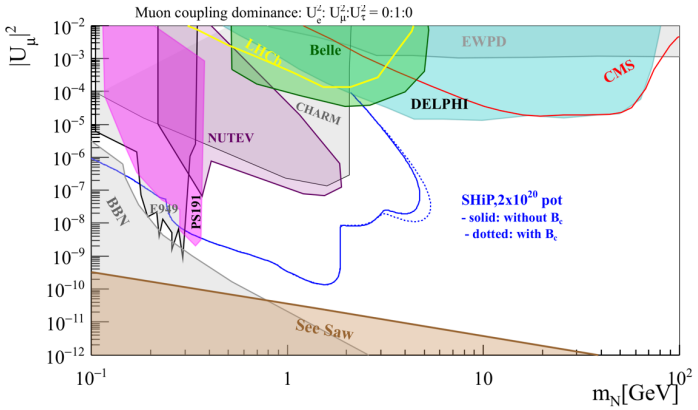

Figure 68: Sensitivity curve for HNLs, with the benchmark assumption that the ratio between the three HNL mixing angles corresponds to $U_e^2 : U_\mu^2 : U_\tau^2 = 0 : 1 : 0$.

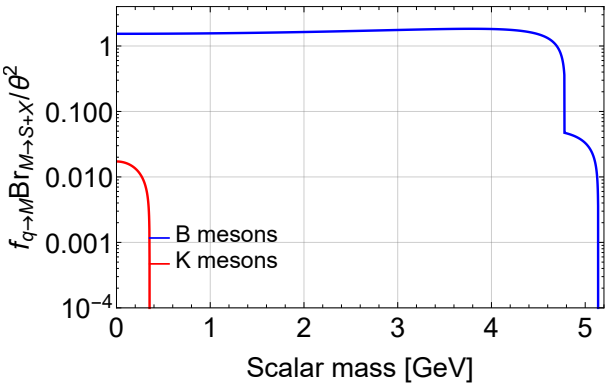

Figure 69: Scalar production from kaons ($K \to X + \pi$) and $B^{\pm}$ mesons ($B \to X + K$, $B \to X + \pi$). The y-axis shows meson fragmentation fraction times the decay branching fraction.

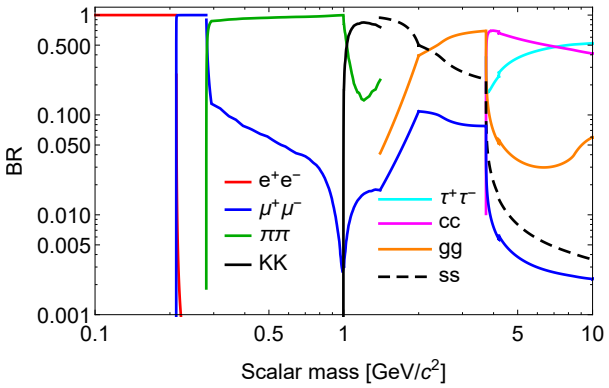

Figure 70: The branching ratios of the scalar decays. From [107].

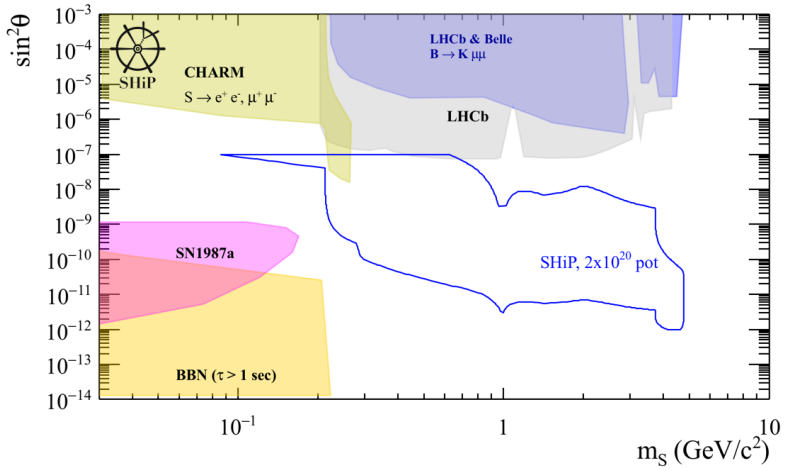

Figure 71: Sensitivity of the SHiP experiment to dark scalars. Only contribution from B mesons is taken into account.

(π^0, η, ω, η'), that are produced in non-diffractive interactions. The PYTHIA 8.2 [120] Monte Carlo (MC) generator is used to obtain an estimate of the neutral meson production rate. For an incident beam momentum of 400 GeV/c on fixed-target protons, the non-diffractive interactions represent 60%

of the total proton-proton interactions [121]. Branching ratios of mesons to dark photons are calculated according to [115, 122].

The proton-proton interaction can also lead to the radiation of a dark photon via a bremsstrahlung process, dominant for DP masses in the range 0.4–1.3 GeV/c^2. An approach identical to that of [122,123] is followed to parametrise the probability density function for producing dark photons with a given momentum and angle to the beam-line, and calculate the total production rate. Above this threshold, the dominant production mechanism happens through quark-quark annihilation into the dark photon. This process is simulated using the generic implementation of a resonance that couples both to SM fermion pairs and hidden particles as implemented in Pythia 8.2 under the "HiddenValley" Z' model [124]. The native cross section from Pythia 8.2 is used for the normalisation of the process.

The relative contribution from each process is shown in Figure 72 (left) as a function of m_{DP}, for the three production modes. Additional contributions from secondary interactions in the cascade decays on the initial proton into the target material will be the subject of future work. Only visible decays of the DP to pairs of fermions are considered here. The partial decay width of the dark photons into lepton (hadron) pairs is calculated as in [123] ([125]) as a function of m_{DP} and ε. The lifetime of the DP is then naturally set to the inverse of its total width, which is proportional to $1/\varepsilon^2$, and, which is calculated by summing all the kinematically allowed channels. The branching ratios to individual channels are set to the ratio of the partial over total width, and are hence independent of ε, shown as a function of m_{DP} in Figure 72 (right). For separating the hadronic channels into the different quark-flavoured pairs, the same relative branching ratios as those of the SM Z bosons are used [120]. PYTHIA 8.2 is used in all three production modes considered to decay the dark photon. Simulated events are then passed through the full FairShip simulation.

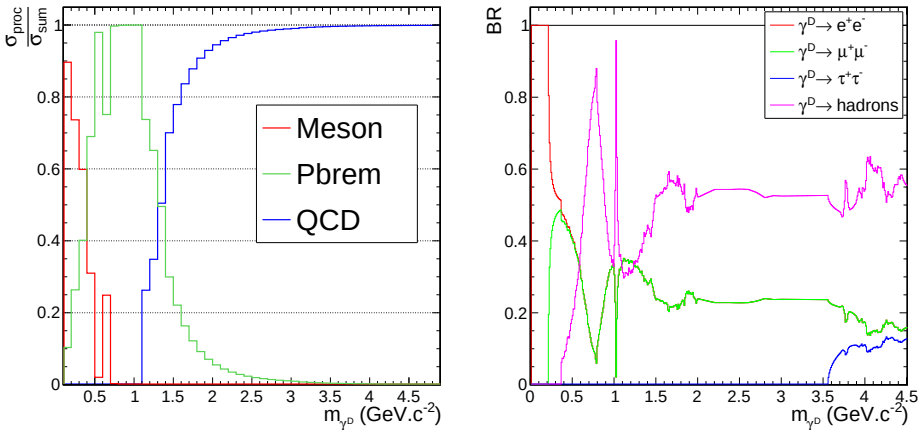

Figure 72: Left: relative contributions to the cross-section as a function of m_{DP} for the three production modes studied. Right: branching ratio of the DP into fermion pairs as a function of its mass.

The strategy of the analysis relies on identifying the decays of the DP into at least two charged particles. The reconstructed charged tracks must originate from a common vertex reconstructed inside the vaccum vessel, have a sufficient number of hits in the different tracking layers in the fiducial area of the detector. These requirements are enough to ensure that no background event will survive the selection, as demonstrated in [2, 3]. The 90% confidence level (CL) limits on the existence of a DP with given (m_{DP}, ε) are set by excluding regions where more than 2.3 events are expected. The requirement of the decay vertex to be in the vacuum vessel volume has an acceptance impact which depends on the lifetime and momentum of the m_{DP}, but it is typically between 7% and 14% for the most sensitive region of the parameter space. Once the decay vertex is selected, the reconstruction efficiency for the two-track selection is between 45% and 97%.

The rate of events is driven by two aspects: for large ε values, larger cross sections are expected

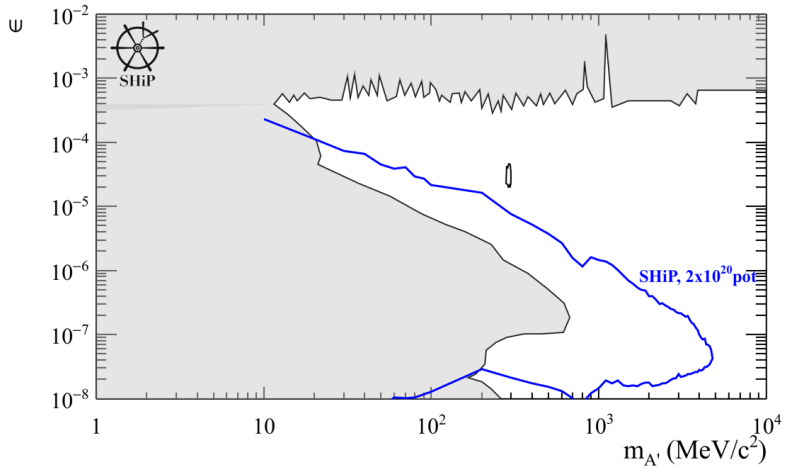

Figure 73: Expected 90% exclusion region as a function of the dark photon mass and of the kinetic mixing parameter ε, for the three production modes studied.

but the events are suppressed due to small lifetimes and decays happening before the decay vessel. As ε decreases, the cross section decreases as ε^2 but the events have more and more probability to reach the vessel and the rate increases, up to a turn-on point where the decay vertex happens after the decay vessel and/or the cross section becomes too small. Hence the 90% CL exclusion region is contained inside a lower and upper limits on ε^2 for each mass point. The dependency of the excluded region on the mass is driven by the kinematic properties of the DP and its daughters, affecting the detector acceptance and selection efficiency.

The 90% CL exclusion contour is shown in Figure 73 for the three production mode studied, in the (m_{DP},ε) plane. Exclusion contours from theoretical constraints, existing and other planned experiments sensitive to this process are overlaid. The SHiP experiment is found to have a unique sensitivity within the mass region m_{DP} ranging from 0.002 and 4.1 GeV/c^2, and ε ranging between 1.64×10^{-3} and 1.64×10^{-9}.

Axion-Like Particles

Pseudo Nambu-Goldstone bosons can arise from spontaneously broken symmetries at high energies. A prime example is the axion introduced to solve the strong CP problem in QCD with mass $\sim 10^{-5} eV$. The SHiP experiment is not sensitive to QCD axions, however other pseudo-scalar particles can feature very similarly to axions but with larger masses. These hypothetical particles are known as axion-like particles (ALPs). Here we will consider two cases: the coupling of ALPs with photons and with fermions. The couplings with fermions and photons, respectively, are given by the Lagrangian:

$$\mathcal{L} \supset \frac{\partial_\mu \phi}{f_a} \overline{\psi} \gamma^\mu \gamma^5 \psi. \tag{3}$$

$$\mathcal{L} \supset \frac{\alpha}{4\pi f_a} \phi F^{\mu\nu} F_{\mu\nu}. \tag{4}$$

In both cases the interaction is suppressed by the factor $1/f_a$, where f_a is the scale of the spontaneous symmetry breaking. The ALPs coupling to fermions have an analogous production mechanism to that of Dark Scalars. The sensitivity for ALPs coupling to fermions, compared to previous experiments is shown in Figure 74. This is calculated with a fast simulation that was tuned with the FairShip simulation, and takes into account the geometrical acceptance.

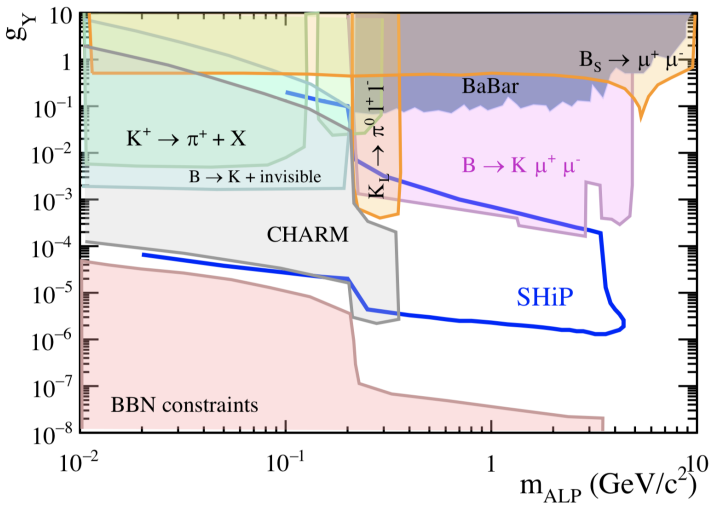

Figure 74: SHiP sensitivity to ALP coupling to fermions

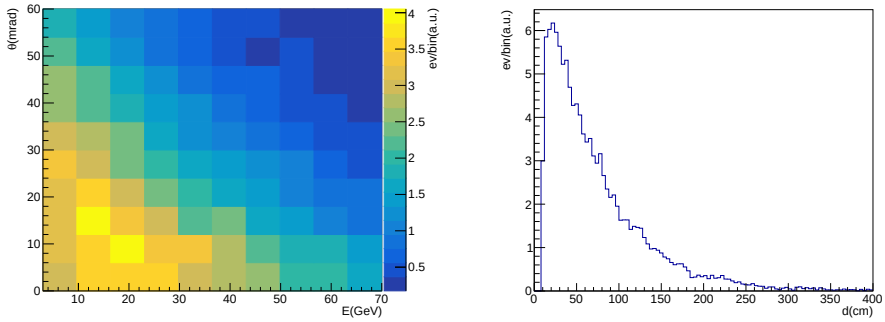

Figure 75: Left: angle of incidence θ (in mrad) vs energy E (in GeV) of photons. Right: distance between the two photons at the SplitCal surface for 600 MeV/c^2 ALP mass decaying to two photons in the ToyMC.

For the sensitivity to ALPs, SHiP has used the model with an exclusive coupling to photons as benchmark channel (ALP $\to \gamma\gamma$), whose theoretical framework is discussed in Reference [126], and for which SHiP has unique sensitivity in the mass range between 200 MeV/c^2 and 1 GeV/c^2. In the phenomenological study [126], the authors only considered a final state with two reconstructed photons in the detector, with energy E>3 GeV and minimum distance on the calorimeter surface of 10 cm.

A fast simulation of the signal was developed, based on the theoretical formulae of [126]. ALPs were assumed to be produced in the target and let decay in the decay vessel. Figure 75 left shows the angle of incidence θ on the SplitCal of photons vs energy E for 600 MeV/c^2 ALP mass, showing that angles are up to 30 mrad and are correlated with energy. Figure 75 (right) shows the distance d between the two photons at the SplitCal surface for 600 MeV/c^2 ALP mass. For lower ALP masses the distribution of d shrinks to lower values making shower separation and direction reconstruction more challenging. The two photons of the ALP decay were smeared in angle and energy according to resolutions consistent with the values obtained from the SplitCal simulation, i.e. an angular resolution of $\sigma_\theta \cdot \sqrt{\mathrm{E}} = 16\,\mathrm{mrad} \cdot \sqrt{\mathrm{GeV}}$ and a relative energy resolution $\sigma_\mathrm{E}/\mathrm{E} = 15\%/\sqrt{\mathrm{E}}$ (a precise determination of the coefficients of these functions from the SplitCal simulation is left for future work). For small angles, the invariant mass is proportional to $\mathrm{E} \cdot \theta$; for ALP decays in the SHiP experiments, the angular resolution is by far the dominant contribution to the mass resolution. The mass resolution, obtained by fitting mass distributions

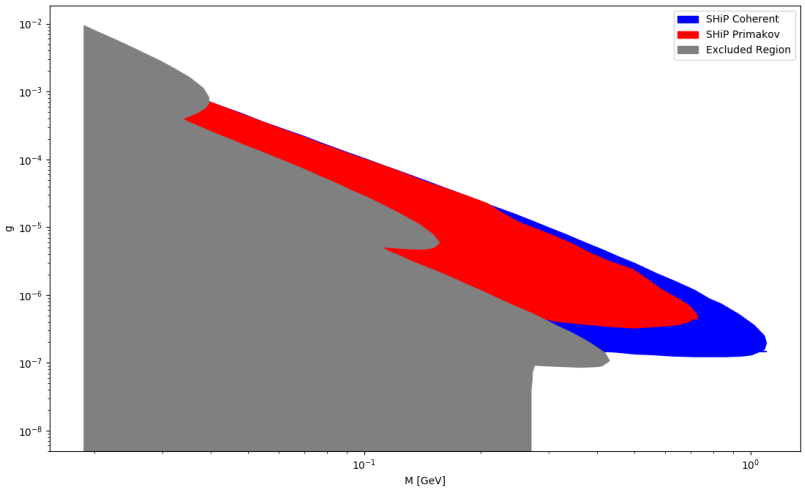

Figure 76: SHiP sensitivity to ALP decaying to two photons

with a Gaussian, is found to be 66 MeV/c^2, 110 MeV/c^2 and 115 MeV/c^2 for 0.2 GeV/c^2, 0.6 GeV/c^2 and 1 GeV/c^2 ALP mass, respectively.

The background suppression, does not depend on the capability of reconstructing the photon direction while mass reconstruction is crucially dependent on it. The background was simulated in with FairShip. The neutrinos and the muons can interact in the material upstream, aside or inside the decay vessel and yield photons that mimic the signal. To suppress this kind of background both charged and neutral particle veto detectors of different kinds are used, exploiting the high multiplicity topology of both deep inelastic neutrino and muon scattering events. Coherent neutral current neutrino scattering, with the production of the single neutral pion, is in principle an irreducible background but, since most interactions occur at the entrance window of the decay vessel, it can be suppressed by a kinematical cut by only measuring the energy and the position in the calorimeter and making the hypothesis of the neutral pion mass, with a small signal inefficiency of the order of 5% for a 600 MeV/c^2 ALP mass.
With these cuts, the Monte Carlo simulation shows that for the whole SHiP data-taking, one expects for the ALP search with the two-photon decay less than 0.1 background events. Figure 76 shows the the SHiP sensitivity to ALP decaying to two photons compared to other experiments.

6.2 Sensitivity to Light Dark Matter

LDM scattering in the emulsion spectrometer produces an isolated electromagnetic shower originating from the recoil electron. The modules of the emulsion spectrometer act as fine sampling calorimeters with more than five active layers per radiation length X_0 over a total thickness of ten X_0, allowing the electron energy and incident angle to be measured accurately. The micrometric accuracy of the emulsion is crucial for detecting any associated activity at the origin of the electromagnetic shower in order to discriminate the LDM signal from background induced by neutrino interactions.

The background to the LDM search, which comes primarily from neutrino interactions with only one reconstructed electron at the interaction vertex, has been simulated with the help of GENIE. A neutrino scattering event is tagged as background if the interaction vertex is within the geometrical acceptance, and if the electron is accompanied by additional visible activity, such as charged tracks or photons. At the final stage of the selection, the LDM signal is discriminated from neutrino events with the same LDM elastic scattering topology, using the kinematic correlation between the energy and

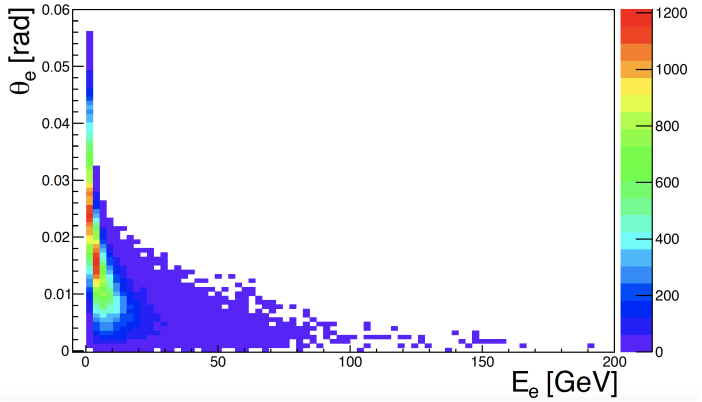

Figure 77: Correlation between the electron energy and the scattering angle for 1 GeV/c^2 Dark photons produced in the decay of mesons and decaying into fermionic LDM with a benchmark mass $m_\chi = m_{A'}/3$.

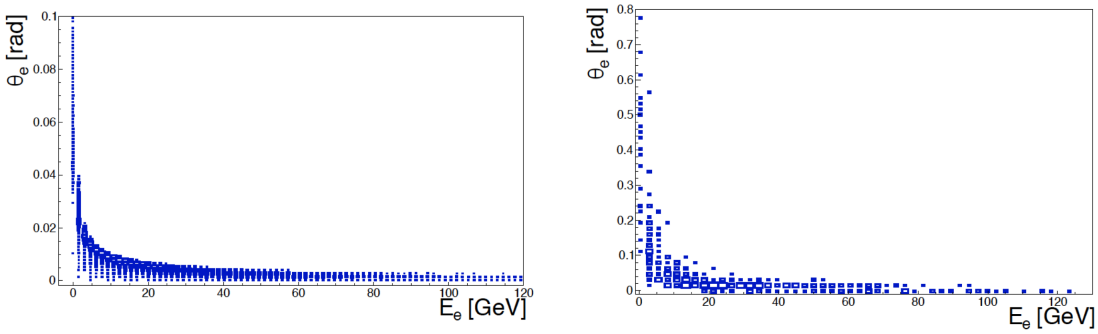

(a) (b)

Figure 78: Electron scattering angle with respect to the incoming neutrino direction versus the electron energy in case of elastic (a) and quasi-elastic (b) scattering.

the azimuthal angle of the scattered electron which is shown in Figure 77 for LDM scattering, and in Figure 78 for neutrino background.

The resulting estimate of the background levels for 2×10^{20} protons on target is shown in Table 10 for the various classes of neutrino interactions. The main source of background for LDM search is due to elastic and quasi-elastic scattering events from ν_e and $\bar{\nu}_e$. In neutrino interactions $\nu_e\, n \to e^-\, p$, the background comes from events where the proton momentum is below 170 MeV/c. This boundary can be relaxed if a more sophisticated tracking algorithm for soft protons is exploited, *e.g.* by means of a Machine Learning approach. Conversely the anti-neutrinos mimic the LDM signal, being $\bar{\nu}_e\, p \to e^+ n$ irreducible for the presence of an outgoing neutron which cannot be detected.

Background	ν_e	$\bar{\nu}_e$	ν_μ	$\bar{\nu}_\mu$	all
Elastic Scattering on e^-	81	45	56	35	217
Quasi-elastic Scattering	245	236	-	-	481
Resonant Scattering	8	77	-	-	85
Deep Inelastic Scattering	-	14	-	-	14
Total	334	372	56	35	797

Table 10: Number of background events in the LDM search after the selection for 2×10^{20} protons on target.

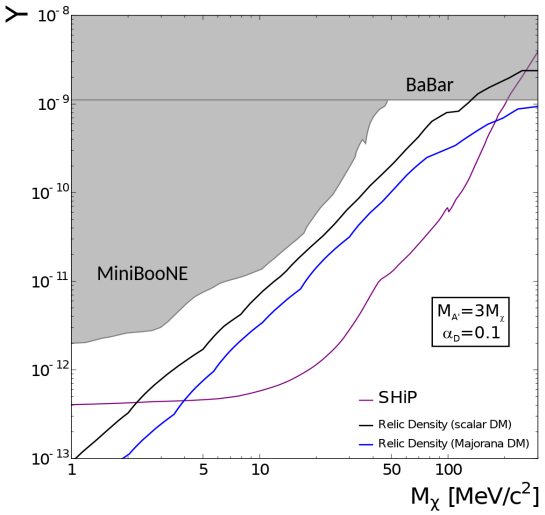

Figure 79: SHiP sensitivity to LDM produced in dark photon decays. The coupling is given as $Y = \epsilon^2\alpha'_D(m_\chi/m_{A'})^4$. Only meson decays and Drell-Yan processes are considered here as production mechanisms for the dark photons. The grey shaded regions represent the parameter space which has been already ruled out by the searches at the BaBar and the MiniBooNE experiments.

In order to perform a complete simulation of the LDM production and interaction in SHiP, the MadDump tool, developed within MadGraph5 [127], has been interfaced with FairShip.

The expected SHiP sensitivity for 2×10^{20} protons on target, taking into account the geometrical acceptance and the selection criteria, is shown in Figure 79 in the parameter space (m_χ,Y), where $Y = \epsilon^2\alpha'_D(m_\chi/m_{A'})^4$. In the region from a few MeV/c^2 to $\sim 200\,\mathrm{MeV}/c^2$ the SHiP sensitivity reaches below the limit which gives the correct relic abundance of dark matter. The current estimate is conservative since at the moment only meson decays and Drell-Yan production have been considered as a source of dark photons decaying to LDM.

In case an excess of events is observed, the use of a bunched proton beam (Section 2.1.1) and a Target Tracker with $\sim$100 ps resolution would unambiguously discriminate between a new massive particle, and nearly massless neutrinos by exploiting the difference in the time of flight.

6.3 Physics with neutrinos

The neutrino fluxes produced at the beam dump were estimated with FairShip, including the contribution from cascade production in the target. The energy spectra of different neutrino flavors are shown in Figure 80 (left), and the integrated yield at the beam dump for 2×10^{20} protons on target is shown in the left column of Table 11. The number of charged-current (CC) deep-inelastic interactions in the neutrino target is evaluated by convoluting the generated neutrino spectrum with the cross section provided by GENIE. The expected number of CC DIS in the target of the SND detector is reported in the right column of Table 11, and the corresponding energy spectra in Figure 80 (right).

The distance of the Scattering Spectrometer from the downstream end of the proton target, as well as the compact transverse area of the emulsion target, reduce the flux to about 2% and 1% for electron and muon neutrinos, respectively. The acceptance for the ν_τ component amounts to $\sim$4%.

The nuclear emulsion technology combined with the information provided by the muon identification system makes it possible to identify the three different neutrino flavors in the SND detector. The neutrino flavour is determined through the flavour of the primary charged lepton produced in neutrino charged-current interactions. The lepton identification is also used to classify the tracks produced in the

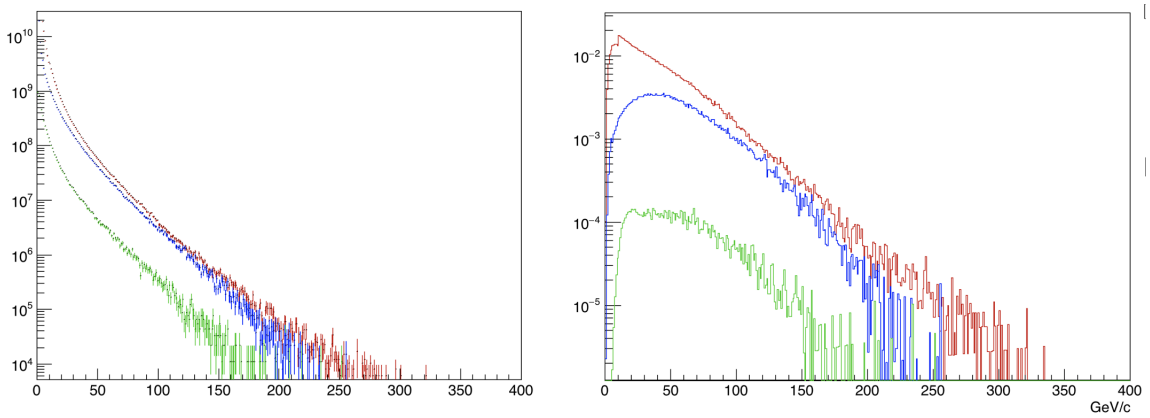

Figure 80: Left: energy spectra of muon (red), electron (blue) and tau (green) neutrinos at the beam dump. Right: energy spectra of neutrinos after their deep inelastic interactions with the Scattering Spectrometer. Units are arbitrary.

	<E>[GeV]	Beam dump	<E>[GeV]	CC DIS interactions
N_{ν_e}	4.1	2.8×10^{17}	59	1.1×10^{6}
N_{ν_μ}	1.5	4.2×10^{18}	42	2.7×10^{6}
N_{ν_τ}	7.4	1.4×10^{16}	52	3.2×10^{4}
$N_{\overline{\nu}_e}$	4.7	2.3×10^{17}	46	2.6×10^{5}
$N_{\overline{\nu}_\mu}$	1.6	2.7×10^{18}	36	6.0×10^{5}
$N_{\overline{\nu}_\tau}$	8.1	1.4×10^{16}	70	2.1×10^{4}

Table 11: Expected neutrino flux for different neutrino flavors at the beam dump (left) and charged-current deep-inelastic interactions in the Scattering Spectrometer (right). 2×10^{20} protons on target were assumed.

τ decay and, therefore, to identify the τ decay channel. In addition, the target magnetisation will allow for the first time to distinguish between ν_τ from $\overline{\nu}_\tau$.

The available statistics will allow to test lepton flavor violation in the neutrino sector.

6.3.1 ν_τ detection

The neutrino detector has the unique capability of detecting all three neutrino flavors and of distinguishing neutrinos from anti-neutrinos. As an example, the event display of a ν_τ interaction with $\tau \rightarrow \mu$ decay in the Scattering and Neutrino Detector and in the ECC brick is shown in Figure 81 and Figure 82, respectively. Electron neutrinos are the only exception because electrons shower in the emulsion target before their charge can be measured.

The identification of ν_τ and $\overline{\nu}_\tau$ interactions requires, as a first step, the detection of both the neutrino interaction and the τ lepton decay vertices. Two procedures, the event location and decay search, are applied. Neutrino interactions are searched for in the brick in a fiducial volume excluding the regions within 1 mm from the transverse edges of the brick and within 5 mm from the downstream edge of the brick. This results in a geometrical efficiency of approximately 96%.

The location of a neutrino interaction consists of reconstructing the neutrino interaction vertex and its three-dimensional position with micrometric accuracy. To identify a neutrino interaction vertex the presence of at least two tracks with a momentum above 1 GeV/c and a slope $\tan\theta < 1$, having an impact

parameter lower than 10 μm, is required. Tracks having an impact parameter larger than 10μm from the reconstructed neutrino vertex are considered as a hint for a secondary vertex.

The first selection of ν_τ lepton candidates is based on purely topological criteria. Once the primary neutrino interaction vertex has been defined, possible secondary vertices induced by short-lived particles decays are searched for. This is done by a decay search procedure: tracks are defined as belonging to a secondary vertex if the kink angle and the impact parameter of the daughter track with respect to the primary vertex are larger than 20 mrad and 10 μm, respectively.

The identification of the neutrino flavor is performed through the identification of the charged lepton produced in the charged current interaction with the passive material of the brick. The lepton flavor identification is also important to classify the daughter tracks produced by τ decay, thus identifying the decay channel, as well as to identify charmed hadrons induced by neutrino interactions. Muon neutrinos are identified through the identification of the muon at the primary vertex. The muon identification is performed by the muon identification system. A track entering this system is classified as a muon if it crosses at least 40 cm in the passive material. The identification of the electron neutrinos is performed by exploiting the nuclear emulsion capability of identifying individual tracks in the shower. With a total thickness corresponding to 10 X_0, the emulsion brick acts as a calorimeter with a high sampling, given its $\sim$5 sensitive layers every radiation length. This method, largely exploited in the OPERA experiment, provides an electron identification efficiency of about 90%. The use of Target Tracker stations might improve the identification efficiency for electrons.

The charge measurement of τ decay products is used to separate ν_τ and $\overline{\nu}_\tau$. The charge of hadrons and muons is measured by the Compact Emulsion Spectrometer, the Muon Tracker, and by the muon identification system. The electron decay channel of the τ lepton is not considered for the discrimination of ν_τ and $\overline{\nu}_\tau$.

The efficiency at the different steps, as well as the overall identification efficiency, is reported in Table 12.

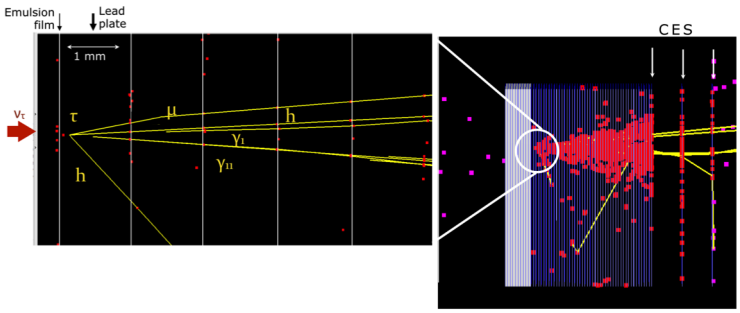

Figure 81: ν_τ interaction and subsequent $\tau \rightarrow \mu$ decay in the Emulsion Target.

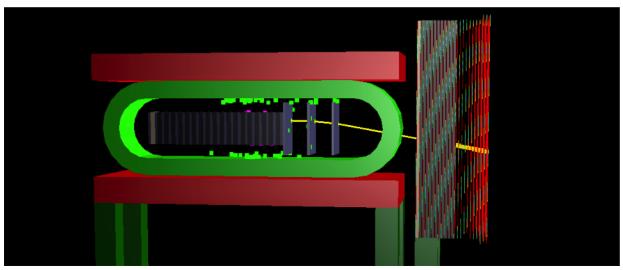

Figure 82: ν_τ interaction and subsequent $\tau \rightarrow \mu$ decay in the whole Scattering and Neutrino Detector.

Efficiency	ν_τ					$\overline{\nu}_\tau$				
	$\tau \to \mu$	$\tau \to h$	$\tau \to 3h$	$\tau \to e$	total	$\tau \to \mu$	$\tau \to h$	$\tau \to 3h$	$\tau \to e$	total
Geometrical	0.96	0.95	0.96	0.95	0.96	0.95	0.95	0.95	0.96	
Location	0.66	0.66	0.67	0.66	0.67	0.83	0.82	0.84	0.84	0.83
Decay search	0.45	0.45	0.51	0.45	0.45	0.49	0.48	0.54	0.49	0.49
PID	0.31	0.44	0.51	0.41	0.42	0.42	0.47	0.54	0.44	0.44
Charge	0.23	0.29	0.22	-	0.21	0.31	0.30	0.24	-	0.24
Total	0.23	0.29	0.22	-	0.28	0.31	0.30	0.24	-	0.29

Table 12: ν_τ and $\overline{\nu}_\tau$ efficiencies for the different decay channels at differenst steps of the selection.

By combining the overall neutrino CC DIS interaction yield in the target and the detection efficiencies reported in Table 12, it is possible to estimate the expected number of ν_τ and $\overline{\nu}_\tau$ interactions observed in the different decay channels. Since the charge of the electron is not measurable, only an inclusive measurement of ν_τ and $\overline{\nu}_\tau$ is possible in the $\tau \to e$ decay channel.

The unprecedented statistics of about 6000 ν_τ and 5000 $\overline{\nu}_\tau$ detected interactions are expected for 2×10^{20} protons on target, as reported in Table 13.

Decay channel	ν_τ	$\overline{\nu}_\tau$
$\tau \to \mu$	1200	1000
$\tau \to h$	4000	3000
$\tau \to 3h$	1000	700
total	6200	4700

Table 13: Expected number of ν_τ and $\overline{\nu}_\tau$ signal events observed in the different τ decay channels, except for the $\tau \to e$, where the lepton number cannot be determined.

6.3.2 Neutrino induced charm production

The expected charm yield with respect to the neutrino charged current interactions ($\sigma_{charm}/\sigma_{CC}$) was estimated using the GENIE generator. The charm fractions are reported in the right column of Table 14 for electron and muon neutrinos.

In 2×10^{20} protons on target, more than $\sim 2 \times 10^5$ neutrino induced charmed hadrons are expected, as reported in left column of Table 14. The total charm yield exceeds the statistics available in previous experiments by more than one order of magnitude. It is worth noting that the emulsion experiment with the largest neutrino flux was CHORUS [128–130], where only 2013 charm candidates coming from ν_μ and 32 coming from $\overline{\nu}_\mu$ interactions were reported [131]. No charm candidate from electron neutrino interactions was ever reported.

Therefore all the studies on charm physics performed with neutrino interactions will be improved and some channels inaccessible in the past will be explored. This includes the double charm production cross-section [132, 133] and the search for pentaquarks with charm quark content [134]. Charmed hadrons produced in neutrino interactions are also important to investigate the strange quark content of the nucleon. The statistics available in SHiP will have impact on the knowledge of the nucleon strangeness.

6.3.3 ν_τ magnetic moment

The presence of a non-zero magnetic moment adds an extra component to the elastic cross-section for the process $\nu e^- \to \nu e^-$ that in the SM involves only the neutral current, except for ν_e. Therefore, an

	<E> (GeV)	CC DIS with charm prod	Charm fractions (%)
N_{ν_μ}	55	1.3×10^5	4.7
N_{ν_e}	66	6.0×10^4	5.7
$N_{\overline{\nu}_\mu}$	49	2.5×10^4	4.2
$N_{\overline{\nu}_e}$	57	1.3×10^4	5.1
total		2.3×10^5	

Table 14: Left: Expected CC DIS neutrino interactions with charm production for 2×10^{20} protons on target. Right: relative charm production yield per electron and muon neutrinos CC DIS interaction.

increase of the measured cross-section can prove the hypothesis of anomalous magnetic moment. So far, non-zero magnetic moment for ν_e and ν_μ has been excluded down to $\mu_{\nu_e} < 1.9 \times 10^{-11}\mu_B$ and to $\mu_{\nu_\mu} < 6.9 \times 10^{-10}\mu_B$ [135], respectively. With a few thousand ν_τ CC interactions in the Scattering and Neutrino Spectrometer, the SHiP experiment can significantly constrain the ν_τ magnetic moment.

In the elastic scattering of a neutrino on an electron, the scattering angle of the outgoing electron with respect to the direction of the incoming neutrino is limited, in the laboratory frame, by kinematic constraints [136]:

$$\theta^2_{\nu-e} < \frac{2m_e}{E_e}.$$

Therefore, for $E_e > 1$ GeV, $\theta_{\nu-e}$ is smaller than 30 mrad. This can help suppressing the background from events with the same topology.

The main background sources for this analysis are: (i) neutrino elastic scattering (ES) with electrons of the detector target, (ii) electron neutrino and anti-neutrino quasi elastic scattering (QE) with nucleons of the target with non detected outgoing nucleons, (iii) charged current deep-inelastic interactions (DIS) of electron neutrinos and anti-neutrinos with nucleons in the detector target with no revealed hadrons in the final state, and (iv) electron neutrino and anti-neutrino resonant processes. In order to take into account the uncertainty on the neutrino interaction position in the detector target, a smearing of the electron angle by 1 mrad was introduced although the angular uncertainty is dominated by the measurement accuracy. The GENIE generator was used to estimate the number of expected background events surviving the following selection criteria: only the electron reconstructed in the final state, $E_e > 1$ GeV, $\theta_{\nu-e} <$ 30 mrad. The overall contribution from different background sources amounts to 14×10^3 events, mainly from QE processes.

Denoting with Φ_{ν_τ} the incoming tau neutrino flux on the detector, with N the number of nucleons in the neutrino target, with σ^μ the contribution of the non-zero magnetic moment to the cross-section and with $\mu_B = 5.8 \times 10^5 eVT^{-1}$ the Bohr magneton, the number of expected events for a magnetic moment μ_ν is given by:

$$n_{evt} = \frac{\mu^2_\nu}{\mu^2_B} \times \int \Phi_{\nu_\tau}\sigma^\mu N dE = 4.3 \times 10^{15}\frac{\mu^2_\nu}{\mu^2_B}$$

Assuming a 5% systematic uncertainty, the evidence for a tau neutrino anomalous magnetic moment with a significance of 3σ requires the observation of an excess of about 540 events over the background. Hence, a region down to a magnetic moment $1.3 \times 10^{-7}\mu_B$ could be explored.

7 Project plan and cost

All of SHiP's sub-systems have undertaken genuine programs of prototyping to validate their performance with beam tests of small scale prototypes, as summarised in the corresponding sub-sections of Chapter 4 and 5. The results have been used in the simulation of the expected physics performance. The next level of prototyping is ongoing and consists in the preparation of larger-scale prototypes aiming to measure their global performance in beam tests in 2021, and corroborating the manufacturing techniques. This ensures validating the detector concepts in time for the Technical Design Reports in 2022, and also serves as the basis for the cost and planning of the experiment. The engineering of the muon shield and the straw tracker, and the design of the calorimeter with the required angular resolution for the ALP$\rightarrow \gamma\gamma$ reconstruction, are considered to be particularly challenging projects.

The proposed schedule for both the SHiP experiment and the Beam Dump Facility is largely driven by the CERN long-term accelerator schedule and the unique opportunity to fully exploit the current SPS in the LHC Run 4 and Run 5. At the same time it respects the technical constraints and the operating schedule of the CERN beam facilities during the construction. The civil engineering required for the Beam Dump Facility is an important driver of the time to completion. The global time-line is shown in Figure 83. It has been elaborated in collaboration with the Beam Dump Facility Working Group. More details can be found in the BDF Comprehensive Design Study report [6].

The schedule requires preparation of final prototypes and the TDRs for the detector by end of 2022. The schedule foresees three years for the continued detector R&D, prototyping, and validation. With the past three years of Comprehensive Design Study, and first prototypes of all subsystems already constructed and tested, this amount of time is considered sufficient with margins for financial delays. It is estimated that the detector production will require two to three years, and that the detector assembly and installation, including infrastructure, will require another two years. Most of the experimental facility can be constructed in parallel to operating all of the current beam facilities. However, to minimize the impact on the availability of beam in the CERN North Area during the connection of the facility to the existing beam line, and to fully profit from the operation of the accelerators in the LHC Run 4, the last phase of civil engineering and installation of the facility and the SHiP detector is planned for the Long Shutdown 3, allowing commissioning and starting data taking early in Run 4.

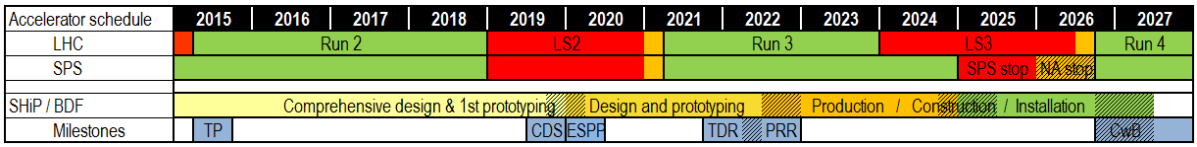

Figure 83: Global project schedule for the Beam Dump Facility and the SHiP detector. CDS, TDR, PRR mark the submission of the Comprehensive Design Study report, submission of Technical Design Reports, and Production Readiness Reviews for the SHiP detector, and CwB marks commissioning with beam.

A Class 3 $(^{+(10-30)\%}_{-(10-20)\%})$ cost estimate based on a detailed breakdown of each item in the conceptual design of the detector, was prepared for the Technical Proposal [3, 4]. The cost estimate for the detector is reproduced in Table 15 including the Muon Shield. A new cost estimate is in preparation for the Comprehensive Design Study report which will be submitted in the second half of 2019. It is expected that the cost will remain within the uncertainty of the TP cost estimate. Below is a summary of the changes since the TP as indicators of the impacts on the cost.

- The magnetisation of the hadron stopper was not included in the TP.
- The Muon Shield optimization has led to a magnet system which is 35 m in length instead of 48 m, and has 1300 tonnes of magnetic mass instead of 2900 tonnes, required in the TP.
- The magnet around the LDM/neutrino target, instrumented with emulsion and the Target Tracker, was added after the TP. Including the power converter it was estimated to 1.5 MCHF.

- The Muon Magnetic Spectrometer of the Scattering and Neutrino Detector was replaced with a conventional muon identification system without magnetization.
- The Upstream Veto Tagger has been removed. It has been shown that the SND muon system can perform the same function.
- The original Decay Volume, shaped as an elliptical cylinder with inner dimensions $5 \times 10\,\mathrm{m}^2$, has been redesigned as a conical frustum with inner dimensions of $1.7 \times 4.4\,\mathrm{m}^2$ upstream, and $5 \times 10\,\mathrm{m}^2$ downstream. The length is maintained at $50\,\mathrm{m}$. It has been shown that a pressure of $10^{-3}\,\mathrm{bar}$ is sufficient (TP: $10^{-6}\,\mathrm{bar}$).
- The in-vacuum Straw Veto Tagger has been removed.
- The Spectrometer Straw Tracker stations and the vacuum tank through the spectrometer magnet have been designed with transverse dimensions of $5 \times 10\,\mathrm{m}^2$ throughout.
- The Spectrometer Straw Tracker tube diameter has been changed from 10 mm to 20 mm, halving the total number of tubes.
- Further design studies of the spectrometer vacuum tank, the straw tracker mechanics and interfaces with the spectrometer magnet have shown that this section is more complex than initially expected.
- The shashlik-based Electromagnetic Calorimeter has been replaced with a calorimeter based on two different types of active layers, in order to extend its capability to reconstruct two-photon final states. While most sampling layers are based on scintillating bars, resulting in a significant cost reduction compared to the shashlik technology, a few high-precision layers are instrumented with micro-pattern or alternatively scintillating fibre detectors.
- The Hadron Calorimeter has been removed, only the absorber is kept as the first muon filter. The new Electromagnetic Calorimeter is expected to be capable of providing sufficient identification for low momentum particles.
- The original muon system with scintillating bars has been replaced by a system based on scintillating tiles with SiPM readout.

The production and the construction of the detector is based on the concept of deliverables, which includes the detector components and assembly, the associated electronics and infrastructure systems, as well as the transport to CERN and the specific operations related to the installation.

Item		Cost (MCHF)
Muon Shield		**11.4**
Scattering and Neutrino Detector		**11.6**
Emulsion Target (no magnet)	6.8	
Target Tracker	2.5	
Muon Magnetic Spectrometer	2.3	
Decay Spectrometer		**46.8**
Decay Volume	11.7	
Surround Background Tagger	2.1	
Upstream Veto Tagger	0.1	
Straw Veto Tagger	0.8	
Spectrometer Straw Tracker	6.4	
Spectrometer Magnet	5.3	
Spectrometer Timing Detector	0.5	
Electromagnetic Calorimeter	10.2	
Hadron Calorimeter	4.8	
Muon Detector	2.5	
Muon iron filter	2.3	
Computing and online system		**0.2**
Total		**70.0**

Table 15: Breakdown of the cost of the SHiP detectors and the Muon Shield, including infrastructure, as estimated for the Technical Proposal.

8 Status of the SHiP Collaboration

The SHiP Expression of Interest was submitted to SPSC in October 2013. This was followed by the Technical Proposal submitted to the SPSC in April 2015. The SHiP Technical Proposal was successfully reviewed by the SPSC and the CERN RB up to March 2016, with a recommendation to prepare a Comprehensive Design Study report by 2019.

SHiP is currently a collaboration of 53 institutes and 4 associated institutes, in total representing 18 countries, CERN and JINR. The formal organisation of SHiP consists of a Country Representative Board (CRB), Interim spokesperson, Technical Coordinator and Physics Coordinator, and the group of project conveners as elected and ratified by the CRB. The organisation has been adopted for the Comprehensive Design Study phase.

Bibliography

[1] W. Bonivento et al., *Proposal to Search for Heavy Neutral Leptons at the SPS*, [arXiv:1310.1762].

[2] S. Alekhin et al., *A facility to Search for Hidden Particles at the CERN SPS: the SHiP physics case*, *Rept. Prog. Phys.* **79** (2016), no. 12 124201, [arXiv:1504.04855].

[3] **SHiP** Collaboration, M. Anelli et al., *A facility to Search for Hidden Particles (SHiP) at the CERN SPS*, [arXiv:1504.04956].

[4] **SHiP** Collaboration, M. Anelli et al., *A Facility to Search for Hidden Particles (SHiP) at the CERN SPS*, Tech. Rep. CERN-SPSC-2015-040, SPSC-P-350-ADD-2, 2015.

[5] Physics Beyond Colliders Study Group. https://pbc.web.cern.ch/, 2016.

[6] C. C. Ahdida, M. Calviani, B. Goddard, R. Jacobsson, and M. Lamont, *SPS Beam Dump Facility Comprehensive Design Study* , Tech. Rep. CERN-PBC-REPORT-2018-001, CERN, Geneva, December 2018.

[7] **ATLAS** Collaboration, G. Aad et al., *Combined search for the Standard Model Higgs boson using up to* $4.9\,fb^{-1}$ *of pp collision data at* $\sqrt{s} = 7$ *TeV with the ATLAS detector at the LHC*, *Phys.Lett.* **B710** (2012) 49–66, [arXiv:1202.1408].

[8] **ATLAS** Collaboration, G. Aad et al., *Observation of a new particle in the search for the Standard Model Higgs boson with the ATLAS detector at the LHC*, *Phys. Lett.* **B716** (2012) 1–29, [arXiv:1207.7214].

[9] **CMS** Collaboration, S. Chatrchyan et al., *Combined results of searches for the standard model Higgs boson in pp collisions at* $\sqrt{s} = 7$ *TeV*, *Phys. Lett.* **B710** (2012) 26–48, [arXiv:1202.1488].

[10] **CMS** Collaboration, S. Chatrchyan et al., *Observation of a new boson at a mass of* 125 *GeV with the CMS experiment at the LHC*, *Phys.Lett.* **B716** (2012) 30–61, [arXiv:1207.7235].

[11] F. Bezrukov, M. Yu. Kalmykov, B. A. Kniehl, and M. Shaposhnikov, *Higgs Boson Mass and New Physics*, *JHEP* **10** (2012) 140, [arXiv:1205.2893].

[12] G. Degrassi, S. Di Vita, J. Elias-Miro, J. R. Espinosa, G. F. Giudice, G. Isidori, and A. Strumia, *Higgs mass and vacuum stability in the Standard Model at NNLO*, *JHEP* **08** (2012) 098, [arXiv:1205.6497].

[13] D. Buttazzo, G. Degrassi, P. P. Giardino, G. F. Giudice, F. Sala, A. Salvio, and A. Strumia, *Investigating the near-criticality of the Higgs boson*, *JHEP* **12** (2013) 089, [arXiv:1307.3536].

[14] F. Bezrukov, J. Rubio, and M. Shaposhnikov, *Living beyond the edge: Higgs inflation and vacuum metastability*, *Phys. Rev.* **D92** (2015), no. 8 083512, [arXiv:1412.3811].

[15] F. Bezrukov and M. Shaposhnikov, *Why should we care about the top quark Yukawa coupling?*, *J. Exp. Theor. Phys.* **120** (2015) 335–343, [arXiv:1411.1923].

[16] C. D. Froggatt and H. B. Nielsen, *Standard model criticality prediction: Top mass* 173 ± 5 *GeV and Higgs mass* 135 ± 9 *GeV*, *Phys. Lett.* **B368** (1996) 96–102, [hep-ph/9511371].

[17] M. Shaposhnikov and C. Wetterich, *Asymptotic safety of gravity and the Higgs boson mass*, *Phys. Lett.* **B683** (2010) 196–200, [arXiv:0912.0208].

[18] T. Carli, "ATLAS + ALICE highlights (talk at ICHEP 2018)." https://indico.cern.ch/event/686555/contributions/3028060/.

[19] S. Rahatlou, "CMS + LHCb highlights (talk at ICHEP 2018)." https://indico.cern.ch/event/686555/contributions/3028061/.

[20] **CMS** Collaboration, "CMS Supersymmetry Physics Results." https://twiki.cern.ch/twiki/bin/view/CMSPublic/PhysicsResultsSUSY, 2015.

[21] **ATLAS** Collaboration, "ATLAS Exotics Public Results." https://twiki.cern.ch/twiki/bin/view/AtlasPublic/SupersymmetryPublicResults, 2015.

[22] **ATLAS** Collaboration, "ATLAS Supersymmetry Searches." https://twiki.cern.ch/twiki/bin/view/AtlasPublic/ExoticsPublicResults, 2015.

[23] **CMS** Collaboration, "CMS Exotica Public Physics Results." https://twiki.cern.ch/twiki/bin/view/AtlasPublic/ExoticsPublicResults, 2015.

[24] Del Re, Daniele, "Exotics (talk at ICHEP 2018)." https://indico.cern.ch/event/686555/contributions/3028077/.

[25] S. Strandberg, "SUSY (talk at ICHEP 2018)." https://indico.cern.ch/event/686555/contributions/3028076/.

[26] **Belle** Collaboration, M. Huschle et al., *Measurement of the branching ratio of $\bar{B} \to D^{(*)}\tau^-\bar{\nu}_\tau$ relative to $\bar{B} \to D^{(*)}\ell^-\bar{\nu}_\ell$ decays with hadronic tagging at Belle*, *Phys. Rev.* **D92** (2015), no. 7 072014, [arXiv:1507.03233].

[27] **Belle** Collaboration, Y. Sato et al., *Measurement of the branching ratio of $\bar{B}^0 \to D^{*+}\tau^-\bar{\nu}_\tau$ relative to $\bar{B}^0 \to D^{*+}\ell^-\bar{\nu}_\ell$ decays with a semileptonic tagging method*, *Phys. Rev.* **D94** (2016), no. 7 072007, [arXiv:1607.07923].

[28] **Belle** Collaboration, S. Hirose et al., *Measurement of the τ lepton polarization and $R(D^*)$ in the decay $\bar{B} \to D^*\tau^-\bar{\nu}_\tau$*, *Phys. Rev. Lett.* **118** (2017), no. 21 211801, [arXiv:1612.00529].

[29] **LHCb** Collaboration, R. Aaij et al., *Measurement of the ratio of branching fractions $\mathcal{B}(\bar{B}^0 \to D^{*+}\tau^-\bar{\nu}_\tau)/\mathcal{B}(\bar{B}^0 \to D^{*+}\mu^-\bar{\nu}_\mu)$*, *Phys. Rev. Lett.* **115** (2015), no. 11 111803, [arXiv:1506.08614]. [Erratum: Phys. Rev. Lett.115,no.15,159901(2015)].

[30] **LHCb** Collaboration, R. Aaij et al., *Measurement of the ratio of the $B^0 \to D^{*-}\tau^+\nu_\tau$ and $B^0 \to D^{*-}\mu^+\nu_\mu$ branching fractions using three-prong τ-lepton decays*, *Phys. Rev. Lett.* **120** (2018), no. 17 171802, [arXiv:1708.08856].

[31] M. Yokoyama, "Long baseline experiments (talk at ICHEP 2018)." https://indico.cern.ch/event/686555/contributions/3028063/.

[32] S. Petcov, "Neutrino theory including leptogenesis (talk at ICHEP 2018)." https://indico.cern.ch/event/686555/contributions/3028066/.

[33] C. Giunti, *Light Sterile Neutrinos: Status and Perspectives*, *Nucl. Phys.* **B908** (2016) 336–353, [arXiv:1512.04758].

[34] H. S. Lee, "Dark matter (talk at ICHEP 2018)." https://indico.cern.ch/event/686555/contributions/3028096.

[35] L. D. Duffy and K. van Bibber, *Axions as Dark Matter Particles*, *New J. Phys.* **11** (2009) 105008, [arXiv:0904.3346].

[36] A. Boyarsky, M. Drewes, T. Lasserre, S. Mertens, and O. Ruchayskiy, *Sterile Neutrino Dark Matter*, *Prog. Part. Nucl. Phys.* (2018) [arXiv:1807.07938].

[37] M. Shaposhnikov and C. Wetterich, *Asymptotic safety of gravity and the Higgs boson mass*, *Phys. Lett.* **B683** (2010) 196–200, [arXiv:0912.0208].

[38] A. Berlin, N. Blinov, G. Krnjaic, P. Schuster, and N. Toro, *Dark Matter, Millicharges, Axion and Scalar Particles, Gauge Bosons, and Other New Physics with LDMX*, [arXiv:1807.01730].

[39] **MiniBooNE DM** Collaboration, A. A. Aguilar-Arevalo et al., *Dark Matter Search in Nucleon, Pion, and Electron Channels from a Proton Beam Dump with MiniBooNE*, [arXiv:1807.06137].

[40] **MiniBooNE** Collaboration, A. A. Aguilar-Arevalo et al., *Dark Matter Search in a Proton Beam Dump with MiniBooNE*, *Phys. Rev. Lett.* **118** (2017), no. 22 221803, [arXiv:1702.02688].

[41] P. deNiverville, C.-Y. Chen, M. Pospelov, and A. Ritz, *Light dark matter in neutrino beams: production modelling and scattering signatures at MiniBooNE, T2K and SHiP*, *Phys. Rev.* **D95** (2017), no. 3 035006, [arXiv:1609.01770].

[42] **CRESST** Collaboration, G. Angloher et al., *Results on light dark matter particles with a*

low-threshold CRESST-II detector, *Eur. Phys. J.* **C76** (2016), no. 1 25, [arXiv:1509.01515].

[43] **NA64** Collaboration, D. Banerjee et al., *Search for vector mediator of Dark Matter production in invisible decay mode*, *Phys. Rev.* **D97** (2018), no. 7 072002, [arXiv:1710.00971].

[44] **NA64** Collaboration, D. Banerjee et al., *Search for invisible decays of sub-GeV dark photons in missing-energy events at the CERN SPS*, *Phys. Rev. Lett.* **118** (2017), no. 1 011802, [arXiv:1610.02988].

[45] **BDX** Collaboration, M. Battaglieri et al., *Dark Matter Search in a Beam-Dump eXperiment (BDX) at Jefferson Lab*, [arXiv:1607.01390].

[46] V. V. Gligorov, S. Knapen, M. Papucci, and D. J. Robinson, *Searching for Long-lived Particles: A Compact Detector for Exotics at LHCb*, *Phys. Rev.* **D97** (2018), no. 1 015023, [arXiv:1708.09395].

[47] J. P. Chou, D. Curtin, and H. J. Lubatti, *New Detectors to Explore the Lifetime Frontier*, *Phys. Lett.* **B767** (2017) 29–36, [arXiv:1606.06298].

[48] D. Curtin and M. E. Peskin, *Analysis of Long Lived Particle Decays with the MATHUSLA Detector*, *Phys. Rev.* **D97** (2018), no. 1 015006, [arXiv:1705.06327].

[49] J. A. Evans, *Detecting Hidden Particles with MATHUSLA*, *Phys. Rev.* **D97** (2018), no. 5 055046, [arXiv:1708.08503].

[50] J. L. Feng, I. Galon, F. Kling, and S. Trojanowski, *ForwArd Search ExpeRiment at the LHC*, *Phys. Rev.* **D97** (2018), no. 3 035001, [arXiv:1708.09389].

[51] J. L. Feng, I. Galon, F. Kling, and S. Trojanowski, *Dark Higgs bosons at the ForwArd Search ExpeRiment*, *Phys. Rev.* **D97** (2018), no. 5 055034, [arXiv:1710.09387].

[52] F. Kling and S. Trojanowski, *Heavy Neutral Leptons at FASER*, *Phys. Rev.* **D97** (2018), no. 9 095016, [arXiv:1801.08947].

[53] **LHCb** Collaboration, R. Aaij et al., *Search for Majorana neutrinos in $B^- \to \pi^+ \mu^- \mu^-$ decays*, *Phys. Rev. Lett.* **112** (2014), no. 13 131802, [arXiv:1401.5361].

[54] **CMS** Collaboration, V. Khachatryan et al., *Search for heavy Majorana neutrinos in $\mu^\pm \mu^\pm +$ jets events in proton-proton collisions at $\sqrt{s}$ = 8 TeV*, *Phys. Lett.* **B748** (2015) 144–166, [arXiv:1501.05566].

[55] **ATLAS** Collaboration, G. Aad et al., *Search for heavy Majorana neutrinos with the ATLAS detector in pp collisions at $\sqrt{s} = 8$ TeV*, *JHEP* **07** (2015) 162, [arXiv:1506.06020].

[56] **CMS** Collaboration, A. M. Sirunyan et al., *Search for heavy neutral leptons in events with three charged leptons in proton-proton collisions at $\sqrt{s} = 13$ TeV*, *Phys. Rev. Lett.* **120** (2018), no. 22 221801, [arXiv:1802.02965].

[57] A. Izmaylov and S. Suvorov, *Search for heavy neutrinos in the ND280 near detector of the T2K experiment*, *Phys. Part. Nucl.* **48** (2017), no. 6 984–986.

[58] **SHiP** Collaboration, P. Mermod, *Hidden sector searches with SHiP and NA62*, in *2017 International Workshop on Neutrinos from Accelerators (NuFact17) Uppsala University Main Building, Uppsala, Sweden, September 25-30, 2017*, 2017. [arXiv:1712.01768].

[59] **NA62** Collaboration, E. Cortina Gil et al., *Search for heavy neutral lepton production in K^+ decays*, *Phys. Lett.* **B778** (2018) 137–145, [arXiv:1712.00297].

[60] S. Antusch, E. Cazzato, and O. Fischer, *Sterile neutrino searches via displaced vertices at LHCb*, *Phys. Lett.* **B774** (2017) 114–118, [arXiv:1706.05990].

[61] M. Drewes, J. Hajer, J. Klaric, and G. Lanfranchi, *NA62 sensitivity to heavy neutral leptons in the low scale seesaw model*, [arXiv:1801.04207].

[62] **Belle** Collaboration, D. Liventsev et al., *Search for heavy neutrinos at Belle*, *Phys. Rev.* **D87** (2013), no. 7 071102, [arXiv:1301.1105].

[63] **Belle** Collaboration, Y. Kwon, *Search for dark sector particles at Belle*, *PoS* **EPS-HEP2017**

(2017) 069.

[64] **Belle** Collaboration, I. Jaegle, *Search for the dark photon and the dark Higgs boson at Belle*, *Phys. Rev. Lett.* **114** (2015), no. 21 211801, [arXiv:1502.00084].

[65] **BaBar** Collaboration, J. P. Lees et al., *Search for Invisible Decays of a Dark Photon Produced in e^+e^- Collisions at BaBar*, *Phys. Rev. Lett.* **119** (2017), no. 13 131804, [arXiv:1702.03327].

[66] **ATLAS** Collaboration, M. Aaboud et al., *Search for long-lived particles in final states with displaced dimuon vertices in pp collisions at $\sqrt{s} = 13$ TeV with the ATLAS detector*, [arXiv:1808.03057].

[67] **LHCb** Collaboration, R. Aaij et al., *Search for Dark Photons Produced in 13 TeV pp Collisions*, *Phys. Rev. Lett.* **120** (2018), no. 6 061801, [arXiv:1710.02867].

[68] F. Addesa et al., *The SE-CpFM Detector for the Crystal-Assisted Extraction at CERN-SPS*, in *Proc. of International Beam Instrumentation Conference (IBIC'17), Grand Rapids, MI, USA, 20-24 August 2017*, no. 6 in International Beam Instrumentation Conference, (Geneva, Switzerland), pp. 419–422, JACoW, Mar., 2018. https://doi.org/10.18429/JACoW-IBIC2017-WEPCF04.

[69] K. Kershaw et al., *Design Development for the Beam Dump Facility Target Complex at CERN*, *JINST* **13** (2018), no. 10 P10011, [arXiv:1806.05920].

[70] **SHiP** Collaboration, A. Akmete et al., *Muon flux measurements for SHiP at H4*, Tech. Rep. CERN-SPSC-2017-020. SPSC-EOI-016, CERN, Geneva, June 2017.

[71] A. Ferrari, P. R. Sala, A. Fasso, and J. Ranft, *FLUKA: A multi-particle transport code (Program version 2005)*, *CERN-2005-010, SLAC-R-773, INFN-TC-05-11* (2005).

[72] P. Santos Diaz, *Preliminary design of the decay volume vacuum system for the SHiP experiment*, Tech. Rep. CERN EDMS 2000025, January 2019.

[73] I. Bezshyiko et al., *TauFV: a fixed-target experiment to search for flavour violation in tau decays*, 2018. submitted to ESPPU.

[74] M. Al-Turany, D. Bertini, R. Karabowicz, D. Kresan, P. Malzacher, T. Stockmanns, and F. Uhlig, *The fairroot framework*, *Journal of Physics: Conference Series* **396** (2012), no. 2 022001.

[75] T. Sjöstrand, S. Ask, J. R. Christiansen, R. Corke, N. Desai, P. Ilten, S. Mrenna, S. Prestel, C. O. Rasmussen, and P. Z. Skands, *An Introduction to PYTHIA 8.2*, *Comput. Phys. Commun.* **191** (2015) 159–177, [arXiv:1410.3012].

[76] S. Agostinelli et al., *Geant4 - a simulation toolkit*, *Nucl. Instr. and Meth.* **A508** (2003) 250.

[77] **SHiP** Collaboration, H. Dijkstra and T. Ruf, *Heavy Flavour Cascade Production in a Beam Dump*, December 2015. CERN-SHiP-NOTE-2015-009.

[78] **SHiP** Collaboration, C. Ahdida et al., *Sensitivity of the SHiP experiment to Heavy Neutral Leptons*, [arXiv:1811.00930].

[79] A. Monin, A. Boyarsky, and O. Ruchayskiy, *Hadronic decays of a light Higgs-like scalar*, [arXiv:1806.07759].

[80] F. Bergsma, *Prompt lepton production in a proton beam dump experiment*. PhD thesis, University of Amsterdam, 1990.

[81] **SHiP** Collaboration, T. Ruf, *Studying Multiple Scattering with GEANT4 v10.3.2*, December 2018. CERN-SHiP-NOTE-2017-003.

[82] G. Ruggiero, *NA48 Results*, in *Proceedings, 43rd Rencontres de Moriond on Electroweak Interactions and Unified Theories: La Thuile, Italy, March 1-8, 2008*, (Paris, France), pp. 293–300, Moriond, Moriond, 2008.

[83] S. A. Akimenko, V. I. Belousov, A. M. Blik, G. I. Britvich, V. N. Kolosov, V. M. Kutin, B. N. Lebedev, V. N. Peleshko, Ya. N. Rastsvetalov, and A. S. Solovev, *MULTIPLE COULOMB SCATTERING OF 7.3-GeV/c AND 11.7-GeV/c MUONS ON Cu TARGET*, *Nucl. Instrum. Meth.*

A243 (1986) 518.

[84] M. Rosenthal, N. Charitonidis, P. Chatzidaki, R. Margraf, H. Wilkens, F. Bergsma, and P.-A. Guidici, *Magnetic Field Measurement of the GOLIATH Magnet in EHN1*, Tech. Rep. CERN-ACC-NOTE-2018-0028, March, 2018.

[85] A. Alexandrov et al., *A new fast scanning system for the measurement of large angle tracks in nuclear emulsions*, *JINST* **10** (2015), no. 11 P11006.

[86] A. Alexandrov et al., *A new generation scanning system for the high-speed analysis of nuclear emulsions*, *JINST* **11** (2016), no. 06 P06002.

[87] A. Alexandrov et al., *The Continuous Motion Technique for a New Generation of Scanning Systems*, *Sci. Rep.* **7** (2017), no. 1 7310.

[88] R. Acquafredda et al., *The OPERA experiment in the CERN to Gran Sasso neutrino beam*, *JINST* **4** (2009) P04018.

[89] **OPERA** Collaboration, N. Agafonova et al., *Final Results of the OPERA Experiment on ν_τ Appearance in the CNGS Neutrino Beam*, *Phys. Rev. Lett.* **120** (2018), no. 21 211801, [arXiv:1804.04912]. [Erratum: Phys. Rev. Lett.121,no.13,139901(2018)].

[90] **OPERA** Collaboration, N. Agafonova et al., *Procedure for short-lived particle detection in the OPERA experiment and its application to charm decays*, *Eur. Phys. J.* **C74** (2014), no. 8 2986, [arXiv:1404.4357].

[91] **OPERA** Collaboration, N. Agafonova et al., *Momentum measurement by the Multiple Coulomb Scattering method in the OPERA lead emulsion target*, *New J. Phys.* **14** (2012) 013026, [arXiv:1106.6211].

[92] **OPERA** Collaboration, N. Agafonova et al., *Final results of the search for $\nu_\mu \to \nu_e$ oscillations with the OPERA detector in the CNGS beam*, *JHEP* **06** (2018) 151, [arXiv:1803.11400].

[93] L. Arrabito et al., *Hardware performance of a scanning system for high speed analysis of nuclear emulsions*, *Nucl. Instrum. Meth.* **A568** (2006) 578–587, [physics/0604043].

[94] N. Armenise et al., *High-speed particle tracking in nuclear emulsion by last-generation automatic microscopes*, *Nucl. Instrum. Meth.* **A551** (2005) 261–270.

[95] C. Fukushima, M. Kimura, S. Ogawa, H. Shibuya, G. Takahashi, K. Kodama, T. Hara, and S. Mikado, *A thin emulsion spectrometer using a compact permanent magnet*, *Nucl. Instrum. Meth.* **A592** (2008) 56–62.

[96] G. Bencivenni, R. De Oliveira, G. Morello, and M. P. Lener, *The micro-Resistive WELL detector: a compact spark-protected single amplification-stage MPGD*, *JINST* **10** (2015), no. 02 P02008, [arXiv:1411.2466].

[97] M. S. Dixit and A. Rankin, *Simulating the charge dispersion phenomena in micro pattern gas detectors with a resistive anode*, *Nucl. Instrum. Meth.* **A566** (2006) 281–285, [physics/0605121].

[98] G. Bencivenni, R. De Oliveira, G. Felici, M. Gatta, G. Morello, A. Ochi, M. P. Lener, and E. Tskhadadze, *Performance of μ-RWELL detector vs resistivity of the resistive stage*, *Nucl. Instrum. Meth.* **A886** (2018) 36–39.

[99] T. Alexopoulos et al., *Development of large size Micromegas detector for the upgrade of the ATLAS muon system*, *Nucl. Instrum. Meth.* **A617** (2010) 161–165.

[100] **LHCb** Collaboration, *LHCb Tracker Upgrade Technical Design Report*, 2014. CERN-LHCC-2014-001, LHCB-TDR-015.

[101] O. Giard, G. Haefeli, et al., "Modular beam telescopes based on scintillation fibers and silicon photo-multipliers (Talk at BTTB workshop 2018)." https://indico.desy.de/indico/event/18050/session/9/contribution/18.

[102] "GARFIELD simulation package." http://cern.ch/magboltz, http://cern.ch/garfield

and http://cern.ch/garfieldpp.

[103] **PANDA** Collaboration, *Technical design report for the panda (antiproton annihilations at darmstadt) straw tube tracker*, *The European Physical Journal A* **49** (Feb, 2013) 25.

[104] C. Betancourt et al., *Application of large area SiPMs for the readout of a plastic scintillator based timing detector*, *JINST* **12** (2017), no. 11 P11023, [arXiv:1709.08972].

[105] S. Gomez et al., *MUSIC: An 8 channel readout ASIC for SiPM arrays*, in *Proceedings, Optical Sensing and Detection IV, SPIE Photonics Europe, 2016, Brussels, Belgium*, vol. 9899, 2016.

[106] W. Baldini et al., *Measurement of parameters of scintillating bars with wavelength-shifting fibres and silicon photomultiplier readout for the SHiP Muon Detector*, *JINST* **12** (2017), no. 03 P03005, [arXiv:1612.01125].

[107] F. Bezrukov and D. Gorbunov, *Light inflaton Hunter's Guide*, *JHEP* **05** (2010) 010, [arXiv:0912.0390].

[108] K. Bondarenko, A. Boyarsky, D. Gorbunov, and O. Ruchayskiy, *Phenomenology of GeV-scale Heavy Neutral Leptons*, [arXiv:1805.08567].

[109] **LHCb** Collaboration, R. Aaij et al., *Observation of $B_c^+ \to D^0 K^+$ decays*, *Phys. Rev. Lett.* **118** (2017), no. 11 111803, [arXiv:1701.01856].

[110] C.-H. Chang, C. Driouichi, P. Eerola, and X. G. Wu, *BCVEGPY: An Event generator for hadronic production of the B_c meson*, *Comput. Phys. Commun.* **159** (2004) 192–224, [hep-ph/0309120].

[111] M. Cacciari, S. Frixione, and P. Nason, *The p_T spectrum in heavy flavor photoproduction*, *JHEP* **03** (2001) 006, [hep-ph/0102134].

[112] D. Gorbunov and M. Shaposhnikov, *How to find neutral leptons of the νMSM?*, *JHEP* **10** (2007) 015, [arXiv:0705.1729]. [Erratum: JHEP11 (2013), 101].

[113] K. Bondarenko, I. Boiarska, A. Boyarsky, M. Ovchynnikov, and O. Ruchayskiy, *Light dark matter with scalar mediator at Intensity Frontier experiments*, *to appear* (2018).

[114] B. Patt and F. Wilczek, *Higgs-field portal into hidden sectors*, [hep-ph/0605188].

[115] B. Batell, M. Pospelov, and A. Ritz, *Exploring Portals to a Hidden Sector Through Fixed Targets*, *Phys. Rev.* **D80** (2009) 095024, [arXiv:0906.5614].

[116] J. D. Clarke, R. Foot, and R. R. Volkas, *Phenomenology of a very light scalar (100 MeV $< m_h <$ 10 GeV) mixing with the SM Higgs*, *JHEP* **02** (2014) 123, [arXiv:1310.8042].

[117] K. Schmidt-Hoberg, F. Staub, and M. W. Winkler, *Constraints on light mediators: confronting dark matter searches with B physics*, *Phys. Lett.* **B727** (2013) 506–510, [arXiv:1310.6752].

[118] J. F. Donoghue, J. Gasser, and H. Leutwyler, *The Decay of a Light Higgs Boson*, *Nucl. Phys.* **B343** (1990) 341–368.

[119] B. Holdom, *Two U(1)'s and Epsilon Charge Shifts*, *Phys. Lett.* **B166** (1986) 196–198.

[120] T. Sjöstrand, S. Ask, J. R. Christiansen, R. Corke, N. Desai, P. Ilten, S. Mrenna, S. Prestel, C. O. Rasmussen, and P. Z. Skands, *An Introduction to PYTHIA 8.2*, *Comput. Phys. Commun.* **191** (2015) 159–177, [arXiv:1410.3012].

[121] **Particle Data Group** Collaboration, C. Patrignani et al., *Review of Particle Physics*, *Chin. Phys.* **C40** (2016), no. 10 100001.

[122] D. Gorbunov, A. Makarov, and I. Timiryasov, *Decaying light particles in the SHiP experiment: Signal rate estimates for hidden photons*, *Phys. Rev.* **D91** (2015), no. 3 035027, [arXiv:1411.4007].

[123] J. Blümlein and J. Brunner, *New Exclusion Limits on Dark Gauge Forces from Proton Bremsstrahlung in Beam-Dump Data*, *Phys. Lett.* **B731** (2014) 320–326, [arXiv:1311.3870].

[124] L. Carloni, J. Rathsman, and T. Sjöstrand, *Discerning Secluded Sector gauge structures*, *JHEP* **04** (2011) 091, [arXiv:1102.3795].

[125] J. D. Bjorken, R. Essig, P. Schuster, and N. Toro, *New Fixed-Target Experiments to Search for Dark Gauge Forces*, *Phys. Rev.* **D80** (2009) 075018, [arXiv:0906.0580].

[126] B. Döbrich, J. Jaeckel, F. Kahlhoefer, A. Ringwald, and K. Schmidt-Hoberg, *ALPtraum: ALP production in proton beam dump experiments*, *JHEP* **02** (2016) 018, [arXiv:1512.03069].

[127] J. Alwall, M. Herquet, F. Maltoni, O. Mattelaer, and T. Stelzer, *MadGraph 5 : Going Beyond*, *JHEP* **06** (2011) 128, [arXiv:1106.0522].

[128] **CHORUS** Collaboration, A. Kayis-Topaksu et al., *Cross-section measurement for quasi-elastic production of charmed baryons in nu N interactions*, *Phys. Lett.* **B575** (2003) 198–207.

[129] **CHORUS** Collaboration, A. Kayis-Topaksu et al., *Measurement of topological muonic branching ratios of charmed hadrons produced in neutrino-induced charged-current interactions*, *Phys. Lett.* **B626** (2005) 24–34.

[130] **CHORUS** Collaboration, G. Onengut et al., *Measurement of fragmentation properties of charmed particle production in charged-current neutrino interactions*, *Phys. Lett.* **B604** (2004) 145–156.

[131] A. Kayis-Topaksu et al., *Measurement of charm production in neutrino charged-current interactions*, *New J. Phys.* **13** (2011) 093002, [arXiv:1107.0613].

[132] **CHORUS** Collaboration, A. Kayis-Topaksu et al., *Observation of one event with the characteristics of associated charm production in neutrino charged-current interactions*, *Phys. Lett.* **B539** (2002) 188–196.

[133] **HERA-B** Collaboration, I. Abt et al., *Measurement of D^0, D^+, D_s^+ and D^{*+} Production in Fixed Target* 920*-GeV Proton-Nucleus Collisions*, *Eur. Phys. J.* **C52** (2007) 531–542, [arXiv:0708.1443].

[134] G. De Lellis, A. M. Guler, J. Kawada, U. Kose, O. Sato, and F. Tramontano, *Search for charmed pentaquarks in high energy anti-neutrino interactions*, *Nucl. Phys.* **B763** (2007) 268–282.

[135] **Particle Data Group** Collaboration, M. Tanabashi et al., *Review of Particle Physics*, *Phys. Rev.* **D98** (2018), no. 3 030001.

[136] G. Radel and R. Beyer, *Neutrino electron scattering*, *Mod. Phys. Lett.* **A8** (1993) 1067–1088.